Masteroppgave

NTNU
Norges teknisk-naturvitenskapelige universitet

Aslak Magdalon Blytt & Sander Sundt

Crack propagation in aluminium alloy plates: experiments, modelling and simulation

Masteroppgave i Produktutvikling og produksjon

Oktober 2020

NTNU
Norwegian University of
Science and Technology

Aslak Magdalon Blytt & Sander Sundt

Crack propagation in aluminium alloy plates: experiments, modelling and simulation

Masteroppgave i Produktutvikling og produksjon
Veileder: Odd Sture Hopperstad, Tore Børvik og Vetle Espeseth
Oktober 2020

Norges teknisk-naturvitenskapelige universitet
Fakultet for ingeniørvitenskap
Institutt for konstruksjonsteknikk

NTNU
Kunnskap for en bedre verden

Department of Structural Engineering
FACULTY OF ENGINEERING
NTNU – Norwegian University of Science and Technology

MASTER'S THESIS 2020

for

Aslak Magdalon Blytt and Sander Nicholas Sundt

Crack propagation in aluminium alloy plates: experiments, modelling and simulation

Aluminium is a widely used energy absorbent in the automotive industry. Bumper beams, crash boxes and various body parts are often made of aluminium alloys to absorb energy in connection with collisions. The reason why aluminium is a good energy absorbent is that the material is lightweight, strong and ductile. In finite element simulations of components and structures potentially subjected to such loading conditions, material models describing the large deformation behaviour and failure of aluminium alloys are needed. The topic of this study is modelling and simulation of crack propagation in aluminium alloy plates subjected to quasi-static and dynamic loading. Plate tearing tests will be performed under quasi-static loading conditions using a specially developed experimental set-up and used for validation of the numerical simulations. In addition, existing test data on dynamically loaded plates of the same aluminium alloy will be used for validation under dynamic loading conditions. Finite element simulations will be performed with Abaqus using solid elements and the Gurson model to describe plasticity, damage and fracture. The objective of the research is to evaluate the accuracy, efficiency and robustness of the Gurson model for simulating crack propagation in aluminium alloy plates.

The main tasks of the research project are as follows:

1. Literature study on ductile fracture of aluminium alloys, the Gurson model and numerical simulation of crack propagation.
2. Experimental study on plate tearing of AA6016 plates in different tempers under quasi-static loading conditions.
3. Identification of parameters in the Gurson model based on existing test data for the AA6016 plate material in different tempers.
4. Modelling and simulations of quasi-static plate tearing applying the calibrated Gurson model and validation against the new test data.
5. Numerical study on crack propagation in AA6016 plates subjected to impact loading conditions and validation against existing test data.

Supervisors: Vetle Espeseth, Odd Sture Hopperstad, Tore Børvik (NTNU)

The thesis must be written according to current requirements and submitted to the Department of Structural Engineering, NTNU, no later than February1, 2021.

NTNU, August 26, 2020.

Odd Sture Hopperstad
Professor

Acknowledgments

During this master thesis, our supervisors have been Professor Odd Sture Hopperstad, Tore Børvik and PhD. candidate Vetle Espeseth at the Structural Impact Laboratory (SIMLab), Department of Structural Engineering, Norwegian University of Science and Technology (NTNU). We wish to show our gratitude for their encouraging guidance, enthusiasm and input. A special thanks to PhD candidate Vetle Espeseth his modeling contributions in the Finite Element Analysis (FEA) program Abaqus.

The experimental work has been carried out by the dedicated and very helpful laboratory staff at both the Department of Structural Engineering at NTNU and SINTEF. We want to give a special thanks to senior Engineer Trond Ausetad and Tore Wisth for their contribution in setting up the experiment.

We would also like to thank PhD. candidate Henrik Granum for his modeling contribution in Abaqus and valuable discussion.

The SIMLab research group are acknowledged for an inspiring and friendly working environment.

Trondheim, January 30th, 2021

Aslak Magdalon Blytt

Sander Sundt

Abstract

When properly calibrated, the Gurson-Tvergaard-Needleman (GTN) model has the potential to predict crack initiation and propagation over a range of loading conditions. This paper addresses the procedures for calibrating the GTN-model parameters in addition to the extensively used Cockroft-Latham (CL) fracture criterion, for three tempers of AA6016 aluminum alloy. Data from five separate previously conducted experimental studies have been used for calibration and model validation. Uniaxial tensile tests were used to determine the flow stress and isotropic hardening, defined by the Voce-hardening law. Thereafter data from notched tensile tests were used to determine the damage and failure-parameters of the GTN and CL model. Model validation was performed using finite element simulations of single edge notched tension tests, modified Arcan tests, and a low-velocity drop-weight impact test. An experimental study was conducted on double edge notched tension specimens and subsequent simulations of the same test used as a final validation. All simulations were performed using Abaqus/Explicit using eight-node linear brick elements. The numerical results using both models were in good agreement with the Experimental data. The same trends seen in the quasi-static experiments was also seen for dynamic conditions, corroborating the notion that the quasi-static tests can be used fro validation for similar dynamic tests on AA6016. Considering the simplicity of the calibration process and the computational efficiency of the models, the results demonstrate, that when calibrated correctly, both models are useful tools in predicting ductile failure. Moreover, despite the greater complexity of a coupled damage criterion the computational efficiency of both models are roughly the same.

Table of contents

Acknowledgements ii

Abstract iii

1 Introduction 1
- 1.1 Background and motivation . . . 1
- 1.2 Previous work . . . 1
- 1.3 Objective and aim . . . 2

2 Material mechanics 2
- 2.1 Aluminum alloy . . . 3
- 2.2 Fracture mechanisms . . . 4
  - 2.2.1 Ductile Fracture . . . 4
- 2.3 Uniaxial tensile test . . . 7
  - 2.3.1 Necking . . . 7
- 2.4 Material modeling . . . 8
  - 2.4.1 Yield Criterion . . . 8
  - 2.4.2 Von Mises Yield Criterion . . . 10
  - 2.4.3 Plastic flow rule . . . 10
  - 2.4.4 Hardening Rules . . . 12
  - 2.4.5 Ductile failure criterion . . . 13
  - 2.4.6 Anisotropy . . . 14
- 2.5 Porous plasticity . . . 14
  - 2.5.1 Gurson's Porous Plasticity Model . . . 15
- 2.6 Finite element method (FEM) . . . 18
- 2.7 Explicit analysis . . . 19
  - 2.7.1 Energy balance . . . 19
- 2.8 Contact . . . 20

3 Experimental study 21
- 3.1 Material and experimental setup . . . 21
  - 3.1.1 Uniaxial tension tests . . . 21
  - 3.1.2 Notched tension tests . . . 22
  - 3.1.3 SENT . . . 22
  - 3.1.4 DENT . . . 23
- 3.2 Experimental results . . . 24
  - 3.2.1 Uniaxial tensile test . . . 24
  - 3.2.2 Notched tensile test results . . . 25
  - 3.2.3 SENT - test . . . 25
  - 3.2.4 DENT - test . . . 28

4 Modeling and simulations **33**
4.1 Material model . . . 33
4.2 Finite element modelling . . . 33
4.2.1 Uniaxial and notched tension . . . 35
4.2.2 SENT . . . 35
4.2.3 DENT-numerical model . . . 35

5 Calibration **35**
5.1 Calibration of hardening parameters . . . 36
5.2 Calibration of the GTN-model . . . 36
5.2.1 Parametric study . . . 37
5.2.2 Calibration of f_0 . . . 41
5.2.3 Calibration of ε_N ,f_N and s_N . . . 41
5.2.4 Calibration of f_c and f_F . . . 42
5.2.5 Calibration to the 0.15mm mesh . . . 44
5.3 Calibration of the Cockroft-Latham fracture criterion . . . 45

6 Numerical results and discussion **48**
6.1 Material tests . . . 48
6.2 SENT-test . . . 52
6.2.1 Stress state analysis . . . 54
6.2.2 Mesh structure sensitivity . . . 56
6.3 DENT-test . . . 57
6.3.1 Revised model . . . 62

7 Case study 1: Modified Arcan tear tests **66**
7.1 Experimental results . . . 66
7.2 Numerical modelling . . . 67
7.3 Numerical results . . . 67

8 Case study 2: Drop weight impact tests **70**
8.1 Experimental setup . . . 70
8.1.1 Numerical modelling . . . 70
8.1.2 Numerical and experimental results . . . 71

9 Summary **73**

10 Conclusion **74**
10.1 Proposal for future fork . . . 74

References **75**

A Figures **79**
A.1 Figures to section 3 (Experimental setups) . . . 79
A.2 Figures to section 4 (Finite element modelling) . . . 80
A.3 Figures to section 5 (Calibration of material models) . . . 81
A.4 Figures to section 6 (Numerical results and Discussion) . . . 84

A.5 Figures to section 7 (Modified Arcan-tests) 90
A.6 Figures to section 8 (Drop weight impact test) 91

B Theory **91**
B.1 The Central Difference Method 91
B.2 Drop test displacement calculation 93

C Material Cards **94**
C.1 T6 94
C.2 T7 95
C.3 T4 96

List of Tables

1 Chemical composition of AA6016 in wt% 3
2 Table of calibrated parameters from [1] 37
3 Gurson damage parameters according to literature. 38
4 Fitted damage parameters 42
5 Final GTN constitutive parameters calibrated to the NT3 specimen for h_e=0.25, . . 44
6 Final GTN constitutive parameters calibrated to the NT3 specimen using a 0.15mm mesh. 45
7 CL, damage parameter calibration 47

List of Figures

2.1 Void nucleation, growth, and coalescence in ductile metals: (a) inclusions in a ductile matrix, (b) void nucleation, (c) void growth, (d) strain localization between voids, (e) necking between voids, and (f) void coalescence and fracture[2]. 5
2.2 Formation of the cup and cone fracture surface in uniaxial tension:(a) void growth in a triaxial stress state, (b) crack and deformation band formation, (c) nucleation at smaller particles along the deformation bands, and (d) cup and cone fracture[2]. . . . 5
2.3 Mechanisms for ductile crack growth: (a) initial state, (b) void growth at the crack tip, and (c) coalescence of voids with the crack tip[2]. 6
2.4 Ductile growth of an edge crack[2]. 6
2.5 Ductile crack growth in a 45° zig-zag pattern.[2] 7
2.6 Elastic domain, yield surface and inadmissible region for a two-dimensional stress state[3] 8
2.7 Geometric representation of the associated flow rule for Tresca and von Mises yield surfaces. The associated flow rule implies that the incremental plastic strain vector is normal to the yield locus.[3] 11
2.8 Consequences of the principle of maximum plastic dissipation: normality of the plastic flow and convexity of the yield surface. [3] 12
2.9 Spherical void shape geometry with outer cell wall centered around the void. 15
3.1 Geometry of test specimens with measures in mm: (a) uniaxial tension, (b) and (c) notched tension, (d) single edge notched tension and(e) double edge notched tension 21
3.2 Illustrative drawing and clamping configuration of the SENT-test made by PhD. Candidate Vetle Espeseth. 23
3.3 Illustrative drawing and clamping configuration of the DENT-test. 24
3.4 Engineering stress-strain curves from (a) samples in the rolled direction (b) representative tests in each direction. 24
3.5 Extracted force-strain and local strain-strain curves from (a) NT3 tesnsion tests, and (b) NT10 tension tests. 25
3.6 (Top left) Sketch of the SENT- test made by PhD. candidate Vetle Espeseth. Experimental results for (a) Temper T4, (b) temper T6 and (c) temper T7. 26
3.7 Image series from the SENT-experiment using the (left column) temper T4, (centre column) temper T6 and (right column) temper T7. 27
3.8 The measured surface crack displacement plotted against the slit opening displacement on the second y-axis with the force-SOD curves plotted in the background for referencing. 28
3.9 (Top left) Sketch of the DENT-specimen. Experimental results for (a) temper T4, (b) temper T6 and (c) temper T7. 29
3.10 DIC strain-map of accumulated strains, ε_{yy}, of the T7 temper, using (a) the specimen at the start of the experiment as reference frame, and (b) using the image corresponding to the onset of fracture as reference frame. 30
3.11 Image series from the DENT-experiment for the (left column) T4 temper, (centre column) T6 temper and the (right column) T7 temper. 31
3.12 Fracture surfaces of the the DENT specimens. 31
3.13 a) Field-maps from DIC of horizontal displacements at two selected instances. b) Horizontal displacements and force measure plotted against the vertical displacements. 32

4.1 Finite element meshes of test specimens: a) UT200, b) NT10, c) NT335, d) SENT and e) DENT 34
5.1 Stress-strain curves from experiments and simulations of the Uniaxial tensile tests. . 36
5.2 Force-strain curves and VVF-strain curves from the parameter study of a) f_0 , b) f_N , c) ε_N and d) s_N , for the T4 temper 39
5.3 Force-strain curves and VVF-strain curves from the parameter study of a) f_0 , b) f_N , c) ε_N and d) s_N , for the T6 temper 40
5.4 Force-strain curves and VVF-strain curves from the parameter study of a) f_0 , b) f_N , c) ε_N and d) s_N , for the T7 temper. 41
5.5 Illustration of calibration process for the T4 temper. a) Extraction of ε_N at the onset of deviation between experimental force-strain curves and the corresponding FE analysis results of the GTN-model with nucleation omitted. b) f_N optimization steps. c) Extraction of the fracture parameters, f_c from the simulated VVF corresponding to the experimental fracture strain. 43
5.6 Simulation and experimental force-strain curves from the NT3-tensile test, along with strain-local-logarithmic-strain curves plotted along the second y-axis. 44
5.7 Force-strain curves and logarithmic strains from experiments and simulations of the NT3 - tensile tests with a 0.15mm mesh in the critical region. 45
5.8 Acquisition of the damage parameter, W_c for the T7 temper, from the accumulated damage up to the experimentally observed fracture strain from the T7 46
5.9 Experimental NT3 force-displacement and logarithmic strain-displacement curves and corresponding numerical results using the a) the CL-0.25mm calibration applied to the 0.25mm model b) the CL-0.25mm(initial) and CL-0.15mm (revised) -calibration applied to the 0.15mm model. 47
6.1 a) Experimental and numerical stress-strain curves for the UT200- test for all tempers. b) Strain rate sensitivity study for the T7 temper. 49
6.2 NT3 Experimental and numerical force-strain curves plotted with the logarithmic strains as a function of the engineering strains for the a) 0.25mm mesh and b) 0.15mm mesh. 49
6.3 NT10 Experimental and numerical force-strain curves plotted with the logarithmic strains as a function of the engineering strains for the a) 0.25mm mesh and b) 0.15mm mesh. 49
6.4 Evolution of the stress state (i.e., Lode parameter and stress triaxiality) as function of the equivalent plastic strain extracted from the critical element. 51
6.5 Strain fields from FE simulations of the T7 NT10-test a) just befor fracture in the 0.25 mm model, and b) just after fracture of the first elements in the 0.15 mm model. 52
6.6 Simulated results of the SENT tests using a characteristic element length of 0.25 mm: (a) predicted crack propagation in the T7 temper, (b, c, d) Force - SOD curves along with SOD - Surface-Crack-Displacement curves of tempers T4, T6 and T7 respectively. 53
6.7 Simulated results of the SENT tests using a characteristic element length of 0.15 mm: (a) predicted crack propagation in the T7 temper, (b, c, d) Force - SOD curves along with SOD - Surface-Crack-Displacement curves of tempers T4, T6 and T7 respectively. 54
6.8 Evolution of the stress triaxiality and Lode parameter with equivalent plastic strain for elements at the center plane: e1 located at the slit opening surface, e2 located in the second row of elements behind element 1, and e3, located halfway to the specimen center. 56

6.9 Equivalent plastic strain field map on the cracked SENT- specimen from the (top) GTN-T4 simulation and the (bottom) CL-T4 simulation. 57
6.10 Simulated results of the DENT tests using a characteristic element length of 0.15 mm and 0.25 mm(a)predicted crack propagation in the T7 temper, (b, c, d) Force - SOD curves along with SOD - Surface-Crack-Displacement curves of tempers T4, T6 and T7 respectively 59
6.11 Evolution of the stress triaxiality and Lode parameter with equivalent plastic strain for elements at the center plane: e1 located at the slit opening surface, e2 representing the elements located behind element e1, and e3, representing the rest of the elements at the crack path. 61
6.12 Experimental and numerical strain fields at selected slit opening displacements. . . . 62
6.13 Force-displacement comparison between the original and revised model where mesh guidance is included and through thickness symmetry is omitted for the T6 temper . 63
6.14 Crack path on the T6 DENT specimen from a) Experiment, and b) simulations of the full specimen (through-thickness symmetry omitted), c) simulations with a the revised mesh, d) simulations with both full model and revised mesh, and e) simulations with revised mesh and a horizontal velocity. 64
6.15 Numerical results with the revised model, including a horizontal displacement. a) display the horizontal displacement field comparison. (b, c, d) are force-displacement curves and horizontal-vertical displacement curves for (T4, T6, T7) 65
7.1 Test setup of a modified Arcan specimen with a) $= 90°$ and b) $= 45°$, and c) drawing of specimen geometry with measurements in mm. 66
7.2 Experimental and numerical force-displacement curves for the Arcan45 tests in a), c) and e) and corresponding crack paths on the undeformed configuration in b), d) and f). 68
7.3 Experimental and numerical force-displacement curves for the Arcan90 tests, for temper a) T4, b) T6, and c) T7 69
8.1 a) Illustrative drawing of the dropped weight impact test, created by Vetle Espeseth. Geometry of b) impactor with hemispherical tup and c) square target plate with 45° slit, with measurements in mm. 70
8.2 A) Numerical model of the hemispherical impactor and plate and b) Meshed plate, with irregular swept mesh in the predicted crack region. 71
8.3 a)Deformed plate from the T6 drop test simulation and experimental and numerical force-displacement curves for temper b)T4, c)T6 and d)T7. 72
8.4 Experimental and numerical force-displacement curves for the Drop-test for different friction coefficients using temper a)T4, c)T6 and e)T7. [1] 72
A.1 Picture taken of the experimental DENT-test set-up. 79
A.2 The the critical region of the SENT-specimen modelled using a structured mesh of a) h_e=0.25 and b) h_e=0.15 and using an irregular swept mesh combined with c) h_e=0.25 and d) h_e=0.15 80
A.3 The original mesh used for the bulk of numerical simulations of the DENT-test and the revised mesh used to replicate the experimental crack and assess mesh design sensitivity. 80
A.4 Nearly identical force - strain curves for the NT3-T6 temper simulations using distinct combinations of ε_N and f_N of the T6 81

A.5 Illustration of the applied calibration process for the GTN-paramters: a,d,g) Extraction of ε_N at the onset of deviation between experimental force-strain curves and the corresponding FE analysis results of the GTN-model with nucleation omitted. b,e,h) f_N optimization steps. c,f,i) Extraction of the fracture parameters, f_c from the simulated VVF corresponding to the experimental fracture strain. 82
A.6 Force-strain curves and logarithmic strains from experiments and simulations of the NT3 - tensile tests using characteristic element length h_e =0.15mm. 83
A.7 Influence of strain-rate-dependence on the behavior of the smooth specimen. 84
A.8 (left column) Average stress triaxiality and lode parameter of elements in the predicted crack plane having accumulated 20 % of the total predicted damage as a function of the elements position from the slit . (right column) Average equivalent plastic strain of elements as a function of the elements position from the slit. 85
A.9 Experimental and numerical force-strain curves from the SENT-test applying the GTN-model to combined with the structured and irregular mesh using a mesh size (a,c,e)0.25mm (b,d,f) 0.15mm. 86
A.10 Experimental and numerical force-strain curves from the SENT-test applying the CL-model to combined with the structured and irregular mesh using a mesh size (a,c,e)0.25mm (b,d,f) 0.15mm. 87
A.11 Equivalent plastic strain fields on the cracked SENT- specimen from the (top) GTN-T6 simulation and the (bottom) CL-T6 simulation. 88
A.12 Equivalent plastic strain field map on the cracked SENT- specimen from the (top) GTN-T7 simulation and the (bottom) CL-T7 simulation. 88
A.13 Experimental and simulated crack path in the T4 temper using a revised mesh and discarding the thickness symmetry plane.. 89
A.14 Experimental and simulated crack path in the T6 temper using a revised mesh and discarding the thickness symmetry plane. 89
A.15 Representation of the a) Arcan45 and b) Arcan90 model in Abaqus. 90
A.16 Illustrative drawing of the drop weight experiment created by PhD. candidate Vetle Espeseth. 91

List of Symbols

σ'	Deviatoric stress
σ^*	Stress triaxiality
σ_0	Yield strength
σ_{eq}	Equivalent plastic stress
σ_e	engineering stress
σ_t	True stress
σ_y	Yield stress
ε_e	Engineering strain
ε_f	Fracture strain
ε_l	Logarithmic strain
ε_N	Mean strain for nucleation
f	Void volume fraction
f_0	Initial void volume fraction
f_c	Critical void volume fraction
f_n	Void volume fraction
h_e	Characteristic element length
p	Equivalent plastic strain
s_N	Standard deviation
W	Work
W_c	Cockcroft-Latham fracture parameter
L	Lode parameter

1 Introduction

1.1 Background and motivation

Aluminum is a widely used energy absorbent in the automotive industry; bumper beams, crash-boxes, and various body parts are often made of aluminum alloys to absorb energy during collisions. The material is favored for its ductility, moderate strength, and lightweight. The latter has become increasingly important due to increased demands for more fuel-efficient and environmental vehicle[4]. As the industry transitions to electric vehicles, the use of lighter materials such as aluminium is a critical factor in increasing the driving range on a single charge, which is a key criterion in satisfying both environmental regulation and customer preferences. To uphold safety standards and regulation material behavior of car components are validated by physical testing, which is both time consuming and expensive. For this reason the industry is looking more and more to numerical modelling, for faster and more cost efficient design of components and structures. In finite element simulations of components and structures potentially subjected to "collision-like" loading conditions, robust material models describing deformation behavior and progressive failure are needed. To this end, it is desirable for material models to incorporate a dependency on the physical mechanisms that govern the fracture process.

1.2 Previous work

Ductile fracture is the most commonly observed fracture mechanism for aluminum alloys. Three stages characterize this fracture mode: void nucleation, void growth, and finally, void coalescence[2]. Nucleation and void growth have been observed to generate considerable porosity in ductile materials. It has thereby been suggested that this porosity should be accounted for in constitutive models in order to capture the material softening resulting from the degeneration of stiffness contributing material[5]. In traditional porous plasticity models, porosity is accounted for through a representative volume element (RVE) -approach, where the RVE often consists of a pressure-sensitive spherical void inside a matrix material typically modelled as a von Mises material. Using the RVE-approach, the basis for predicting the influence of void growth on material behavior was established in the pioneering work by McClintock in [6], Rice and Tracy in [7], and Gurson in [8]. In [6], McClintock created a fracture criterion by analyzing an expanding cylindrical cavity in a non-hardening material pulled in the direction of its axis while subjected to transverse tensile stresses. In [7], Rice and Tracy considered a spherical void in an infinite matrix of elastically rigid and incompressible plastic material subjected to a remotely uniform stress and strain rate field. Both analyses found an exponential dependence of void growth rate on the hydrostatic stress.

In [8], Gurson expanded on the work by Rice and Tracy and established an approximate yield criterion and flow rules for a material containing voids, where porosity was characterized by a single state variable: the void volume fraction. The yield criterion and flow rules were approximated through an upper limit analysis of a rigid plastic solid with a spherical void. Modifications made by Tvergaard in [9] have since been adopted by the model to obtain improved agreement with more comprehensive data. In the work by Tvergaard and Needleman[10], a failure criterion was added to explicitly account for void coalescence.

The constitutive relations provided by Gurson with modifications by Tvergaard and Needleman, known as the Gurson-Tvergaard-Needleman-(GTN)-model, have been employed in several studies of various aspects of the ductile rupture process. Numerical results using the GTN-model have illustrated the model's capability of describing the physical fracture patterns observed in experiments

of ductile fracture, such as "the cone and cup" fracture surface[10]. The comparison of model predictions with experimental results has demonstrated that when properly calibrated, the GTN-model can predict the onset of ductile fracture in ductile metals with reasonable accuracy [11][12]. Versions of the model which take the plastic anisotropy of the matrix material into account have also been proposed in Dæhli et al. [13]. Dæhli et al. performed 3D unit cell analyses for a wide range of stress states using a heuristic extension of the Gurson-model where an anisotropic yield criterion was incorporated for the matrix material. The model proposed by Dæhli et al. accurately captured the main trends of the unit cell simulations and was thus believed applicable for higher scale simulations where progressive damage due to void growth is desirable. Recent studies by Nahlson and Hutchinson[14], Dunand and Mohr[15], Granum et al.[16], Xue et al. [17] and Dæhli et al. [18] have addressed the limitation of characterizing the critical fracture criterion solely on the basis of stress-triaxiality by incorporating a dependency on the deviatoric stress state through the lode parameter. In [14], shear dependent damage evolution was incorporated by including a softening term dependent on the deviatoric stress.state. By including the term for material softening due to shear in the evolution equation, the physical meaning of the void volume fraction is lost and the parameter is instead considered a damage parameter. As a result the model is able to capture the shear softening due to void distortion and inter-void linking, and thus capable of extending the model use to shear dominated states[14]. Results from simulations demonstrate that when the shear extended model is properly calibrated against a basic set of experiments, it is capable of predicting crack initiation and propagation over a wide range of stress states[17]. Furthermore, the model is able to capture experimental trends recently reported for various structural alloys: i.e. the fracture strain displayed at pure shear can be notably less than those displayed under axisymmetric stress at significantly higher triaxiality [14].

1.3 Objective and aim

The topic of this study is modelling and simulation of crack propagation in 15mm thick AA6016 aluminium alloy plates by use of the GTN model. The main objective is to assess the models accuracy, efficiency and robustness in in predicting fracture and simulating crack propagation under quasi static and dynamic loading conditions. The parameters in the GTN model will be identified based on existing test data for the AA6016 plate material in three different tempers: T4, T6, and T7. The calibrated model will then be employed in numerical simulations of various experimental tests, and the results compared with experimental data for model validation. Quasi-static plate tearing tests will be performed using a specially developed experimental set-up and used for validation of the numerical simulations. In addition, existing test data on dynamically loaded plates of the same aluminium alloy will be used for validation under dynamic loading conditions. Finite element simulations will be performed with Abaqus using solid elements and the GTN model to describe plasticity, damage and fracture. As a benchmark for assessing the performance of the GTN model, a Cockroft-Latham (CL) failure criterion will be calibrated and numerical simulations compared to simulations using the GTN-model.

2 Material mechanics

A detailed characterization of the material is necessary to obtain an accurate and reliable analysis. The first sections of this chapter present the material and its characteristic fracture mode: ductile fracture. Subsequent sections elaborate on the different theories, models, and assumptions used to

define our material model, i.e., yield criteria, flow rules, and work hardening laws. The final sections present various aspects of the finite element method.

2.1 Aluminum alloy

Aluminum is lightweight, ductile, has moderate strength, and is resistant to corrosion. When small amounts of other metals are added, aluminum's strength can be significantly improved without a significant impact on the materials ductility or corrosion resistance. The most common alloying elements used together with aluminum are magnesium, silicon, manganese, zinc, and copper. The density of aluminum is approximately 2.7 g/cm^3, roughly one-third of that of steel (7.8 g/c^3). Given its many advantageous material properties and good formability, aluminum is increasingly used for structural applications in the automotive industry [4]. The main processing advantage of aluminum is its amenability to extrusion amenability to extrusion. Unlike steel, where automotive body structural parts such as roof rails require multiple stampings and weldings, aluminum can be used in single extruded sections. The use of a one-piece extruded section instead of a stamped and welded section can result in tooling and assembly cost reductions. Aluminum also has the advantage of being completely recyclable – without losses in inherent properties –with the energy cost of recycling being only five percent of the energy required for producing the primary metal[19]. Aluminum's drawback is the high energy consumption required for production, which results in high production costs and a negative environmental impact if non-renewable energy sources are used to supply the needed energy.

AA6016

The alloy used in this study, AA6016, is an alloy in the heat-treatable 6xxx series, which contains magnesium and silicone as principal alloying elements. Its chemical composition can be seen in Table. 1. Al-Mg-Si alloys have many positive characteristics, like high strength, good corrosion resistance, and excellent extrudibility[20, 21]. The major strengthening phases in most 6xxx alloys are fine coherent and semi-coherent precipitates based on Mg_2Si. AA6016 is increasingly used as outer panels in automobiles due to properties such as high specific strength, dent resistance, relatively good formability, and surface appearance[22].

Table 1: Chemical composition of AA6016 in wt%

Si	Mg	Fe	Cu	Mn	Cr	Zn	Ti	Al
1.3160	0.3490	0.1617	0.0081	0.0702	0.0025	0.0084	0.0175	Balance

Heat Treatment

The thermal history of the aluminum profile has an important impact on the strength of the material. The material AA6016 is a so-called heat-treatable alloy, which means that the material can be given a thermal treatment to adjust the mechanical properties[21]. In this study, the T4, T6, and T7 tempers were used. The tempers are obtained by solution heat treatment followed by quenching before being naturally or artificially aged into stable condition. In solution heat treatment, the material is heated to a high temperature where precipitates like Mg_2Si are dissolved into the aluminum matrix, and the homogeneous solid-state is reached[19]. The temperature should avoid the eutectic temperature and

be below the melting point. For 6xxx alloys, the solution treatment temperature is between 500° C and 550°C [23]. The main purpose of this treatment is to maximize the volume of hardening solutes like magnesium and silicon in the solid solution of the aluminum matrix[21]. After this treatment, the alloy is rapidly cooled down by water quenching to obtain a supersaturated solution at room temperature[19]. For the T4 temper, the final process is natural aging to stable condition, while the T6 and T7 undergo artificial aging through precipitation heat treatment, resulting in more efficient formations of hardening precipitates. For alloys in the 6xxxx series, the precipitation heat treatment is done at a temperature between 160°C and 205°C, for 1-18 hours[23]. The artificial aging results in an increased yield strength but decreased ductility. The T6 temper is artificially aged to peak strength condition, while the T7 is overaged to stabilized condition. By overaging, strength may be sacrificed to improve properties such as dimensional stability and corrosion resistance[23].

2.2 Fracture mechanisms

The theory on fracture in this section is mostly based on the Third edition Fracture Mechanics book by T.L Anderson [2]. The section presents ductile fracture, which is the most commonly displayed fracture mechanism for aluminium alloys.

2.2.1 Ductile Fracture

Early observations have shown that fractures in ductile solids occurs due to void nucleation, growth, and coalescence [5, 24]. The first stage of ductile fracture involves the nucleation of voids around particles or inclusions, as well as growth of pre-existing voids in the material. Nucleation of voids can occur when the applied stress reaches a critical decohesion stress, causing the interracial bonds between the second-phase particles and matrix material to break, or by fracture of the second-phase particles. Once voids form, continued plastic strain causes the voids to grow and eventually coalesce once a critical size is reached relative to their spacing. The final stage of void coalescence coincides with an abrupt material failure[2]. In materials where second-phase particles and inclusions are well-bounded to the matrix, void nucleation is often the critical step in complete material failure. In contrast, for materials where void nucleation occurs with little difficulty, failure is dictated by growth and coalescence [2]. Figure 2.1 shows the various stages of ductile fracture, where (a), (b), and (c) show how voids grow independently, which can be assumed if the initial void volume fraction is low (<10%), while (d) and (e) illustrates how plastic strain is localized along a sheet of voids, and the formation of local necking instabilities between voids[2].

In uniaxial tensile tests of axisymmetric specimen, the ductile fracture mechanisms result in a “cup and cone” fracture surface. Fig. 2.2 illustrates the process leading to the formation of the distinct fracture surface. In (a), it is shown how the higher hydrostatic stress at the center of the neck compared to the outer region, advances the growth of voids in this region. As the strain increases, the voids grow together and form a penny-shaped flaw, seen in (b), giving rise to deformation bands at 45° from the tensile direction. In the deformation bands, shown in (c), voids nucleate in the finer, more closely spaced particles, such that little growth is needed for instability to develop and subsequent total fracture at 45° angle towards the surface[2].

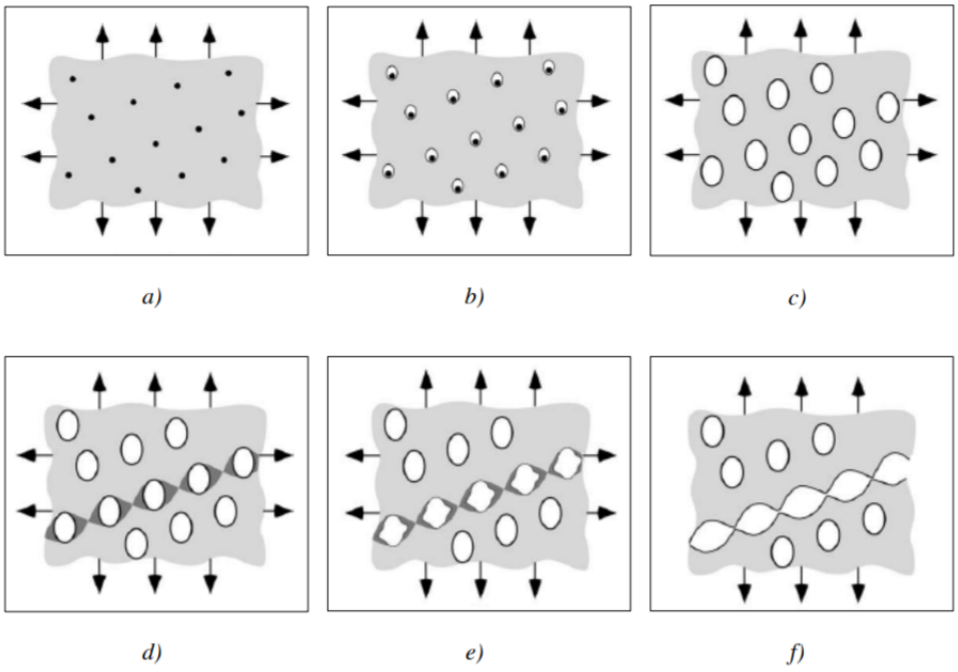

Figure 2.1: Void nucleation, growth, and coalescence in ductile metals: (a) inclusions in a ductile matrix, (b) void nucleation, (c) void growth, (d) strain localization between voids, (e) necking between voids, and (f) void coalescence and fracture[2].

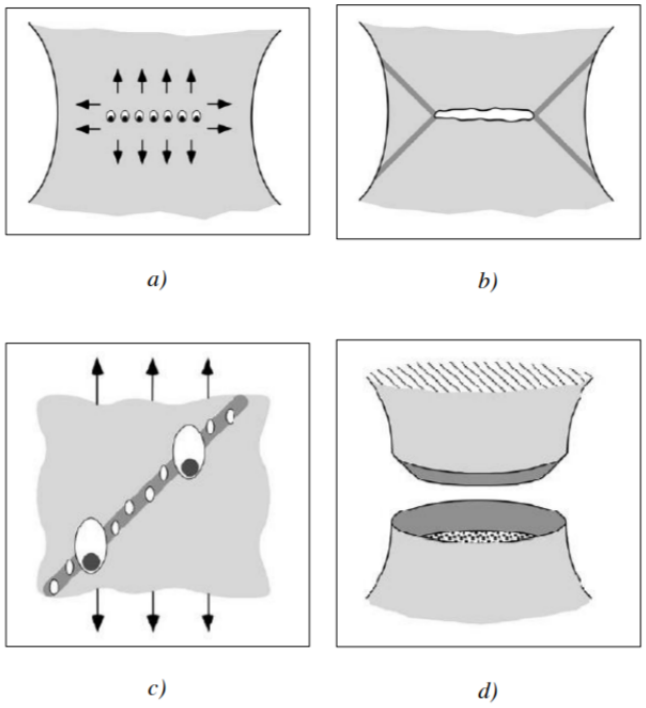

Figure 2.2: Formation of the cup and cone fracture surface in uniaxial tension:(a) void growth in a triaxial stress state, (b) crack and deformation band formation, (c) nucleation at smaller particles along the deformation bands, and (d) cup and cone fracture[2].

Ductile Crack Growth

Ductile crack growth occurs when the stresses and strains near the crack tip reach a critical amount, causing voids to nucleate and eventually link up with the main crack. This process is illustrated Fig. 2.3. The strain exhibits a singularity near the crack tip, but the stresses reach a peak at approximately two times the crack-tip-opening-displacement (CTOD), δ. Nucleation typically occurs when a particle is -2δ from the crack tip, where the stress measure is at its peak, while most of the void growth occurs much closer to the crack tip. Due to the elevated hydrostatic stress environment in front of the crack tip, void nucleation occurs readily; making growth and coalescence critical steps in ductile crack growth[2].

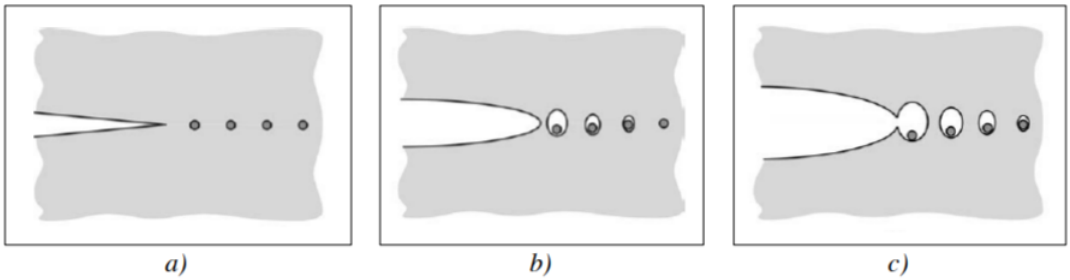

Figure 2.3: Mechanisms for ductile crack growth: (a) initial state, (b) void growth at the crack tip, and (c) coalescence of voids with the crack tip[2].

When an edge crack grows by void coalescence, the crack is observed to propagate in a tunneling mode, where it grows faster in the center of the plate due to higher stress triaxiality. Near the edge of the surface, the crack forms at 45° from the maximum principal stress, producing shear lips visualized in Fig. 2.4. At mid-plane, close examination reveals a zig-zag fracture surface. Under mode I loading conditions, the preferred crack path coincides with the direction of maximum principal stress, 45° from the crack-plane, however, global constraints require that the crack propagation remains in its original plane. The zig-zag fracture surface (as seen in Fig. 2.5) is thus a result of crack propagation reconciling both competing requirements [2].

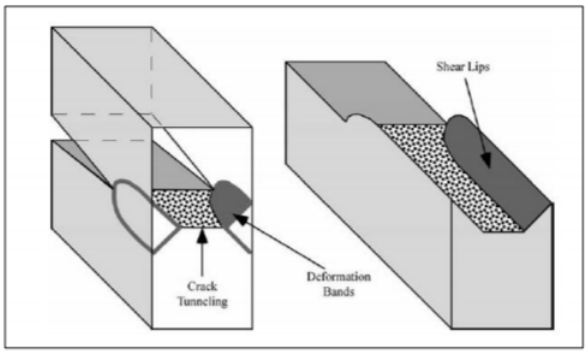

Figure 2.4: Ductile growth of an edge crack[2].

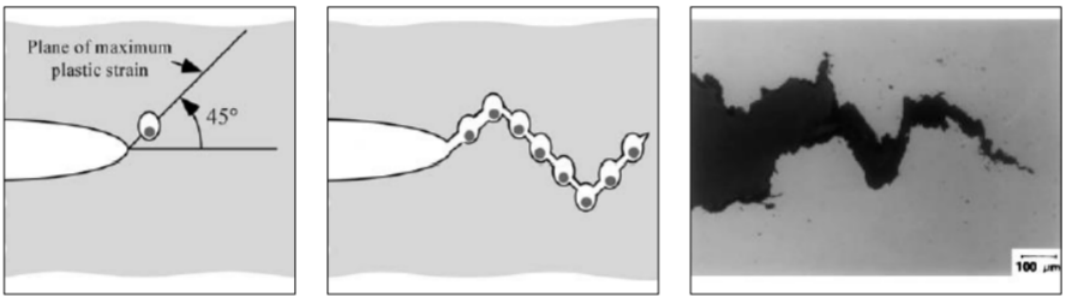

Figure 2.5: Ductile crack growth in a 45° zig-zag pattern.[2]

2.3 Uniaxial tensile test

The primary purpose of conducting a uniaxial tensile test is to find the material's stress-strain relationship. This is achieved by pulling a specimen in tension until fracture, at a quasi-static loading rate. The raw data from a uniaxial tensile test comes in the form of a force-displacement curve. For materials with uniform deformation across the cross-section, the engineering stress, σ_e and engineering strain, ε_e , are calculated as the measured force and displacement over the initial gauge area and length, respectively:

$$\sigma_e = \frac{F}{A_0}, \quad \varepsilon_e = \frac{du_L}{L_0} \tag{2.1}$$

Where the displacement is denoted u_L, forces F, and the initial cross-sectional area and length denoted A_0 and L_0, respectively. The engineering stress-strain states refer to the initial configuration, thus the geometric changes that occur with plastic deformation are not taken into account. To account for these changes, the true stress, σ_t and the work conjugate logarithmic strain, ε_l can be obtained by calculating the stress-strain state by referring to the current configuration

$$\sigma_t = \frac{F}{A} = \sigma_e(1 + \varepsilon_e) \tag{2.2}$$

$$\varepsilon_l = \frac{du_L}{L} = \ln(1 + \varepsilon_e) \tag{2.3}$$

Where A and L are the current gauge cross-section and gauge length, respectively. The defined stress-strain relationship holds when assuming uniform deformation. This is an appropriate assumption for aluminum as the elastic strains are small, and plastic deformation is volume-preserving.

2.3.1 Necking

Ductile materials such as aluminum alloys reach failure when the strain hardening cannot keep up with the reduction in cross-sectional area, and a necking region forms beyond the maximum load. The cross-section where necking occurs decreases quickly with the increasing strain. After necking

occurs, the straining of the specimen is no longer uniform and thus Eq.(2.2) and Eq.(2.3) are no longer valid.

The diffuse necking criterion can be defined by using the result that $\sigma_e = \sigma_t \exp(-\varepsilon_l)$, and that the maximum value of engineering stress is reached at necking, such that $d\sigma_e = 0$. Then,

$$d\sigma_e = d\sigma_t \exp(-\varepsilon_l) + \sigma_t(-d\varepsilon)\exp(-\varepsilon_l) = 0 \tag{2.4}$$

and from we get:

$$\frac{d\sigma_t}{d\varepsilon_l} = \sigma_t \tag{2.5}$$

Equation (2.5) shows that diffuse necking occurs when the slope of the true stress - true strain curve equals the true stress.

2.4 Material modeling

2.4.1 Yield Criterion

The yield criterion expresses the condition for the onset of plastic deformation. Mathematically this is done by defining a yield surface in stress-space i.e., the vector space defined by the components of the stress tensor $\boldsymbol{\sigma}$, by use of a yield function. The yield criterion can be written in terms of the yield function as:

$$f(\sigma) = 0 \tag{2.6}$$

According to the yield criterion, all yielding occurs on the yield surface where $f = 0$, and thus the plastic domain is represented by the yield surface itself. The region inside the yield surface, $f < 0$, represents a stress-state in the elastic domain, whereas the region outside the yield surface, $f > 0$, is defined as an inadmissible region. The yield criterion is illustrated graphically in Fig. 2.6 for a two-dimensional stress-state.

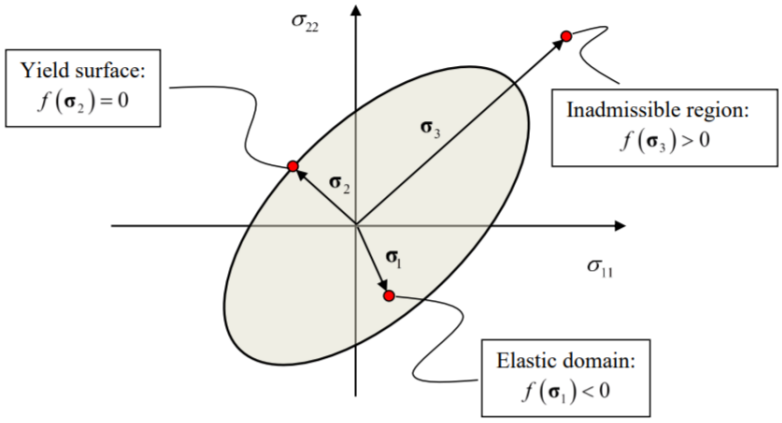

Figure 2.6: Elastic domain, yield surface and inadmissible region for a two-dimensional stress state[3]

The yield function is often written on the form:

$$f(\sigma) = \varphi(\sigma) - \sigma_y \tag{2.7}$$

where $\sigma_{eq} = \varphi(\sigma)$ is the equivalent stress: a measure of the magnitude or intensity of the stress state, and σ_y represents the current yield stress.

The equivalent stress (and thus the function $\varphi(\boldsymbol{\sigma})$) is assumed here to be non-negative, $\varphi(\boldsymbol{\sigma}) \geq 0$, and a positive homogeneous function of order one of the stress, which means that:

$$\varphi(a\boldsymbol{\sigma}) = a\varphi(\boldsymbol{\sigma}) \tag{2.8}$$

where a is a non-negative scalar. By Euler's theorem for homogeneous functions, it then follows that:

$$\sigma_{ij}\frac{\partial\varphi(\boldsymbol{\sigma})}{\partial\sigma_{ij}} = \varphi(\boldsymbol{\sigma}) \tag{2.9}$$

For some materials, like most metals and alloys, the yield criterion can be assumed to depend only on the deviatoric stress state, which is defined as:

$$\sigma'_{ij} = \sigma_{ij} - \sigma_H\delta_{ij} \qquad \text{where} \qquad \sigma_H = \frac{1}{3}\sigma_{kk} = \frac{1}{3}I_\sigma \tag{2.10}$$

where δ_{ij} is the Kronecker delta function (see [25] for more information), σ_H is the hydrostatic stress or mean stress and I_σ is the first principle invariant of the stress tensor (see [3] for more information).

Materials which only depend on the stress deviator are said to be pressure insensitive. For pressure insensitive materials, plastic deformation is for the most part observed to take place by plastic slip, which is a shear-driven deformation mode. For pressure-independent materials, we may express the yield function in the form:

$$f(\boldsymbol{\sigma'}) = 0 \tag{2.11}$$

For pressure sensitive materials such as friction materials: concrete, soil and rock, and porous materials, plastic deformation is also dependent on the hydrostatic stress. To underline this sensitivity the yield criterion can be written as:

$$f(\boldsymbol{\sigma'}, \sigma_H) = 0 \tag{2.12}$$

The plastic yielding of materials can often be assumed to be isotropic, meaning that the yield function is independent of the direction of the loading within the material. This is for example the case for polycrystalline metals and alloys with random texture, i.e., the grains have arbitrary orientation in space. For isotropic materials the yield function should depend only on either the principal stresses $(\sigma_1, \sigma_2, \sigma_3)$ or the principal invariants of the stress tensor $(I_\sigma, II_\sigma, III_\sigma)$.

For an isotropic pressure independent material the yield criterion is most conveniently written in terms of the principal invariants of the stress deviator, namely: $f(J_2, J_3) = 0$. If instead the material is isotropic and pressure dependent, we may express the yield criterion in terms of the invariants of the deviatoric stress tensor in addition to the first principle invariant of the stress tensor: $f(I_\sigma, J_2, J_3) = 0$.

2.4.2 Von Mises Yield Criterion

The von Mises criterion is an isotropic and pressure insensitive yield criterion, used for isotropic materials. Of the many isotropic pressure insensitive yield criteria, the von Mises yield criterion is used almost exclusively for structural impact simulations [26]. The yield function is conveniently expressed in terms of the second principle invariant of the stress deviator [26]:

$$J_2 = \frac{1}{2}\sigma'_{ij}\sigma'_{ij} \tag{2.13}$$

In the von Mises yield criterion, yielding occurs when the second invariant of the deviatoric stress tensor J_2 reaches a critical value k [26], where k equals the yield stress of the material in pure shear: $k = \frac{\sigma_y}{\sqrt{3}}$. The criterion can thus be written as:

$$f(J_2) = \sqrt{J_2} - \frac{\sigma_y}{\sqrt{3}} \tag{2.14}$$

which can be rewritten in terms of the deviatoric stress as:

$$f = \sqrt{\frac{3}{2}\sigma'_{ij}\sigma'_{ij}} - \sigma_y = 0 \tag{2.15}$$

Once the deviatoric stresses reach a critical value such that Eq.(2.15) is met, a further increase stresses requires an increase in the yield stress, σ_y, to not violate the yield criteria. Consequently, σ_y is itself a function dependent on the equivalent plastic strain measure, p, which will be elaborated further in sec.2.4.4.

2.4.3 Plastic flow rule

Whereas the yield function determines the onset of plastic deformation, the flow rule defines the plastic straining by the use of a plastic flow potential, $g(\sigma_{ij})$. The general form of the plastic flow rule is written as:

$$\dot{\varepsilon}^p_{ij} = \dot{\lambda}\frac{\partial g}{\partial \sigma_{ij}} \tag{2.16}$$

Where the multiplier, $\dot{\lambda}$, is here called the plastic parameter. To not violate the second-law of thermodynamics, the plastic potential, g must be defined in a way that ensures non-negative plastic dissipation. Analogous to the equivalent stress (see Eq. (2.9)), the plastic potential function is assumed a positive homogeneous function of order one of the stress tensor. Euler's theorem then assures that

$$\sigma_{ij}\frac{\partial g}{\partial \sigma_{ij}} = g \tag{2.17}$$

The plastic dissipation is then given by:

$$\mathfrak{D}_\mathfrak{p} = \sigma_{ij}\dot{\varepsilon}^p_{ij} = \dot{\lambda}\sigma_{ij}\frac{\partial g}{\partial \sigma_{ij}} = \dot{\lambda}g \geq 0 \tag{2.18}$$

From Eq. (2.18) it is seen that for all $\lambda \neq 0$, the plastic potential function must fulfill $g \geq 0$. One particular choice is to assume the plastic the plastic potential is defined by the yield function f:

$$\dot{\varepsilon}^p_{ij} = \dot{\lambda}\frac{\partial f}{\partial \sigma_{ij}} \tag{2.19}$$

This is then called the associated flow rule. Since the yield function is also a positive homogeneous function of the stress tensor of order one, the requirement of non-negative plastic dissipation is fullfilled.

$$\mathfrak{D}_\mathfrak{p} = \sigma_{ij}\dot{\varepsilon}^p_{ij} = \dot{\lambda}\sigma_{ij}\frac{\partial f}{\partial \sigma_{ij}} = \dot{\lambda}\sigma_{ij}\frac{\partial \varphi}{\partial \sigma_{ij}} = \dot{\lambda}\varphi \geq 0$$

For a von Mises material, it is seen from Eq.(2.18) that the plastic multiplier, λ corresponds to the equivalent plastic strain.

$$\sigma_{ij}\dot{\varepsilon}^p_{ij} = \sigma_{eq}\dot{p} \tag{2.20}$$

The plastic flow rule can the be derived as:

$$\dot{\varepsilon}^p_{ij} = \dot{p}\frac{\partial \sigma_{eq}}{\partial \sigma_{ij}} = \dot{p}\frac{3}{2}\frac{\sigma'_{ij}}{\sigma_{eq}} \tag{2.21}$$

Using Eq. (2.21), the equivalent plastic strain increment for a von Mises material can conveniently be written as:

$$\dot{p} = \sqrt{\frac{2}{3}\dot{\varepsilon}^p_{ij}\dot{\varepsilon}^p_{ij}} \tag{2.22}$$

If we consider the symmetric tensors as vectors in a six-dimensional vector space, the associated flow rule implies that the plastic strain increment vector $d\varepsilon_p = \dot{\varepsilon}^p dt$ is parallel to the gradient of the yield surface at $\boldsymbol{\sigma}$ and thus directed along the outward normal of the surface at this point. The associated flow rule is therefore also called the normality rule. This property is visualized for the Tresca and von Mises yield surfaces in Fig. 2.7.

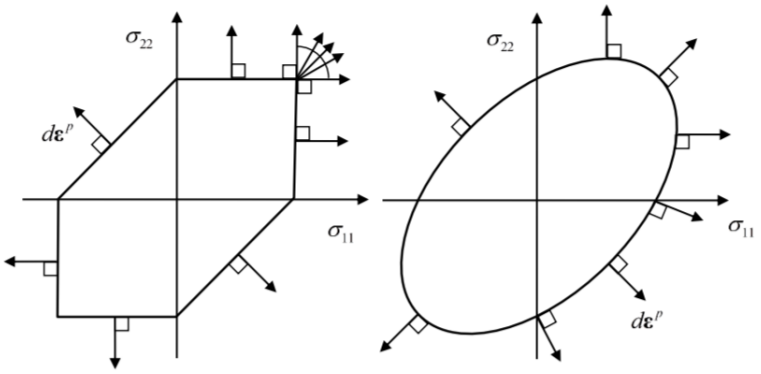

Figure 2.7: Geometric representation of the associated flow rule for Tresca and von Mises yield surfaces. The associated flow rule implies that the incremental plastic strain vector is normal to the yield locus.[3]

It is important to note that the normality rule implies that the shape of the yield surface not only determines the stress state at which yielding initiates, but also the direction of the plastic flow. The normality rule is also derived from the postulate of maximum plastic dissipation, which is represented by the inequality:

$$(\boldsymbol{\sigma} - \hat{\boldsymbol{\sigma}})\dot{\varepsilon}^p \geq 0 \tag{2.23}$$

Supposing that the yield surface is smooth — so that a well-defined tangent hyperplane and normal direction exist at every point — it is clear that for Eq. (2.23) to be true for all $\hat{\boldsymbol{\sigma}}$, not only must $\dot{\varepsilon}^p$ be directed along the outward normal of the yield surface, but all values for $\hat{\boldsymbol{\sigma}}$ must lie on the inward side of the tangent to the yield surface, thus forcing the yield surface to be convex.[27] This is graphically illustrated in Fig. 2.8

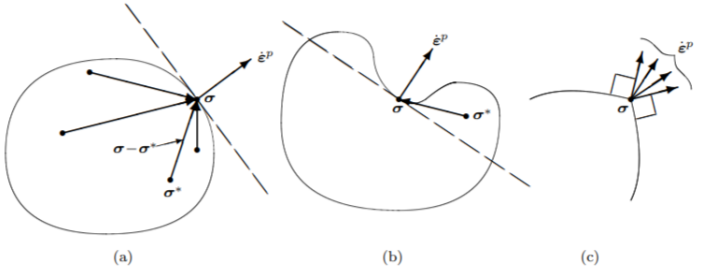

Figure 2.8: Consequences of the principle of maximum plastic dissipation: normality of the plastic flow and convexity of the yield surface. [3]

2.4.4 Hardening Rules

As the material is plastically deformed, work-hardening occurs, making the material stronger. This reflects on the yield function, since the elastic domain expands during work-hardening. A specification of the dependence of the yield criterion on internal variables describing the material hardening properties, along with the rate equations of these variables, is called a hardening rule. One way to account for work-hardening is to let the yield stress σ_y depend on the plastic straining. This is called isotropic hardening. Another way is to let the elastic domain translate in stress space in direction of the plastic straining. This is called kinematic hardening, and is especially important for cyclic loading (loading, unloading and reloading in the reverse direction) or non-proportional (not following a straight line in stress space) loading paths. To describe work-hardening, we need to introduce internal variables with evolution equations, which reflect the changes of the microstructure of the material as a result of plastic straining.

Isotropic Hardening

To account for isotropic hardening, the current yield stress depends on the internal hardening variable: R, the yield criterion can then be written:

$$f = \varphi - \sigma_y(R) = \varphi - (\sigma_0 + R) \leq 0 \tag{2.24}$$

As the material is plastically deformed, the isotropic hardening variable R increases such that the flow stress σ_y increases, resulting in an expansion of the elastic domain in stress space. As work-hardening occurs in conjunction with plastic deformation, the hardening variable R is typically assumed to be dependent on the equivalent plastic strain p, the energy conjugate to the equivalent stress. Two commonly used isotropic hardening rules are the Voce hardening rule and the Power law. The constitutive relations of the Power law and Voce hardening rule are written as:

$$\textit{Power law:} \quad R(p) = Kp^n \tag{2.25}$$

$$\text{Voce hardening rule:} \quad R(p) = \sum_{i=1}^{N_R} Q_i(1 - \exp(-C_i p)) \tag{2.26}$$

where σ_{eq} and p are the equivalent stress and equivalent plastic strain respectively, and K, n and Q_i, C_i for $i = 1, 2, .., N_R$ are model constants for the Power law and Voce hardening rule respectively.

Whereas the Power law increases indefinitely with increasing plastic strain, the Voce hardening rule saturates, making the Voce rule advantageous when modeling aluminum alloys where the stress-strain state saturates for high levels of strain. In this study an extended Voce hardening rule with with three terms was utilized to describe the work hardening.

$$R(p) = \sum_{i=1}^{3} Q_i(1 - \exp(-C_i p)) \tag{2.27}$$

where the hardening terms R_i saturate at different levels of plastic strain. The hardening parameters Q_i and C_i represent the value and rate of saturation respectively i.e. a high value of C_i implies that the maximum value Q_i is reached at a low strain rate, and vice versa. It is assumed that $C_1 \geq C_2 \geq C_3$ such that R_1 saturates at the lowest strain and R_3 at high strain level.

2.4.5 Ductile failure criterion

Ductile failure criteria typically model failure through an accumulative damage variable. This damage variable can either be coupled or uncoupled with the constitutive relations. For criteria using the coupled approach, such as porous plasticity models, the influence of damage is included in the constitutive equations. In contrast, uncoupled damage criteria have no damage effect on the constitutive equations, i.e., the yield criterion, and plastic flow are unaffected by the evolution of damage. While a coupled approach is, in general, based on a more sound physical theory, parameter identification is usually more cumbersome. With an uncoupled criterion, parameter identification can be conducted independently of the plasticity model, thus simplifying the calibration process. Uncoupled criteria are therefore widely used to model failure in ductile materials [28]. A widely used uncoupled failure criterion was presented by Cockroft and Latham in[29]. The failure criterion was given on a form analogous to the work done per unit volume at the point of fracture, where the yield stress was replaced with the principle stress, σ_1, to account for the effects of the hydrostatic stress.

$$W_c = \int_0^{p_f} \max(\sigma_1, 0)\, dp \tag{2.28}$$

For a given temperature and strain rate fracture is said to occur when the highest principle stress integrated over the strain path reaches a critical value, W_c. In Abaqus the CL-failure criterion is

implemented on the form, Eq.(2.29), through an in-house user defined subroutine (VUSDFLD), where failure is assumed to occur when $w = 1$.

$$w = \frac{1}{W_c} \int_0^p \max(\sigma_1, 0)\, dp \tag{2.29}$$

This criterion has since its introduction been used in many studies to describe ductile fracture, e.g., [30, 31]. Calibrated for a given material, the CL fracture criteria implicitly express the equivalent plastic strain at fracture, as a decreasing function of the hydrostatic stress (assuming a constant value of the Lode parameter). This is coherent with micro-mechanical theory, since void growth increases with increased hydrostatic pressure[2].

It is often convenient to express the degree of hydrostatic stress or. deviatoric stress at given stress-state. This is done by introducing the dimensionless stress-invariants known as the stress-triaxiality, σ^* and the lode parameter, L.

$$\sigma^* = \frac{\sigma_H}{\sigma_{eq}} = \frac{I_1}{3\,\sigma_{eq}} \qquad \text{and} \quad L = \frac{2\sigma_2 - \sigma_1 - \sigma_3}{\sigma_1 - \sigma_3} \tag{2.30}$$

By expressing the the principle stress as a function of the Lode parameter, L, and the stress triaxiality, σ^*, and the equivalent stress, σ_{eq}, the CL-criterion can be rewritten as:

$$w = \frac{1}{W_c} \int_0^p \max(\sigma^* - \frac{3 - L}{3\sqrt{3 + L^2}}, 0)\sigma_{eq}\, dp \tag{2.31}$$

From Eq. (2.31) it is seen that damage evolves faster at high stress triaxialities. With regards to the Lode parameter it is seen that damage evolves faster for generalized tension L = -1, than for generalized compression: L = 1, with generalized shear: L= 0 , somewhere in between[3].

2.4.6 Anisotropy

Crystallographic textures caused by manufacturing processes such as extrusion and rolling processes — which are common for aluminum alloys — can result in anisotropic properties that are not accurately represented using an isotropic yield function. In these cases, implementing an anisotropic yield function usually produces more accurate solutions [32–34]. To determine whether an isotropic or anisotropy yield criterion is appropriate, the degree of anisotropy must be assessed. Assuming plastic incompressibility, the degree of anisotropy can be defined in terms of the ratio between the plastic strains in different directions. This is defined as the R-ratio, which in α-direction relative to the extrusion direction is given by[35]:

$$R_\alpha = \frac{\epsilon_w^p}{\epsilon_t^p} \tag{2.32}$$

where the material is said to be isotropic if Eq. (2.32) is equal to unity for all directions α.

2.5 Porous plasticity

The desire for using a porous plasticity model emanates from observations of the significant void growth generated within the material through the ductile fracture process. Modeling of this type of material is often attempted using homogenized micro mechanically motivated material models referred to as porous plasticity models. These models can capture the material softening at a

homogenized level through the evolution of some microstructural variable included in the model. Perhaps the best-known model founded on a micro-mechanical basis was proposed in the seminal work of Gurson [8]. The model assumes a homogeneous material consisting of pressure-sensitive voids in a plastic incompressible matrix, where softening occurs by the evolution of the void volume fraction. The model's attractiveness resides in the simple closed-form formulation of the yield function and simple implementation [13].

2.5.1 Gurson's Porous Plasticity Model

Gurson establish an approximate yield criterion and normal flow rule, using the upper bound theorem of plasticity and a simple rigid-plastic material model. For simplicity, the void-matrix aggregate was idealized as a single spherical void in a rigid plastic cell, illustrated in Fig. 2.9.

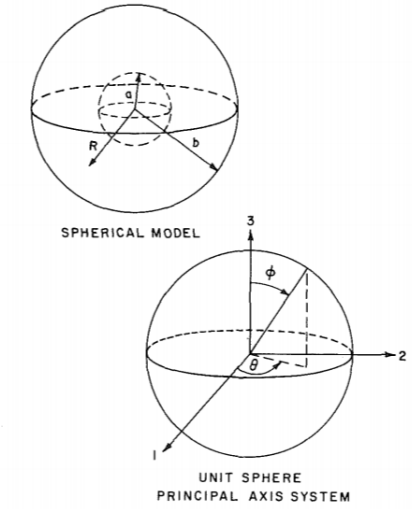

Figure 2.9: Spherical void shape geometry with outer cell wall centered around the void.

The cell was presumed to behave under loading as the aggregate would, exhibiting void growth when undergoing yield with a positive hydrostatic component of macroscopic stress. The matrix was characterized as a perfect plastic von Mises material, such that the yield criterion can be written analogous to Eq.(2.15), while the flow relation can be determined by substituting Eq.(2.22) into Eq. (2.21), giving:

$$\sigma'_{ij} = \frac{2}{3}\frac{\sigma_y}{\sqrt{\frac{3}{2}\dot{\varepsilon}_{kl}\dot{\varepsilon}_{kl}}}\dot{\varepsilon}_{ij} \tag{2.33}$$

Where it is used that σ_{eq} in a perfectly plastic material is given as σ_y. Furthermore, the strain increment of the matrix material is given as:

$$\dot{\varepsilon}_{ij} = \frac{1}{2}\left(\frac{\partial v_i}{\partial x_j} + \frac{\partial v_j}{\partial x_i}\right) \quad , \quad \dot{\varepsilon}_{kk} = 0 \tag{2.34}$$

Here v_i is the microscopic velocity field, and x_i is the position of a material point in Cartesian coordinates. The macroscopic rate of deformation of the aggregate was then defined in terms of the

microscopic velocity field at the unit sphere surface:

$$\dot{E}_{ij} = \frac{1}{V}\frac{1}{2}\int_S (v_i n_j + v_j n_i)\, dS \tag{2.35}$$

Where n_i is a vector unit normal, and S is the surface of the sphere. By applying Greens theorem and the divergence theorem, the macroscopic deformation was written on the form:

$$\dot{E}_{ij} = \frac{1}{V}\left[\int\limits_{V_{matrix}} \dot{\varepsilon}_{ij}\, dV + \int\limits_{V void} \dot{\varepsilon}_{ij}\, dV\right] = \frac{1}{V}\int\limits_{V_{matrix}} \dot{\varepsilon}_{ij}\, dV + \frac{1}{V}\frac{1}{2}\int\limits_{S_{void}} (v_i n_j + v_j n_i)\, dS \tag{2.36}$$

The velocity field, v_i , was required to obey compatibility and meet kinematic boundary conditions on the sphere surface, which correspond to the prescribed macroscopic rates of deformation. Furthermore, the velocity field throughout the aggregate was required to be continuous and have continuous first derivatives. Of the many velocity fields full-filling the these conditions, the actual velocity field, v_i^A would be characterized by its generation of the minimum dissipation:

$$\dot{W} = \frac{1}{V}\int_V \sigma'_{ij}(\dot{\boldsymbol{\varepsilon}})\dot{\varepsilon}_{ij}\, dV \tag{2.37}$$

Normality and convexity is established for the actual yield loci, defined by the actual macroscopic stress,Σ_{ij}^A , by utilizing Bishop and Hill's proof that the Σ_{ij}^A is the work conjugate of $\dot{E}_{ij}$ [36]. This was proven for Σij^A defined as the area average of σ_{ij}^A over a plane section of the aggregate and assuming no correlation between the microscopic stress components and the microscopic displacements.

$$\Sigma_{ij}^A = \frac{1}{A}\int\limits_S \sigma_{ij}^A\, dS \;\rightarrow\; \dot{W}^A = \Sigma_{ij}^A \dot{E}_{ij} \tag{2.38}$$

The principle of virtual work was then proved on a macroscale for Σ^A: $(\Sigma_{ij}^A - \Sigma_{ij}^*)\,\dot{E}_{ij} \geq 0$, via the principle of virtual work. From the principle of virtual work and Eq. (2.38) it follows that:

$$\delta\dot{W}^A = \delta\Sigma_{ij}^A\,\dot{E}_{ij} + \Sigma_{ij}^A\,\delta\dot{E}_{ij} \tag{2.39}$$

$$\delta\Sigma_{ij}^A = 0 \text{ by normality} \tag{2.40}$$

giving:

$$\Sigma_{ij}^A = \frac{\partial \dot{W}^A}{\partial \dot{E}_{ij}} \tag{2.41}$$

The approximate macroscopic stress needed to cause yielding was then defined analogous to Eq.(2.41):

$$\Sigma_{ij} = \frac{\partial \dot{W}}{\partial \dot{E}_{ij}} = \int_V \sigma'_{kl}(\dot{\boldsymbol{\varepsilon}})\frac{\partial \dot{\varepsilon}_{kl}}{\partial \dot{E}_{ij}}\, dV \tag{2.42}$$

By considering a velocity field on the form $v_i = v_i(\dot{E}_{ij}, f, x)$ and homogeneous of degree one in the component of $\dot{E}_{ij}$, $\dot{\varepsilon}_{ij}$ and $\dot{W}$ would also be homogeneous of degree one in $\dot{E}_{ij}$, such that:

$$\dot{W} = \frac{\partial \dot{W}}{\partial \dot{E}_{ij}}\dot{E}_{ij} \tag{2.43}$$

Utilizing the maximum plastic work principle on the microscopic level established in [36]: $(\sigma'_{ij}(\dot{\boldsymbol{\varepsilon}}) - \sigma'^{*}_{ij}(\dot{\boldsymbol{\varepsilon}})\, d\varepsilon \geq 0$ to set one part of the integrand to zero, and Eq. (2.43) we get:

$$\Sigma_{ij}\, \dot{E}ij = \frac{\partial \dot{W}}{\partial \dot{E}_{ij}} \dot{E}ij = \dot{W} \tag{2.44}$$

Thus by Eq.(2.44), Σ_{ij} is the the work conjugate to $\dot{E}_{ij}$ as is Σij^{A}, such that normality is established for the approximate yield locus derived using Eq (2.42) for all possible directions of $\dot{E}_{ij}$. The yield locus was then proven to lie outside the actual yield locus in stress space by using the result that the actual velocity field, v^{A}, is characterized by its generation of the minimum dissipation, $\dot{W}$. .The principle of maximum plastic work could then be rewritten on the form:

$$(\Sigma_{ij} - \Sigma^{A}_{ij})\dot{E}_{ij} = \frac{1}{V}\int_{V} (\sigma'_{ij}(\dot{\boldsymbol{\varepsilon}}) - \sigma'_{ij}(\dot{\boldsymbol{\varepsilon}}^{A}))\dot{\varepsilon}_{ij} dV \geq 0 \tag{2.45}$$

Since $\dot{E}_{ij}$ is the outward normal to both the Σ_{ij} and Σ^{A}_{ij} yield loci, the Σ_{ij} surface always lies on or outside the Σ^{A}_{ij} surface; and is thus an upper bound approximation to Σ^{A}_{ij}.

By determining an appropriate field velocity for the spherical void matrix aggregate (see [8]), the resulting approximate yield function,Φ, found by Gurson was given on the form:

$$\Phi = \left(\frac{\sigma_{eq}}{\sigma_y}\right)^{2} + 2f\cosh\left(\frac{3\sigma_H}{2\sigma_y}\right) - 1 - f^{2} = 0 \tag{2.46}$$

Where

$$\sigma_{eq} = \text{macroscopic von Mises stress} \tag{2.47}$$
$$\sigma_H = \text{macroscopic hydrostatic stress} \tag{2.48}$$
$$\sigma_y = \text{flow stress for the matrix material of the cell} \tag{2.49}$$
$$f = \text{void volume fraction} \tag{2.50}$$

The approximate yield function incorporates porosity dependence by introducing the void volume fraction f into the yield criterion, which has the effect of introducing strain-softening. It can be seen that by setting $f = 0$, the von Mises yield criterion is recovered, as defined in sec. 2.4.2. Subsequent studies by Tvegaard [37] found that the material model overestimated the critical strain for localization at various loading conditions. Tvergaard's study led to a simple modification of the original Gurson model, after it was shown that adding three parameters to the yield function: q_1, q_2, and q_3, enhanced the model's predictions for various loading conditions.

$$\Phi = \left(\frac{\sigma_{eq}}{\sigma_y}\right)^{2} + 2q_1 f\cosh\left(\frac{3q_2\sigma_H}{2\sigma_y}\right) - (1 + q_3 f^{2}) \tag{2.51}$$

The values $q_1 = 1.5$ $q_2 = 1$, $q_3 = (q_1)^2$ are often found in literature after they were shown in [37] to consistently give better results. The associated flow rule is adopted herein, and the macroscopic plastic rate-of-deformation tensor is thus given by:

$$\dot{\varepsilon}^{p}_{ij} = \dot{\lambda}\frac{\partial \Phi}{\partial \sigma_{eq}} \tag{2.52}$$

where $\lambda \geq 0$ is the plastic multiplier. The equivalence in plastic power provides a relation for the equivalent plastic strain rate on the form:

$$\sigma_{eq}\,\varepsilon^p_{ij} = (1-f)\,\sigma_y\,\dot{p} \rightarrow \dot{p} = \frac{\sigma_{eq}\varepsilon^p_{ij}}{(1-f)\sigma_y} \tag{2.53}$$

The loading-unloading conditions of the rate-independent porous plasticity formulation reads:

$$\Phi \leq 0 \quad , \quad \dot{\lambda} \geq 0 \quad , \quad \Phi\,\dot{\lambda} = 0 \tag{2.54}$$

Damage evolution coincides with the change in void volume fraction, which during an increment of deformation is written as:

$$\dot{f} = (1-f)\dot{\varepsilon}^p_{kk} + \Lambda\dot{\varepsilon}^p_{eq} \quad \text{where} \quad \dot{\varepsilon}^p_{eq} = \sqrt{\frac{2}{3}d\,\dot{\varepsilon}^p_{ij}\dot{\varepsilon}^p_{ij}} \tag{2.55}$$

Here, the first term defines the growth rate of the preexisting voids and the second term quantifies the contribution of new voids that are nucleated with plastic strain. The scaling coefficient Λ is chosen so that nucleation follows a normal distribution as suggested by Chu and Needleman in [38]: the strain at which voids nucleate is distributed in a normal fashion about a specified mean strain. Then, with a void volume fraction of nucleating particles, f_N, a mean strain for nucleation ε_N and a standard deviation, s_N, Λ is given by:

$$\Lambda = \frac{f_N}{s_N\sqrt{2\pi}}\exp\left[-\frac{1}{2}\left(\frac{\varepsilon^p_{eq}-\varepsilon_N}{s_N}\right)^2\right] \tag{2.56}$$

The model contains a failure criterion where ductile fracture is assumed to occur as the void fraction reaches a critical value f_c. A typical assumption for metals is $f_c = 0.15$ [2]. Tvergaard and Needleman [10] proposed a modified failure criterion to account for the complete loss of material stress-carrying capacity due to the coalescence of voids, which was not predicted at a realistic level of the void volume fraction by Gurson's equations. The modified failure criterion was introduced by replacing the current void volume fraction, f with an effective void volume fraction, f^*:

$$f^* = \begin{cases} f & \text{for } f \leq f_c \\ f_c + \frac{f^*_u - f_c}{f_F - f_c}(f - f_c) & \text{for } f > f_c \end{cases} \tag{2.57}$$

Where f_c , f_F , and f^*_u are fitting parameters. Here the ultimate value, f^*_u, at which the macroscopic stress carrying capacity vanishes, is given by $f_u = \frac{1}{q_1}$, when $q_3 = q_1^2$. When $f > f_c$, the damage caused by hydrostatic stress is amplified, accelerating the onset of material failure. The modified failure criterion was shown by Tvergaard and Needleman [10] to improve the accuracy of the model; however, it should be weighed whether the benefit of applying Eq.(2.57)) is offset by the need to define the additional parameters. Because failure in real materials is very abrupt with minimal straining after the critical void volume fraction is exceeded, failure criteria consisting of f_c alone can be considered reasonable [2].

2.6 Finite element method (FEM)

All numerical simulations in this thesis were done in the finite element analysis (FEA) software Abaqus/CAE. This section presents a brief introduction of the relevant theory behind the models used in the Abaqus code. In this study Abaqus Explicit – which employs an explicit integration scheme to solve for displacements – was used exclusively.

2.7 Explicit analysis

In the finite element method (FEM), a continuous problem is discretized into elements, and solved using numerical schemes. There are two different direct integration schemes available for solving dynamic problems; Explicit, where the solution is obtained in terms of known quantities, and implicit, where the solution is obtained from unknown quantities. In Abaqus, the explicit dynamics analysis procedure is based on implementing an explicit integration rule: the central difference method, together with using a lumped element mass matrix, i.e., a diagonal mass matrix [39] to solve the governing equation of of motion (see appendix).

The implicit method is unconditionally stable, but the central-difference method is only conditionally stable and the time step has to be limited. However, in contrast to the implicit integration scheme, explicit integration does not require equation solving, nor equilibrium iterations. This makes each time increment computationally less expensive, despite requiring very small time steps, and convergence is not an issue. The result is that the explicit method is preferable when solving discontinuous non-linear problems such as material failure and contact, and makes it ideal for high-speed dynamic simulations where small time-increments are required[40]. The stable time increment is determined from the dilational wave speed: C_d.

$$\Delta t_{cr} \quad = \alpha \frac{2}{w_{max}} \approx \alpha \frac{h_{e,min}}{C_d} = \alpha \frac{h_{e,min}}{\sqrt{\frac{E}{p}}} \tag{2.58}$$

Where w_{max} denotes the highest frequency of the system, $h_{e,min}$ is the smallest element length in the model, C_d is the speed of a dilated stress wave in the material and α is the Courant number. According to [41], typical values of α is between 0.8 and 9.8. Under this interpretation, the time increment should be smaller than the time it takes a dilated stress wave to propagate the smallest element in the model. A consequence of needing to use very small time increments to ensure stability is that modeling quasi-static problems in their natural period is highly impractical. So when quasi-static problems are to be modeled using Abaqus/Explicit, the prerequisite of small time increments needs to be overcome by artificially speeding up the simulation. This is achieved through time or mass-scaling. Time-scaling achieves this by increasing the loading rate, while mass scaling artificially increases the density of the material to allow larger time steps (see Eq. (2.58)). As increasing the loading rate will increase the strain rate, mass-scaling should be used for strain-rate sensitive models so long as inertia effects are negligible i.e. quasi static tests. Increasing the loading rate can introduce artificial kinetic energy (KE) into the system. To refute any unwanted dynamic effects in the solution, an energy balance check is critical.

2.7.1 Energy balance

Time steps that fulfills Eq. (2.58) is not always sufficient for nonlinear problems, as the criterion is based on stability analysis for linear equations of motion. It is therefor recommended to always perform an energy balance check to detect possible instabilities that lead to spurious energy generation. Energy conservation implies Eq. (2.59)

$$\mid W^{kin}_{n+1} + W^{int}_{n+1} - W^{ext}_{n+1} \mid \leq \xi max(W^{kin}_{n+1}, W^{int}_{n+1}, W^{ext}_{n+1}) \tag{2.59}$$

where W^{kin}_{n+1} is kinetic, W^{int}_{n+1} internal and W^{ext}_{n+1} external energy at t_{n+1} . ξ is a tolerance, typically of the order of 10^{-2} according to [40]. If Eq. (2.59) is not fulfilled throughout the simulations,

the numerical results should be disregarded as numerical instability may be dissipated by energy-dissipating nonlinear behaviors (e.g., work hardening) making artificially introduced energy difficult to detect [40]. This is in contrast to linear problems, where numerical instability is usually easy to detect because the solution grows without limit.

2.8 Contact

A contact condition is a special class of discontinuous nonlinear constraints that allow forces to be transmitted from one part of the model to another. There are many methods of enforcing contact, notably the Lagrange multiplier method and the penalty method. Whereas Abaqus/standard allows for contact to be enforced using both methods, Abaqus/Explicit only allows for the penalty method. In contrast to the Lagrange multiplier method, the penalty method enforces contact without introducing additional unknowns into the equation system but may in some cases produce an ill-conditioned set of equations[40]. Two algorithms are provided in Abaqus/Explicit for modeling contact; General contact and contact pairs. General contact allows a definition of contact between many or all regions of a model with a single interaction. This interaction typically includes all bodies in the model and requires very few restrictions on the types of surfaces involved. The surfaces involved in the contact domain can also be disconnected. Contact pairs describe the contact between two surfaces. This algorithm requires a more careful definition of contact since every possible contact pair must be defined, and it has many restrictions on the types of surfaces involved. The interactions must be defined by specifying each of the individual surface pairs that can interact with each other[40].

3 Experimental study

An experimental study was conducted on double edge notch tension (DENT) specimens cut from cold-rolled AA6016 aluminum alloy plates, produced by Hydro Aluminium. The experimental setup and results are presented in this chapter, along with previously conducted studies that have been used for parameter identification and model validation. The previous experiments include uniaxial tensile testes on smooth and notched specimens and single edge notched tension (SENT)-tests conducted by PhD. candidate Vetle Espeseth in [1]. The geometries for each specimen are display in Fig. 3.1

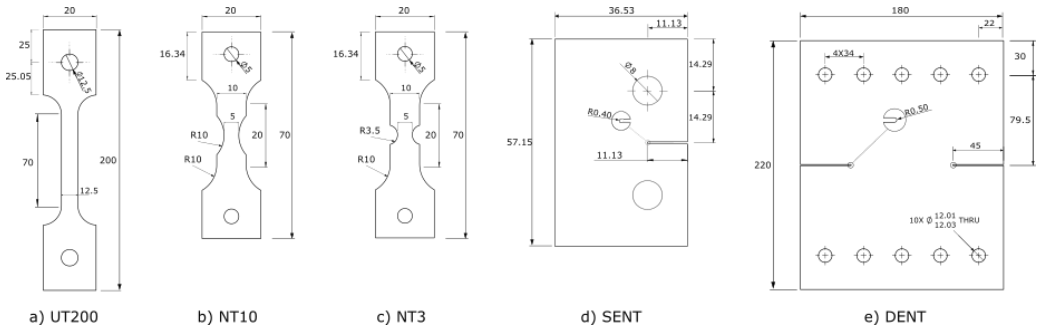

Figure 3.1: Geometry of test specimens with measures in mm: (a) uniaxial tension, (b) and (c) notched tension, (d) single edge notched tension and(e) double edge notched tension

3.1 Material and experimental setup

The specimens considered in this study were all cut from cold-rolled AA6016 aluminum alloy plates, produced by Hydro Aluminium. The received plates had dimensions 625mm x 625 x 1.5 mm, and came in three different tempers: T4, T6, and T7. Solution heat treatment was done at 530°, followed by forced air cooling. The T4 temper was obtained by pre-baking at 80° and then naturally aging to stable condition, while the T6 and T7 temper were artificially aged at 185° for five hours and 205° for 24 hours, respectively. The chemical composition is given in Table 1. The yield strength of the tempers range from about 135 MPa for T4 to 245 MPa for T6, and the ultimate tensile strength ranges from roughly 200 MPa for T7 to just below 300 MPa for T6.

3.1.1 Uniaxial tension tests

Three parallels of the uniaxial tension test were performed on specimens cut 0° , 45° and 90° to the rolling direction. The gauge section of the uniaxial test specimen was 70 mm x 12.5 mm and geometry details are display in 3.1a) The tensile tests were conducted on an Instron 5985 universal series testing machine with initial strain rate of 5×10^{-4} s^{-1} . A 100 kN load cell attached to the actuator measured the force during the experiments, while a camera oriented perpendicularly to the specimens captured images synchronized with the force measurements at 1 Hz. All specimens were spray-painted with a speckle pattern to enable 2D digital image correlation (2D-DIC) to track displacements using a 50 mm virtual extensometer in the in-house software eCorr[42].

3.1.2 Notched tension tests

Notched tensile tests were conducted using two different notch specimen: NT3 and NT10, with a notch radius of 3.35 mm and 10 mm, respectively. The minimum width of the cross-section was 5 mm for both specimen. The geometries are given in Fig. 3.1b) and c) with dimensions expressed in millimeters. Triplicate tests were conducted in the rolled direction using an Instron 5566-series hydraulic universal testing machine where the force was measured by a 10 kN load cell attached to the actuator. Quasi-static loading conditions were obtained using a cross head velocity of 0.01 mm/s. Force measurement from the load cell and images from the camera were recorded at 4 Hz. Displacements were measured from the image series in eCorr, using two sets of virtual extensometers placed centric to the notch radius, one global and one local. The initial length of the global extensometers was 10 mm for the NT3 specimen and 13.5 for the NT10 specimen, while the local extensometer had an initial length of 2 mm for both specimen.

3.1.3 SENT

Quasi-static mode I tear tests were performed on single edge notched tension (SENT) specimens. Five SENT-specimens were cut from a plate of each temper by the use of wire erosion. A thin slit with a length of 11.13 mm and 0.4 mm width was pre-cut into one of the sides to provoke fracture. The specimens were cut so that the slit was oriented in three different directions with respect to the rolled-direction: three 0° , one 45° and one 90°. The dimensions of the test specimen is shown in Fig. 3.1d). The tests were conducted with an Instron 8800 series hydraulic universal test machine where the force was measured by a 25 kN load cell attached to the actuator. All tests were performed with a constant cross head velocity of 0.02 mm/s, to ensure quasi-static loading conditions. The specimens were pinned at the fastening and allowed to rotate about this point. A 3D printed washer was placed between the clamping plates and the specimen in order to minimize out of plane buckling. The clamping configuration is illustrated in Fig. 3.2. A Basler acA4112-20um camera orientated perpendicular to the specimens was used to monitor the tests. Images of the test were captured, starting with a frame rate of 4Hz, and reduced to 1 Hz towards the end of the tests to avoid excessive images. From the images, elongation of the slit opening was extracted from a virtual extensometer by use of DIC in eCorr. The surface of the aluminium was found to give good enough contrast to track the displacements, such that no speckle pattern was sprayed onto the specimens as this would make the crack development harder to detect.

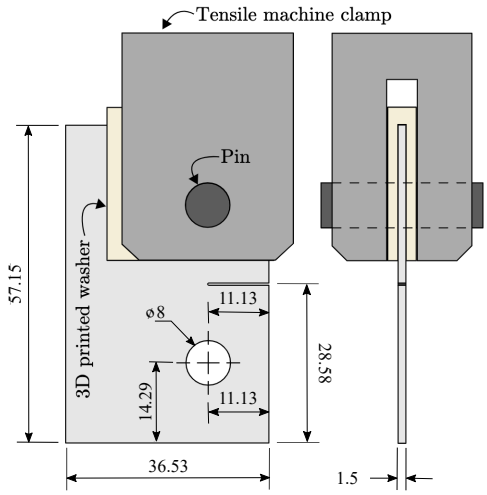

Figure 3.2: Illustrative drawing and clamping configuration of the SENT-test made by PhD. Candidate Vetle Espeseth.

3.1.4 DENT

Quadruplicate tests were conducted on double edge notched specimens. A full view of the specimen's geometry is given in Fig. 3.1e) with measurements in millimeters. Due to isotropic behavior found in the SENT and uniaxial experimental tests (see sec. 3.2.1 and 3.2.3) anisotropic behavior in the DENT-tests were not investigated. All specimens were cut from the cold-rolled aluminum plates in the same direction, with the slits oriented in the rolled direction of the plate equivalent to the SENT 0°-direction. The plate contained two 45 mm long slits with a 0.5 mm notch radius, establishing a 90 mm long ligament. The specimens were spray-painted on both surfaces prior to the test, one surface with a black and white speckle pattern facilitating DIC software and the other completely black to enhance thermal imaging.

The tests were conducted on an Instron 5985 universal testing machine where the plates were fastened to the testing machine using a custom made test-rig machined from cold-rolled AISI 1040 steel. Ten equidistant M10 bolts were used to confine the specimen to the loading plates to ensure a fixed connection, while the loading plates were connected to mounting plates using a loading pin and two connection blocks. The test-rig is illustrated in Fig. 3.3. During the experimental set-up, the custom made upper mounting plate was found to be incompatible with the test machine and was consequently replaced by an improvised version, which was observed to leave a slight gap between the upper loading and mounting plates. The tests were conducted using a crosshead velocity of 0.25 mm/min to mimic quasi-static loading conditions. A 100 kN load cell attached to the actuator measured the force during the experiments, while a camera facing the specimens speckle pattern surface captured images synchronized with the force measurements at 1 Hz. To further improve the DIC software to extract accurate data, a spotlight was also applied to the speckled area to ensure a uniform light condition. A FLIR infrared camera was also implemented and was facing the black painted surface of the specimen to attempt to capture heat generation during plastic deformation.

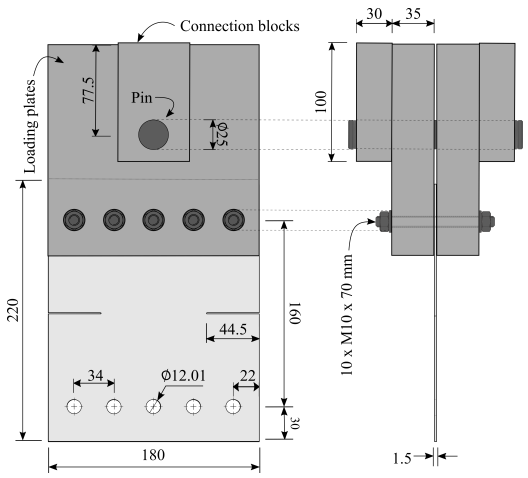

Figure 3.3: Illustrative drawing and clamping configuration of the DENT-test.

3.2 Experimental results

3.2.1 Uniaxial tensile test

From the experimental force data and post-processed displacement data from DIC, the engineering stresses and strains were calculated using Eq. (2.1) The engineering stress-strain curves of the triplicate tests in the rolled direction from are plotted in Fig. 3.4a) while the stress-strain curves from representative tests in each direction are plotted in Fig. 3.4b). Comparing the stress-strain curves between the different tempers, the fracture strain and strength is observed to vary. As expected, the T6 temper has the highest peak force, followed in turn by the T4 and T7 temper. The highest strains are observed for the T4 temper which also experiences the most work-hardening. As seen from Fig. 3.4b) the material is nearly isotropic with respect to flow stress, but slightly anisotropic with respect to failure strain.

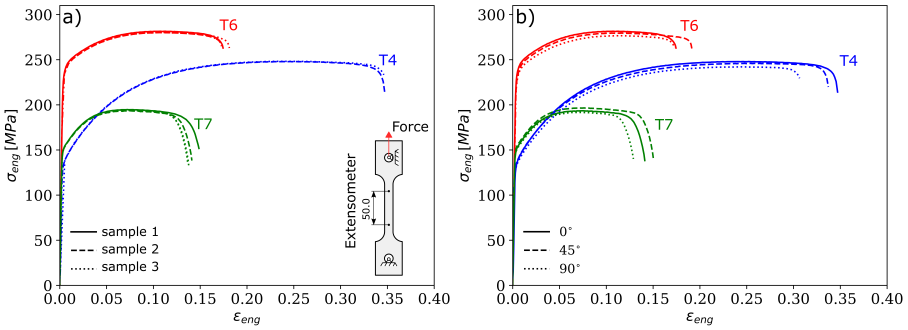

Figure 3.4: Engineering stress-strain curves from (a) samples in the rolled direction (b) representative tests in each direction.

3.2.2 Notched tensile test results

The experimental results from the NT10 and NT3 tests are shown in Figure 3.5. It is seen that the repeatability of the notch tension tests was excellent. The engineering strains were extracted from the displacements measured by the global virtual extensometer while the logarithmic strains were calculated from the displacements measured by the local virtual extensometer. The force levels between the two test geometries are similar, while the displacements are slightly larger for the largest notch radius. The local strain is also seen to be higher in the tests with the largest notch radius. This is attributed to the the smaller notch confining the gauge section more than the larger notch radius, resulting in a higher stress triaxiality and in turn earlier occurrence of necking. Comparing the different tempers it is seen that the T6 temper has the highest strength followed by the T4 and then T7 temper, while the largest strains are obtained for the T4 temper followed by the T7 then T6 temper.

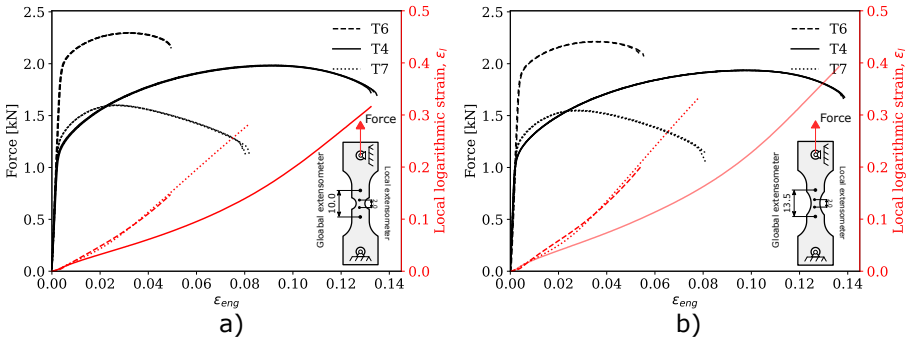

Figure 3.5: Extracted force-strain and local strain-strain curves from (a) NT3 tesnsion tests, and (b) NT10 tension tests.

3.2.3 SENT - test

The force – slit opening displacement (SOD) curves from the SENT-tests are shown in Fig. 3.6, where the slit opening displacement was measured from the outer corners of the slit. From the triplicate test results in the 0°-direction it is seen that repeatability of the test was excellent. Comparison of the test results in the three directions suggests that the material behavior is predominantly isotropic with only minuscule anisotropic effects, seen by a slightly higher peak force in the 45° and 90° orientation for all tempers. Between the tempers, the highest peak force was obtained for temper T6 with a peak force of approximately 3.8 9N followed by tempers T4 at 3.0-3.1 kN and T7 at 3.0 kN. The crack opening displacement at peak force differed between the three tempers, with the T6 temper reaching peak force at the lowest displacement at approximately 0.60 mm, followed by the T7 temper at 1.1 mm and T4 at 1.50 mm.

The difference in response leading up to the peak force is probably linked to the plasticity of the material. The larger proof stress seen for the T6 temper allows for larger elastic deformation in the process zone leading to a higher peak force. Once the critical stress is reached leading to fracture, crack propagation occurs more readily due to the lower ductility and work hardening, as seen by the steep drop in stress carrying capacity following the peak force. The difference between the T7 and T4 temper is likely due to the prolonged hardening of the T4 temper resulting in a

higher peak force. Moreover, the T4 temper is seen to display the largest displacements despite the T7 temper being the more ductile alloy. This is linked to the combination of adequate strength, work-hardening and ductility in temper T4, which seems to be more favorable than the high ductility and low work-hardening seen for temper T7.

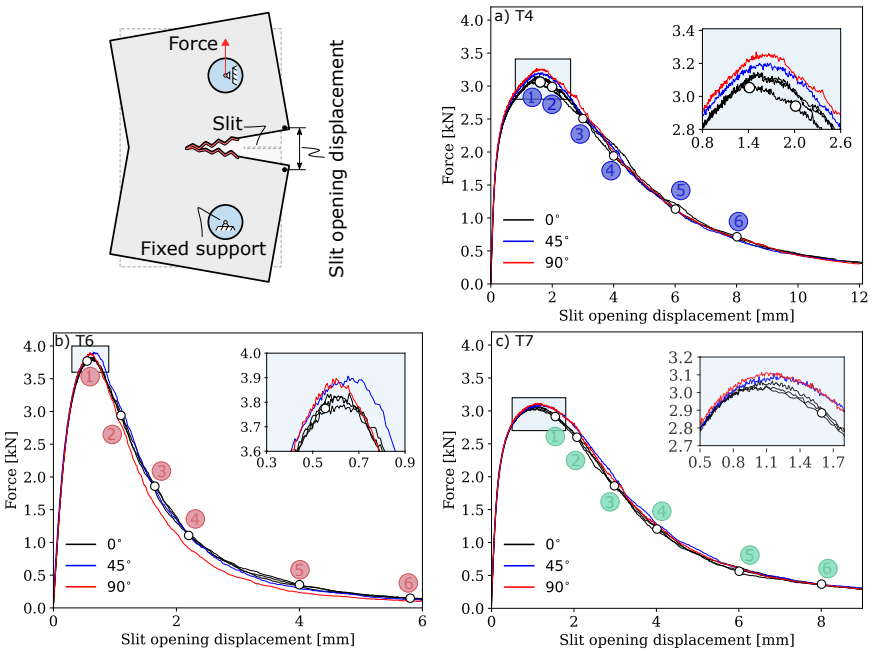

Figure 3.6: (Top left) Sketch of the SENT- test made by PhD. candidate Vetle Espeseth. Experimental results for (a) Temper T4, (b) temper T6 and (c) temper T7.

Figure 3.7 shows the image series from DIC corresponding to the SOD indicated on the force-SOD curves. The fracture mode are seen to differ between the tempers. For the T6 and T4 temper, the slant fracture mode can be seen. The slanted fracture mode occurs when a neck forms ahead of the crack tip where plastic deformation localizes in one of the 45° shear bands, due to some asymmetric imperfection, causing a slanted shear crack in the final stage of separation [43]. For the T4 temper, the alternating slant phenomenon is seen, where the slanted fracture is seen to irregularly alternate between the two possible shear-bands. The T7 temper fracture predominantly initiated and propagated in the tunneling-fracture mode until arrested, resulting in a cup-and-cup fracture surface. Minor slanting through a small segment of the thickness was also observed in the T7 tests. The slanted fracture is governed by shear-bands, while the cup-and-cup fracture mode is found to be governed by the interplay between void growth and the necking process. The findings of the tests are consistent with reports that cup-and-cup fracture mode is favored in materials where extensive void growth and necking occurs while the slant fracture mode is more favored in higher strength materials [43]. The different material properties between the tempers also produced different fracture surfaces, with smoother surfaces found on the higher strength T6 and T4 -tempers.

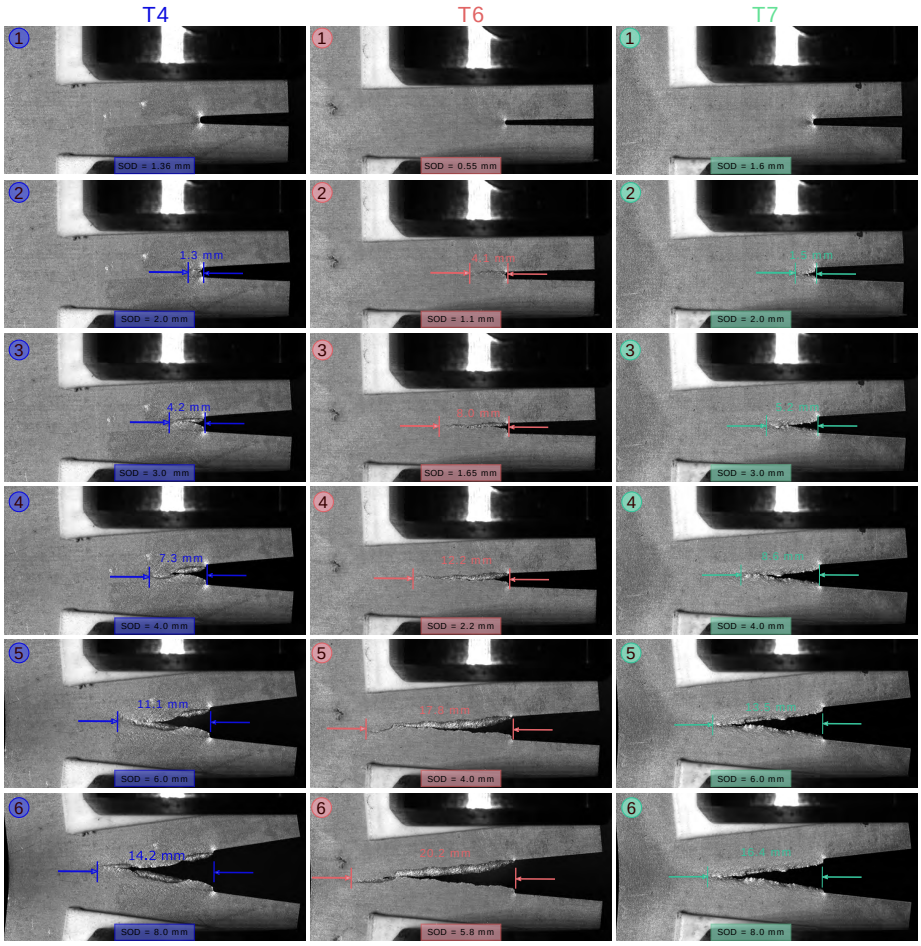

Figure 3.7: Image series from the SENT-experiment using the (left column) temper T4, (centre column) temper T6 and (right column) temper T7.

The surface crack displacements for each temper are plotted in Fig. 3.8. The data is plotted with 1 mm error bars as measurement precision was limited by the resolution of the images. The crack displacement at mid-plane is expected to be ahead of the measured surface crack as ductile crack propagation is expected to occur in a tunneling mode. The extent of tunneling is reduced by slant-fracture growth [44], such that the discrepancy between the crack front and the surface crack displacement is expected to be less for the T4 and T6 tempers.

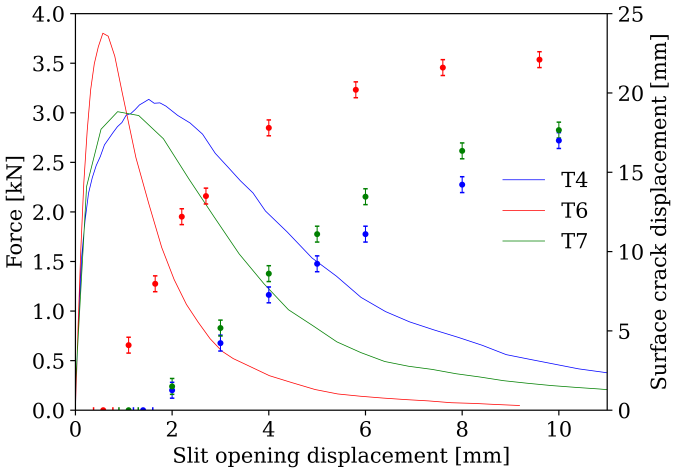

Figure 3.8: The measured surface crack displacement plotted against the slit opening displacement on the second y-axis with the force-SOD curves plotted in the background for referencing.

Some out-of-plane displacement was observed for the T4 specimen during testing, with the amount of displacement varying between tests. This impact on the force-displacement curve appeared negligible however, as the results from samples where out-of-plane occurred differed insignificantly to tests where out-of-plane displacement was almost unnoticeable.

3.2.4 DENT - test

The force – displacement curves from the quadruplicate DENT-tests are shown in Fig. 3.9, where the displacement was taken as the average vertical displacements over the outer corner of both slits: average slit opening displacement (SOD_{avg}). It is seen that repeatability of the DENT-tests was excellent. Overall, the trends are in accordance with the other mechanical tests presented, showing that temper T6 gives the highest peak force at approximately 35.0 kN, followed in turn by tempers T4 at 26.0 kN and T7 at 25.5 kN. Furthermore, the vertical displacement at peak force differed between the three tempers, with the T6 temper reaching peak force at the lowest displacement: at 0.58 mm, followed by the T7 temper at 0.97 mm and T4 at 1.80 mm.

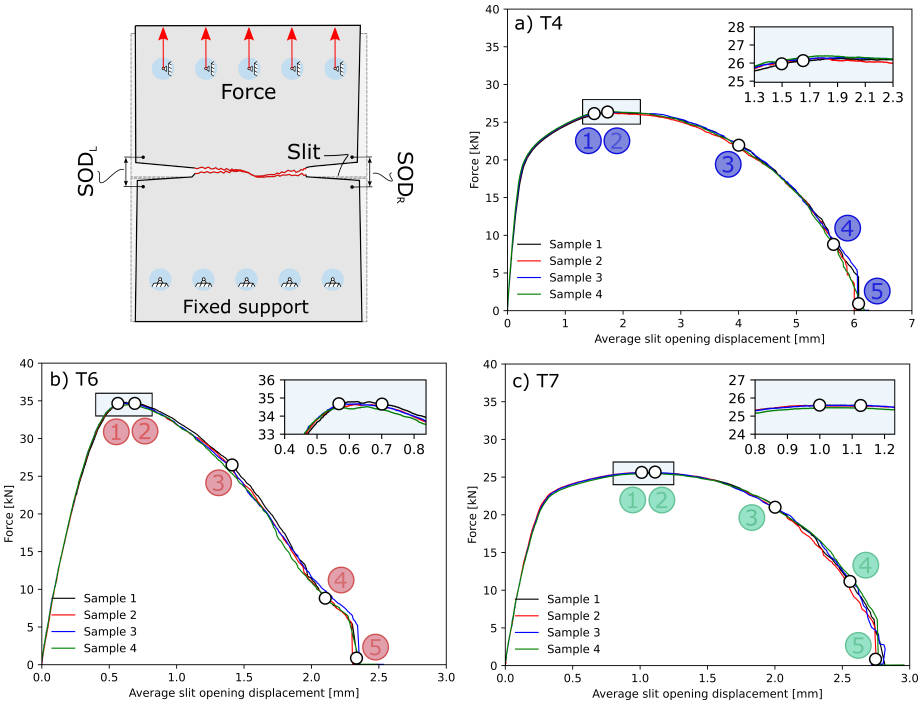

Figure 3.9: (Top left) Sketch of the DENT-specimen. Experimental results for (a) temper T4, (b) temper T6 and (c) temper T7.

It is seen from DIC that the first stage of the test, marked by the abrupt rise in forces, coincides with a transient phase of elastic deformation over the full width of the ligament between the slits. After the transient phase, strains localized, forming two contained plastic zones (PZ) at the vicinity of the slit openings where the material is strained past yielding. As the loading continues, a fracture process zone (FPZ) develops in the established plastic zone at the vicinity of the slits, where material damage accumulated, leading to fracture. The second stage of the test transpired after the initiation of fracture, where the forces dropped as the fracture process zone ahead of the crack tip drives the crack through the plastic zone. The DIC field map of accumulated strains, in the load direction, after the crack propagated approximately one third of the distance to the center is shown in Fig. 3.10. In Fig. 3.10a), the image of the specimen at the start of the experiment is used as a reference frame, whereas in Fig. 3.10b), the image corresponding to the onset of fracture is used as a reference frame, in order to illustrate the formation of the fracture process zone, which is obscured in the former. For Fig. 3.10b), the FPZ is assumed to be contained to the area shaded inn red while the PZ includes the area shaded light blue.

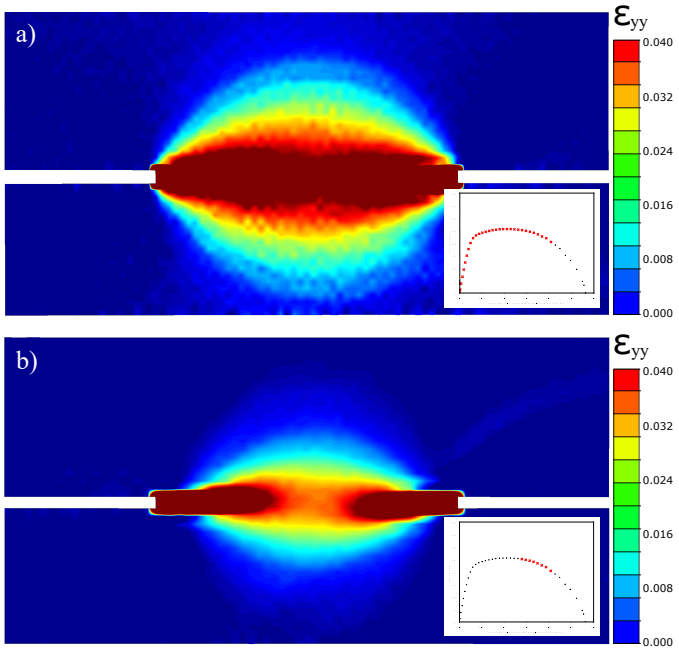

Figure 3.10: DIC strain-map of accumulated strains, ε_{yy}, of the T7 temper, using (a) the specimen at the start of the experiment as reference frame, and (b) using the image corresponding to the onset of fracture as reference frame.

Image series of the DENT-test at selected SOD_{avg} are shown in Fig. 3.11. It is seen that for all tempers, fracture initiated at the left notch somewhat earlier than the right notch, with the crack at the left notch propagating slightly upwards and the crack at the right notch propagating slightly downwards, resulting in an asymmetric crack path. Figure 3.12 shows the fractured DENT-specimens stacked on top of each-other, with the T7 tempers on top, T6 in the middle and T4 on the bottom. The fracture modes observed in the DENT tests were comparable to the fracture modes seen in the SENT-specimens, where fracture in temper T4 and T6 initiated in a flat tunneling mode before transitioning to slant fracture mode after only a few millimeters. The T7 initiated and propagated in a flat tunneling mode until complete fracture. For the T4 temper the alternating slant-fracture phenomenon was observed, where the direction of the slant regularly flips ninety degrees during crack propagation. Once the crack fronts approached the center of the plate, the remaining ligament was fully enclosed by the plastic zone, and experienced considerable necking before complete fracture occurred in a tunneling mode. Thus, by inspection of the fracture surface in the T4 and T6 temper an abrupt change in the fracture surface is seen where the fracture mode changes from slant fracture to flat fracture. The fracture surface resulting from the flat fracture was also observed to be rougher with with small craters, whereas the slant fracture resulted in a smoother fracture surface. This is consistent with the observation that the center of the neck experienced extensive necking compared to the region closer to crack initiation, as necking advances void growth such that fracture occurs due to void growth and coalescence rather than shear band-fracture. The crack path's deviation from the center plane was observed to be affected by the material properties, as it was more prominent for the T6 and T4 temper compared to the T7 temper. This coincides with the results obtained

from the modified arcan tests subjected to a load 45 degrees to the normal axis; the crack path for the ductile T7 temper followed the center plane even though the load was asymmetric, see sec.7 for more details.

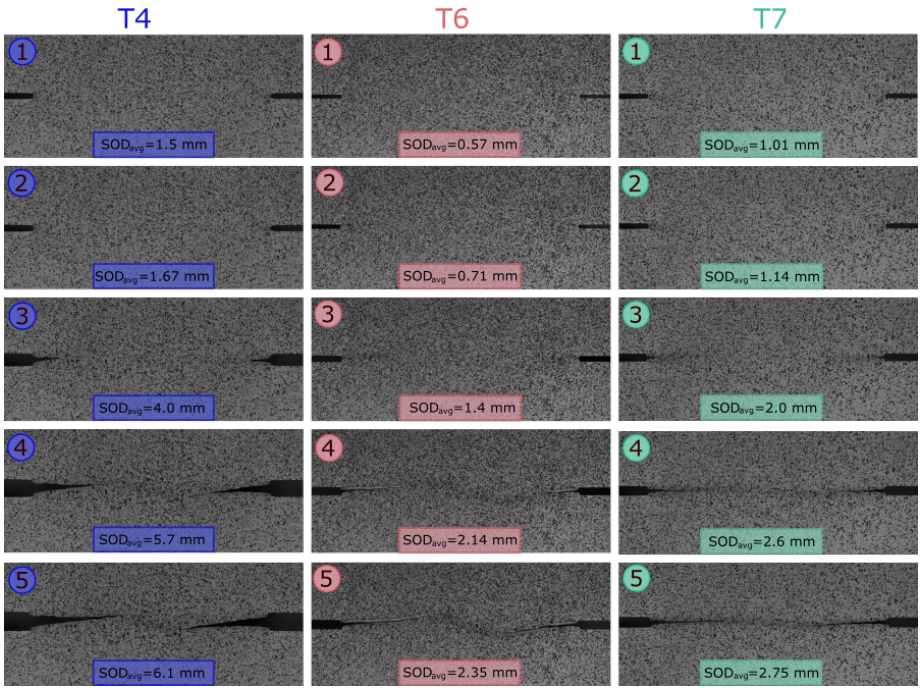

Figure 3.11: Image series from the DENT-experiment for the (left column) T4 temper, (centre column) T6 temper and the (right column) T7 temper.

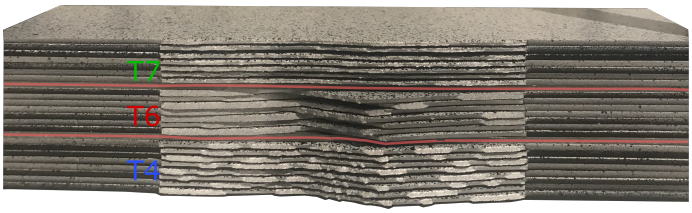

Figure 3.12: Fracture surfaces of the the DENT specimens.

The earlier occurrence of fracture at the left notch in addition to the unique crack path experienced by each sample suggested some disproportion in the test set-up, as crack initiation in an ideal test is expected to occur simultaneously at both notches and the crack propagation remain in its original plane. Geometrical variations can also be excluded as the crack path for every sample for each temper were close to identical.

DIC measurements showed that for each temper the plate experienced considerable horizontal displacement. To investigate the cause of the recurrent horizontal displacements, and obtain the

correct loading conditions of the experiment for subsequent simulations, the relationship between horizontal displacements, u, and vertical displacements, v, over the plates were determined by tracking both displacements simultaneously in DIC. The displacements of the upper and lower half of the plate were tracked at nine equidistant points as close to the frame boundary as possible. The relationship between the vertical and horizontal displacements in combination with the force level is plotted in Fig. 3.13b, where the displacements are taken as the average of the top half of the plate subtracted by the average of the bottom half in order to disregard rigid body motion which would not contribute to an abnormal stress-state.

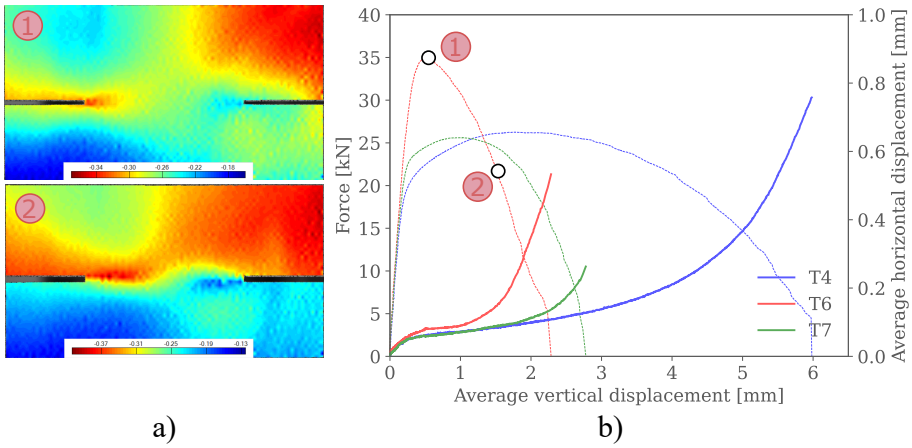

Figure 3.13: a) Field-maps from DIC of horizontal displacements at two selected instances. b) Horizontal displacements and force measure plotted against the vertical displacements.

From the figure it is evident that the horizontal displacement occurs in three stages: The first stage is marked by a steep rise in horizontal displacements as the plate undergoes elastic loading. During second stage, which transpires during the bulk of crack propagation, the horizontal displacements saturate. The third stage onsets when the crack fronts approach the center, causing a new spike in the horizontal displacements as the resistance in the plate approaches zero.

Figure 3.13a) shows field-maps from DIC of the horizontal displacements at two selected instances. From the field maps it is seen that the horizontal displacement varies with horizontal axis, with greater displacement on the left side compared to the right. This is expected as contraction of the plate will facilitate displacement on the right side and counteract displacement on the left side.

4 Modeling and simulations

4.1 Material model

The material behavior is described by a modified Gurson model which is the default porous plasticity model incorporated into Abaqus. The models main components are briefly repeated here. The yield function is written as:

$$\Phi = \left(\frac{\sigma_{eq}}{\sigma_y}\right)^2 + 2q_1 f^* \cosh\left(\frac{3\, q_2\, \sigma_H}{2\, \sigma_y}\right) - (1 + q_3 f^{*2}) \tag{4.1}$$

where f^* is defined in terms of Eq.(2.57). Damage evolution is defined by Eq. (2.55) where the parameters governing void nucleation (Eq.(2.56)) are specified by the user.

In Abaqus, failure is modelled when the current void volume fraction, f^* reaches the user specified parameter f_C . Total failure at an integration point occurs when $f^* \geq f_F$. An element is removed from the FE-model once all of its integration points have failed.

The hardening of the fully dense matrix is defined through the three term Voce hardening rule Eq.(2.26). And was implemented through a user-defined hardening subroutine (VUHARD).

Strain-rate sensitivity effects were looked into by including a multiplicative viscosity-hardening law, altering the altering the yield stress to:

$$\sigma_{eq} = (\sigma_0 + R(p))(1 + p^*)^c \tag{4.2}$$

where $\dot{p}^* = \frac{\dot{p}}{\dot{p_0}}$ being a reference strain, and the constant c governs the rate sensitivity of the material. The strain-rate effects were considered insignificant and thus the viscous stress was excluded from the material model. This decision was also vetted by extensive studies of strain-rate sensitivity of 6xxx alloys where the strain rate sensitivity is found to be practically negligible[30].

Cockroft Latham model For the CL-model the yield condition is reduced to the von Mises yield criterion, while the material hardening remains defined by the Voce hardening law. Material failure is governed by the Cockroft-Latham failure criterion , given by the equation:

$$w = \frac{1}{W_c} \int_0^p \max(\sigma_1,\, 0)\, dp \tag{4.3}$$

In Abaqus the Cockroft-Latham yield criterion is implemented as a user defined subroutine, where W_C is the only required input parameter needed to be calibrated.

4.2 Finite element modelling

All simulations in this study were performed using the explicit integration scheme of Abaqus (described in sec. 2.7) with velocity-controlled loading and $\alpha = 0.9$. Time scaling (see, sec.time-scaling was used to reduce computational cost, where velocity was ramped from zero to the prescribed value during the first ten percent of the step duration to prevent spurious stress waves. The specimens were modeled as homogeneous solid parts and meshed using 8-node brick elements with reduced integration and hourglass control, denoted C3D8R in Abaqus. Two characteristic element lengths were used for all specimens in their predicted crack-regions, 0.25 mm or 0.15 mm, giving three or five elements across the half-thickness. Fracture were modelled by element erosion, where elements are removed when fracture criteria in sec. 4.1 are met. Symmetry planes were utilized to lessen the

computational effort when possible, and the reduced model was verified against selected simulations of the full specimen. To ensure quasi static loading conditions and refute the possibility of any unwanted dynamic effects, an energy balance check (Eq. (2.59)) was performed to ensure that the kinetic and artificial energy were negligible. Meshed assemblies for all test specimen are displayed in Fig.4.1

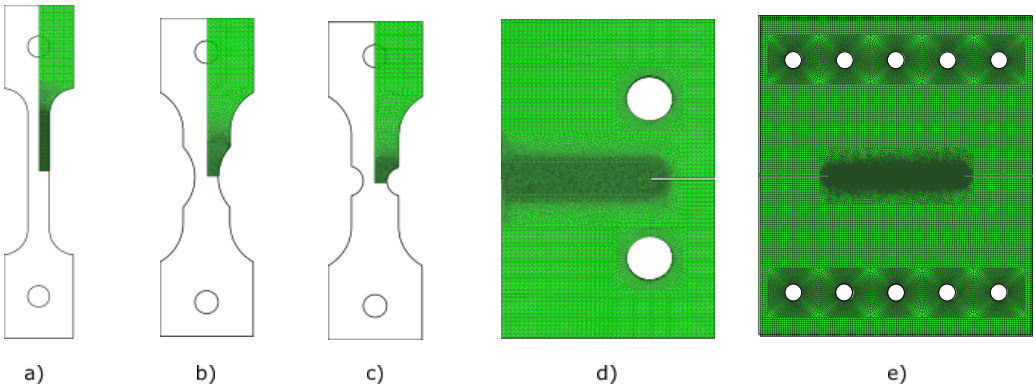

Figure 4.1: Finite element meshes of test specimens: a) UT200, b) NT10, c) NT335, d) SENT and e) DENT

4.2.1 Uniaxial and notched tension

Tension specimens were modelled using three symmetry planes, thus only one eight of the specimens were modelled. The gripped end was constrained to a reference point via an equation constraint, which was prescribed a 500mm/s velocity. The reaction forces at the reference point were extracted as load data, while nodes with corresponding placement to experimental extraction points were used to obtain strain data. An in-plane view of the meshed specimens are shown in Fig. 4.1a),b) and c).

4.2.2 SENT

The SENT-specimen was modeled using a through thickness symmetry plane. The two characteristic element dimensions, $h_e = 0.25$ and $h_e = 0.15$, in the crack zone resulted in slight variations in how the slit was modeled. Using the coarser mesh, $h_e = 0.25$ mm, the slit was modeled as a single element, whereas in the finer-mesh model, it was modelled using three elements across the slit height. Outside the crack zones, the mesh comprised of a structured mesh with element size equal to 0.75 mm. The pins used to apply the load and support in the experiment were modeled as rigid analytical parts. The upper pin was assigned a single translational degree of freedom to constrain movement to only allow vertical displacement, while the lower pin was kept fixed. Load and boundary conditions were transferred from the pins to the plate using a general contact condition with a hard frictionless interaction property, recognizing the pinned link between the specimen and support pins. Slit opening displacement was extracted from the two edge nodes directly above and below the slit, corresponding to the DIC measurements, while the force was extracted as the reaction force from the support pin. A brief mesh structure sensitivity study was also performed by implementing two different meshing techniques, structured and randomly generated sweep mesh, in the crack zone. For the irregular mesh, crack initiation was aided by giving the area in the immediate vicinity to the slit a structured mesh. The complete meshed specimen using $h_e = 0.15$ mm and an irregular swept mesh in the crack zone is shown in Fig. 4.1d), while the critical region of the different SENT-mesh configurations is shown in Fig. A.2.

4.2.3 DENT-numerical model

The DENT-specimen was modeled using a through thickness symmetry plane. The critical region between the slits was modelled using a fine irregular mesh while the first elements in the immediate vicinity to the slit were structured to aid crack propagation (as for the SENT). The assembly used for the DENT specimen is shown in Fig. 4.1e) while the critical regions of the mesh is displayed in Fig. A.3. Outside the crack region the plate was modelled using a structured mesh with a characteristic element size equal to 1 mm. An MPC constraint was used to connect the specimens pinholes to reference points representing the loading and support pins. The slit opening displacement was extracted by measuring the displacement between nodes at the slit opening, corresponding to the DIC measurements, and the reaction force was extracted from the reference nodes.

5 Calibration

The GTN-model can be calibrated via two methods: 1) The metallograhpic method, which treats the model as a micromechanical model using quantitative photography to determine the parameters by analyzing fracture surface metallography and 2) the method applied in this study, the numerical method; where the model is treated more like a phenomenological model in order to capture the

empirical relationship between the material response to an applied loading state. The CL-fracture model is phenomenological in nature and is exemplary in being simple to calibrate, requiring only a single parameter to be calibrated. In this section the calibration process for both the GTN-model and the CL-model will be presented. Experimental data obtained from smooth test specimens were used to determine the yield stress, σ_0 , and hardening parameters $(\theta_1, Q_1, \theta_2, Q_2, \theta_3, Q_3)$. The damage model parameters to both fracture models were calibrated using the notched NT3-specimen.

5.1 Calibration of hardening parameters

The first calibration step was to determine the hardening parameters using the test data from the smooth test specimens. A preliminary set of hardening parameters were determined through curve fitting the extended voce hardening rule Eq. (2.26) with the experimental strain data. The hardening parameters are then optimized using a reversed engineering approach, where a series of FE-simulations are preformed for a range of hardening parameters until an optimized set is found which minimizes the offset of the simulated stress-strain curve and the experimental stress-strain curve. In this study an optimized set of hardening parameters had been calculated beforehand by PhD candidate Vetle Espeseth. The parameters for each temper are tabulated in Table 2. The stress-strain curves from the simulation are plotted as solid lines together with the experiment as dashes in Fig. 5.1. It is seen that the hardening parameters give excellent agreement with the experimental data, but with some lack of softening at the end, especially for the T7.

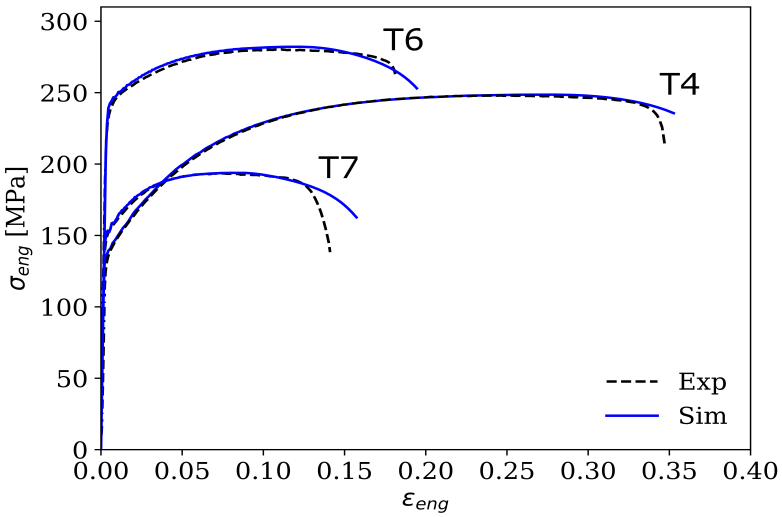

Figure 5.1: Stress-strain curves from experiments and simulations of the Uniaxial tensile tests.

5.2 Calibration of the GTN-model

After the hardening parameters were determined, the parameters in the GTN-model were calibrated using test data from the notched NT3-specimen. In most studies the GTN-model is calibrated by considering some parameters as fixed and others as fitting parameters to simulate the experimentally

Table 2: Table of calibrated parameters from [1]

Temper	σ_y[MPa]	θ_1	Q_1[MPa]	θ_2	Q_2[MPa]	θ_3	Q_3[MPa]
T4	123.3	12410	10.640	1941	118.30	279.4	24550
T6	226.9	11430	15.230	1272	51.17	235.0	5229
T7	145.3	13620	2.464	2385	52.95	138.6	6626

observed force-displacement curve of a material test. The void interaction parameters, q_1, q_2, q_3, are typically taken as fixed values that have been shown to give good agreement with unit cell simulations[10, 45]. Calibration of the parameters governing the material damage, $f_0, f_N, \varepsilon_N, s_N$ is typically done without considering failure, such that f_c and f_f are initially omitted in the simulations [46]. In calibrating the damage parameters, three types of calibrations have been identified: 1) $f_0 \geq 0$ and $f_N = \varepsilon_N = 0$ such that void nucleation is disregarded entirely and all softening is due to growth of pre-existing voids[17, 45, 47]. 2) $f_0 = 0$, $f_N \geq 0$ and $\varepsilon_N \geq 0$, such that no voids are assumed present in the material initially and all softening occurs from nucleation [11]. 3) In the third type both initial and nucleated voids are considered such that $f_0 \geq 0$, $f_N \geq 0$ and $\varepsilon_N \geq 0$[10]. Once the damage parameters are calibrated, the parameters governing failure, f_c and f_f are incorporated in the simulations and fitted to match the experimental force-displacement curves.

In this study the void interaction parameters, q_1, q_2, q_3, were taken as 1.5, 1, and 2.25 which are values commonly found in literature [10]. Damage due to the growth of initial voids and nucleated voids is herein considered such that, f_0, f_N, ε_N s_N along with the ductile fracture parameters f_c and f_f were chosen for calibration. These parameters were calibrated using parametric studies to identify the effect of each parameter on the force-displacement curve. The parameters of the GTN-model are mesh sensitive, so the validity of the calibrated model is restricted by the characteristic element length assigned to the critical region in the calibration simulations. The mesh sensitivity emanates from the dependency on the plastic strain measure on the evolution of f, as the average plastic strain measure during material failure increases with decreasing element size. A consequence of this mesh dependency is that multiple models need to be calibrated to assess the model performance for various discretizations. In this study, GTN- models were calibrated to two characteristic element lengths: $h_e = 0.25$mm and $h_e = 0.15$mm, giving six and ten elements across the specimens thickness, respectively. The GTN-parameters were first calibrated to the mesh using characteristic element length, $h_e = 0.25$mm, following the calibration process described in the following sections. Then, using the h_e=0.25mm-calibrated parameters as an initial estimate, a second set of parameters was calibrated to the mesh using characteristic element length, h_e=0.15m.

5.2.1 Parametric study

Acquisition of an initial estimate for the initial void volume fraction and the nucleation parameters was aided by conducting a parametric study, where the effect of each parameter on the simulated force-strain curves was examined by sequentially varying one parameter while keeping all other parameters fixed. The range of values for each parameter were chosen based on values commonly reported in literature for typical metals (see. Table 3). The force-strain data from the NT3 tension test simulations were extracted from the analysis and plotted against the experimental force-strain data. The development of the void volume fraction of the most exposed element was also extracted to investigate. The resulting plots for each temper are shown in Fig. 5.2-5.4.

Table 3: Gurson damage parameters according to literature.

q_1	q_2	q_3	f_0	f_N	ε_N	s_N
1.5	1	$q_1^2 = 2.25$	0.0 - 0.004	0.00 - 0.06	0.1 - 0.3	0.05 - 0.1

Effect of f_0: A first series of simulations were conducted by only considering void growth, and disregarding the effect of void nucleation. The initial void volume fraction, f_0 was the only additional parameter to be added to the material model. Simulations were done with values for f_0 increasing incrementally from $f_0 = 0$ to $f_0 = 0.004$. In Fig. 5.2-5.4, it is seen that the difference in the resulting force-strain curves is minimal for the different f_0 configurations. From the VVF - strain curve it is seen that the void volume fraction at the experimental failure strain depends on the initial void volume fraction. This indicates that the choice of f_0 in the calibrated model will have an impact the choice of the critical void volume fraction, f_c.

Effect of f_N Sequential simulations were conducted where the void volume fraction from nucleation, f_N was varied from 0.02 to 0.06, whilst f_0, ε_N , s_N were kept fixed at 0.001, 0.2, and 0.1 respectively. The f_N parameter governs the amount of voids nucleated by plastic strain, where the onset of nucleation is dictated by the ε_N parameter. This is illustrated in Fig. 5.2-5.4 where the force-strain curve is seen to be completely insensitive to variations of f_N until the lower limit of nucleation is met, while the results during progressive failure are more diverse. Naturally it is seen that higher values for f_N result in a increased softening of the material.

Effect of ε_N The effect of the mean strain for nucleation, ε_N, was investigated and the parameter varied from 0.1 to 0.3, while f_0, f_N , s_N were set to 0.001, 0.04, and 0.1. As mentioned earlier, the ε_N parameter dictates the onset of void nucleation in terms of the plastic strain measure. This is illustrated in the figures 5.2-5.4 where lower values of ε_N result in an earlier occurrence of a high void volume fraction, advancing the onset of strain softening and resulting in an earlier decline in the force-strain curve.

Effect of s_N: The standard deviation for nucleation i.e the range for which nucleation takes place was varied from $s_N = 0.001$ to $s_{N=0.1}$, and f_0, f_N, ε_N were fixed at 0.001, 0.04, and 0.02 respectively. In figures 5.2-5.4 it is seen that the range of nucleation has a negligible influence on the hardening of the material. The influence of the s_N parameter is governed by the stress state at nucleation.

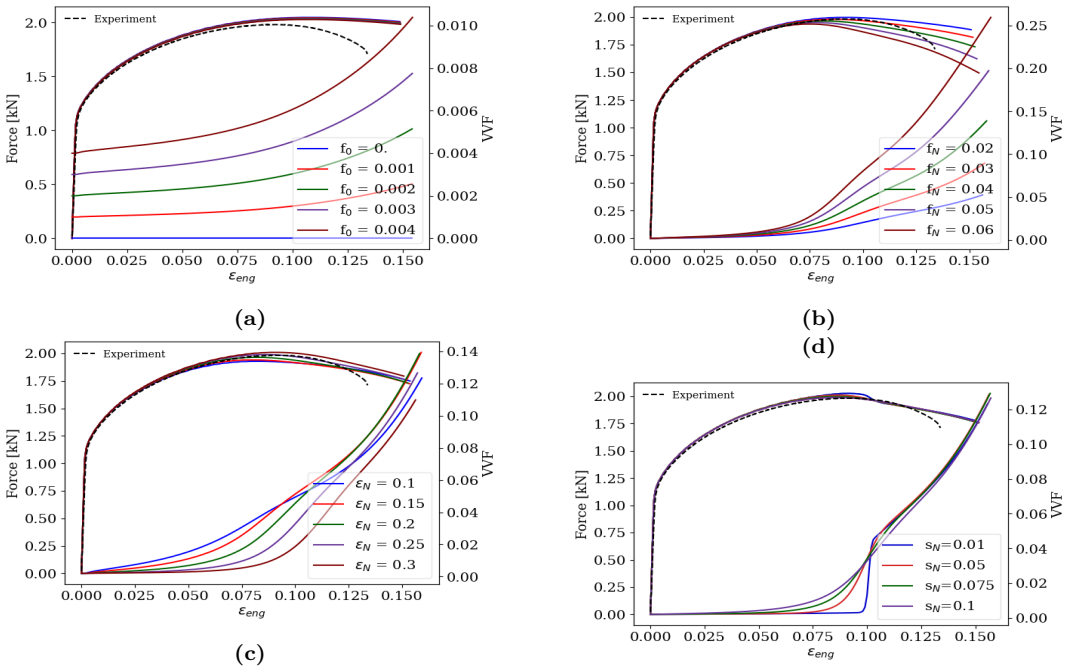

Figure 5.2: Force-strain curves and VVF-strain curves from the parameter study of a) f_0 , b) f_N , c) ε_N and d) s_N , for the T4 temper

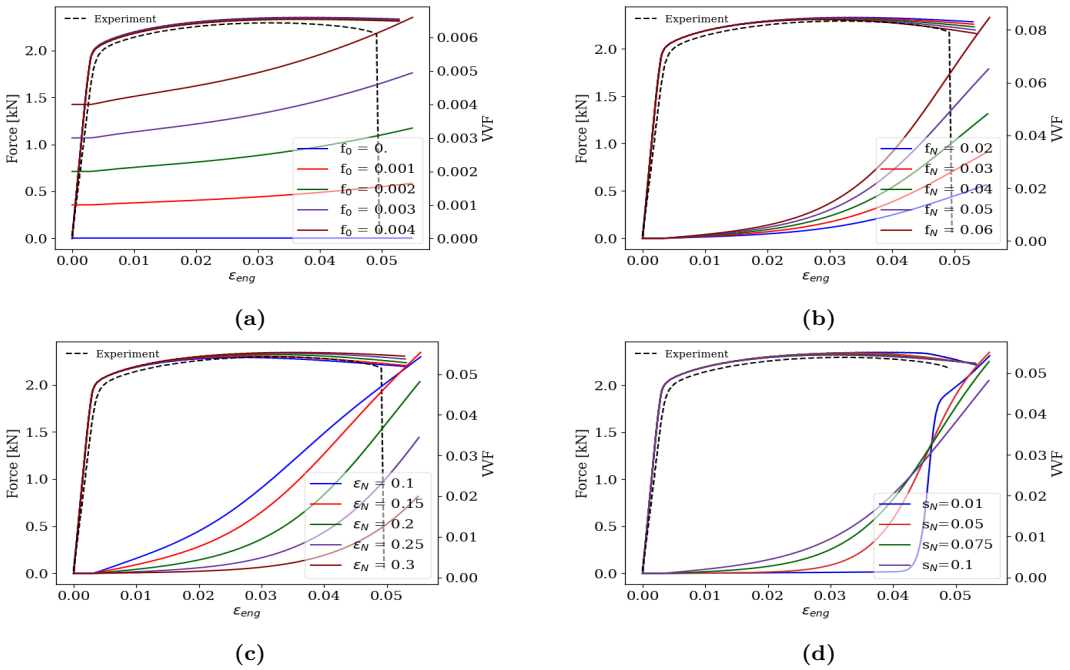

Figure 5.3: Force-strain curves and VVF-strain curves from the parameter study of a) f_0 , b) f_N , c) ε_N and d) s_N , for the T6 temper

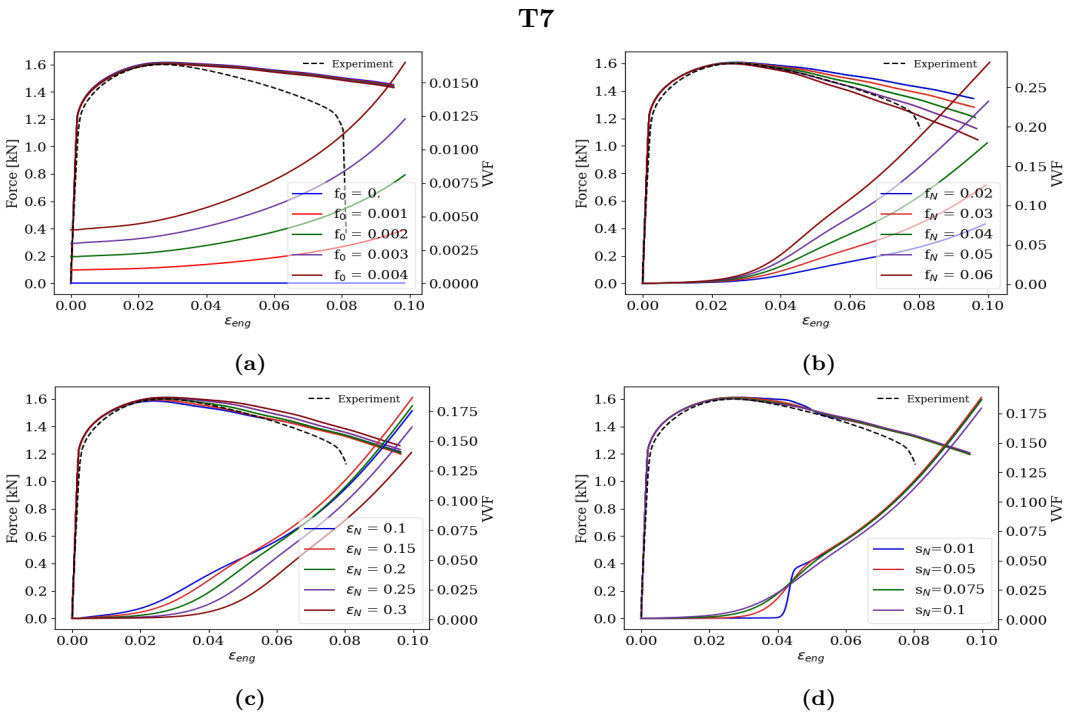

Figure 5.4: Force-strain curves and VVF-strain curves from the parameter study of a) f_0 , b) f_N , c) ε_N and d) s_N , for the T7 temper.

5.2.2 Calibration of f_0

The first parameter to be determined was the initial void volume fraction, f_0. From the parametric study it was seen that the material response varied little within the range of values tested for f_0. Higher values for f_0 did however result in a slightly softer material behavior at the start of the curve, and reduced the curve off-set for the T4 and T6-temper. The f_0 parameter was taken as 0.003 for the T4 and T6 temper, and 0.002 for the T7 temper. It should be noted that f_0 is herein used as a calibration parameter and does not represent the actual f_0 present in the material.

5.2.3 Calibration of ε_N ,f_N and s_N

The s_N parameter governs the equivalent plastic strain -range for void nucleation. In the parametric study the parameter was observed to have a limited impact on the material response, and was therefore kept fixed at 0.1 to simplify the calibration process. For a given s_N, ε_N and f_N govern the plastic strain level at which the damage from nucleation initiates and the amount of damage, respectively. In past studies, the physical significance of ε_N is disregarded, and the parameter is instead used as a fitting parameter. In such cases ε_N can be assumed in a suitable range from 0.1 to 0.3 [48], and f_N can then be calibrated to get the desired force-strain behavior. Past studies have highlighted a problem of non-uniqueness when it comes to calibrating these parameters, i.e., that the choice of ε_N and f_N is non-unique, and multiple choices exist that can simulate the desired material behavior. Kiran and Khandelwal [11]calibrated the constitutive parameters to ASTM

A992 steels; it was shown that accurate predictions were obtained for a range of ε_N, and that the corresponding optimized f_N parameter increased with increases in ε_N. This result identifies two limiting cases for simulating the damage evolution due to voids: early nucleation of fewer voids (ε_N low and f_N low) or late nucleation of a larger number of voids (ε_N high and f_N high). In this study the range of ε_N capable of accurately replicating the experimental data varied between the tempers. For the T6 temper a similar trend to that found by Kiran and Khandelwal [11] was encountered. The experimental results were sufficiently replicated by simulating both early and late nucleation. This is demonstrated in Fig. A.4 where the combinations of $\varepsilon_N = 0.1$, $f_N = 0.038$ and $\varepsilon_N = 0.25$, $f_N = 0.077$ are seen to predict nearly identical behavior. However, in the case of the T4 and T7 temper, the combination was more "unique" and the range of ε_N values which resulted in accurate predictions of the flow stress were limited. A similar approach to that in [11] was applied to determine an appropriate value for ε_N, and thereafter acquire a corresponding f_N through a reversed engineering approach. The ε_N parameter was taken to be comparable to the equivalent plastic strain measure of the most exposed element at the point where the force-strain results of the GTN-model, with nucleation omitted, diverged from the experimental data. In this sense the value ε_N is chosen on the basis of its physical significance; i.e., it represents the onset of material damage from nucleation. This approach is illustrated for the T4 temper in Fig. 5.5 (see appendix Fig. A.5 for all tempers). For temper T4, simulation results with nucleation omitted are seen to diverge at $\varepsilon^p_{eq} = 0.2$, which is interpreted as the point of damage initiation from nucleation. The point where the GTN-model diverges is shown to roughly coincide with the peak force, where the effect of strain hardening is surpassed by the reduction in cross-sectional area, i.e., necking, at which point void growth and nucleation occurs more readily due to the increased stress triaxiality in the center of the neck. For a standard deviation for nucleating voids, $s_N = 0.1$, ε_N can then be taken as 0.3. The acquired parameters by applying this approach for all tempers are tabulated in Table 4.

Table 4: Fitted damage parameters

Temper	f_0	f_N	ε_N	s_N
T4	0.003	0.055	0.30	0.1
T6	0.003	0.054	0.20	0.1
T7	0.002	0.052	0.20	0.1

5.2.4 Calibration of f_c and f_F

The fracture parameters, f_c and f_f govern the accelerated void volume fraction growth and final failure of the material (see Eq.(2.57) in sec.2.5.1. Void growth is accelerated when the void volume fraction at a Gauss point exceeds the value of f_c, and the magnitude of the accelerated void growth is dependent on the f_f parameter. It should be noted that the fracture parameters strongly depend on the initial void volume fraction and should not be considered a material property. For both the T4 and T6 temper, the experimentally observed "sharp knee" in the force-strain curves indicated that fracture occurred in an abrupt manner after reaching a critical point. The final failure could adequately be modeled solely using the f_c parameter. The f_c parameter was then determined as the simulated void volume fraction at the experiment's failure point, as illustrated in Fig. 5.5. The more ductile T7-temper was observed to display a "round knee" and the f_F parameter was included to adequately capture the additional macroscopic strain that occurred at the final stage of rapid

void growth and coalescence. To calibrate the f_c and f_f parameters simultaneously, the values were initially set equal to the void volume fraction at the start of the "knee" and at the fracture point, respectively, and then adjusted until a best fit was obtained with respect to the experimental data. Final GTN constitutive parameters calibrated to the NT3 specimen for h_e=0.25mm,are summarized in Table 5, while simulated and experimental force-strain curves are plotted in Fig. 5.6 along with the local logarithmic strain as function of the engineering strain. As seen in Fig. 5.6 the GTN-model was able to describe the force-strain curves for the NT3-specimen with excellent accuracy once calibrated. Good accuracy is also obtained with respect to the local logarithmic strains, where the predictions only slightly exceed the experimental results.

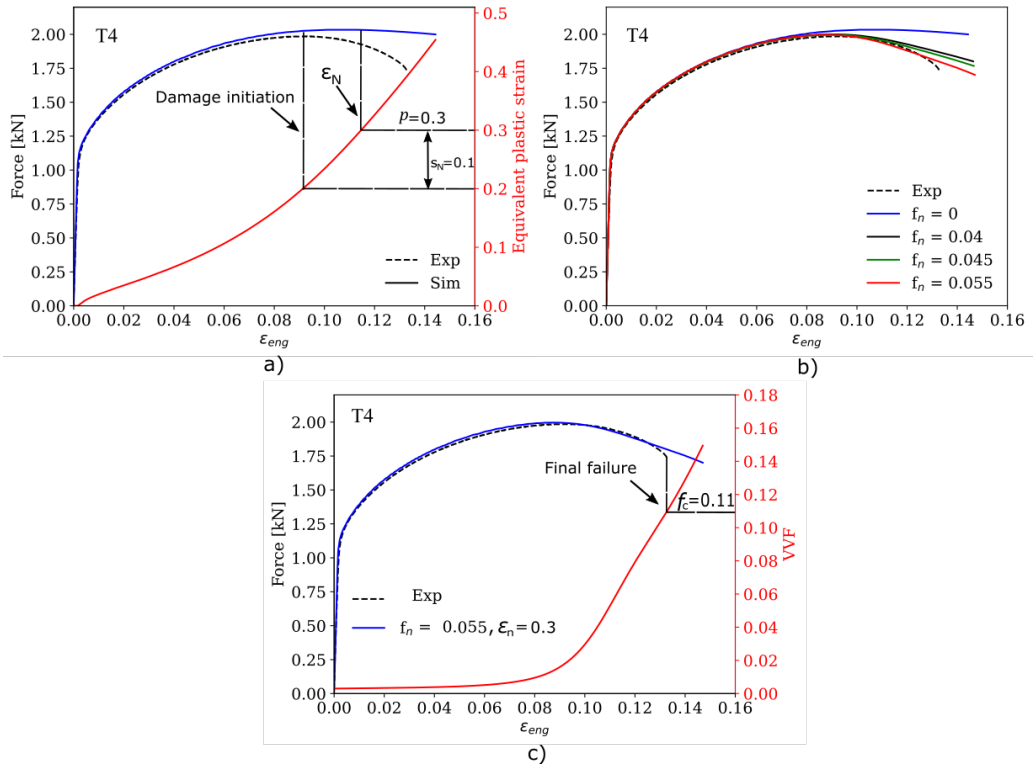

Figure 5.5: Illustration of calibration process for the T4 temper. a) Extraction of ε_N at the onset of deviation between experimental force-strain curves and the corresponding FE analysis results of the GTN-model with nucleation omitted. b) f_N optimization steps. c) Extraction of the fracture parameters, f_c from the simulated VVF corresponding to the experimental fracture strain.

Table 5: Final GTN constitutive parameters calibrated to the NT3 specimen for h_e=0.25,

Temper	f_0	f_N	ε_N	s_N	f_c	f_F
T4	0.003	0.055	0.30	0.1	0.110	0.110
T6	0.003	0.054	0.20	0.1	0.058	0.058
T7	0.002	0.052	0.20	0.1	0.145	0.200

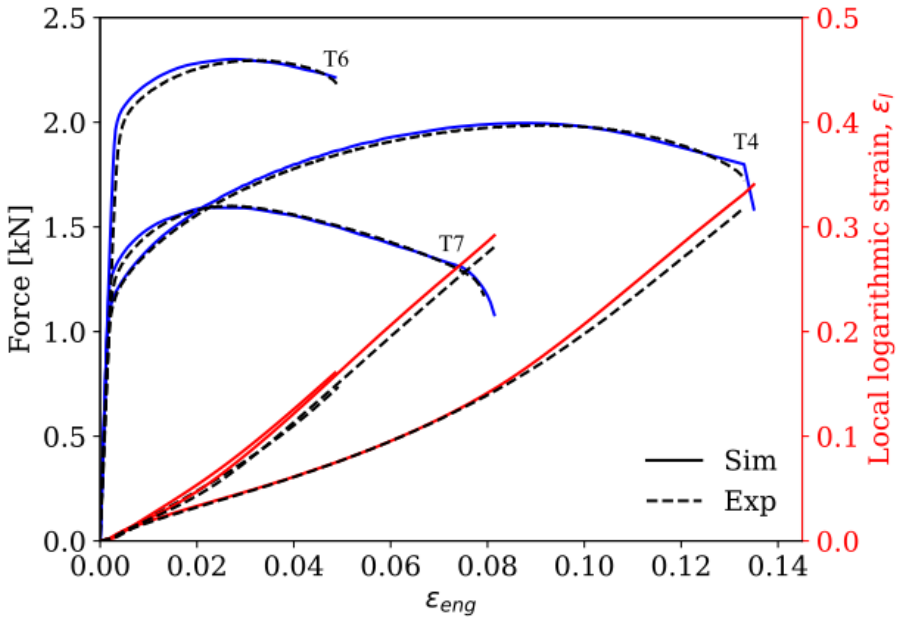

Figure 5.6: Simulation and experimental force-strain curves from the NT3-tensile test, along with strain-local-logarithmic-strain curves plotted along the second y-axis.

5.2.5 Calibration to the 0.15mm mesh

To calibrate the GTN-model to a characteristic element length of 0.15 mm, the NT3-test was simulated with the 0.15mm mesh in the critical region using the GTN-parameters calibrated to the 0.25mm mesh as an initial estimate. The simulated results using the initial estimate and the revised model is shown in Fig. A.6. It is seen that the fracture parameters calibrated to the 0.25 mm mesh predict an early occurrence of fracture when the mesh is refined. This is because the average strain measure is increased for the finer mesh and in turn the development of the VVF is accelerated such that the critical limit is reached at an earlier point. Other than the earlier occurrence of fracture, the numerical results are in excellent agreement with the experimental results. This suggests that the fracture parameters, f_f and f_c, are the most sensitive to mesh size, while the other parameters are rather insensitive. For the T4 and T6 temper only the f_c parameter needed to be increased to improve agreement with the experimental data, while for the T7 temper the void volume fraction for

nucleation was reduced in addition to increasing the fracture parameters. Final GTN constitutive parameters calibrated to the refined mesh are summarized in Table 6.

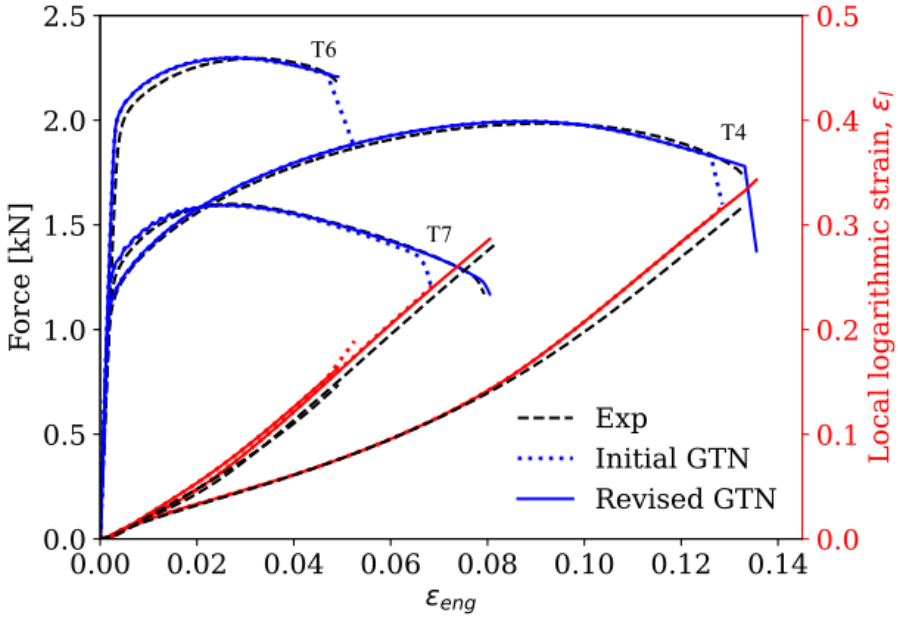

Figure 5.7: Force-strain curves and logarithmic strains from experiments and simulations of the NT3 - tensile tests with a 0.15mm mesh in the critical region.

Table 6: Final GTN constitutive parameters calibrated to the NT3 specimen using a 0.15mm mesh.

Temper	f_0	f_N	ε_N	s_N	f_c	f_F
T4	0.003	0.055	0.30	0.1	0.135	0.135
T6	0.003	0.054	0.2	0.1	0.062	0.062
T7	0.002	0.048	0.20	0.1	0.23	0.28

5.3 Calibration of the Cockroft-Latham fracture criterion

The Cockroft-Latham (CL) criterion introduced in sec. 2.4.5, requires only one damage parameter (W_C) to be calibrated.

$$W_c = \int_0^{p_f} max(\sigma_1, 0) dp \tag{5.1}$$

The CL-criterion is an uncoupled damage criterion, which means that the material does not experience softening as damage accumulates. The stress-strain relationship remains unaffected until the element reaches the damage threshold equal to the calibrated W_c. Since the purpose of introducing the

CL-criterion in this study was to compare its results to GTN-model, it was also calibrated to the NT3 specimen. In order to calibrate the damage parameter, an artificially high W_c was introduced in the material model and the damage evolution i.e., the major principal stress integrated over the equivalent plastic strain, was extracted from the numerical model's critical (central) element. In Figure 5.8 the accumulated damage in the T7 temper is plotted against the engineering strains along with the force-strain curves. As seen from the figure, W_c is set equal to the accumulated damage up to the equivalent plastic strain reaches the experimentally observed failure strain. The same method was used for the T4 and T6 temper, and the figure presenting their calibration procedure can be found in the appendix. Similar to GTN, the damage parameter is mesh size-dependent, and so two sets were calibrated with a characteristic element length of 0.25 and 0.15 mm, respectively. The results from the CL-calibration are summarized in Table 7. The simulated force-strain curves and local logarithmic strain results using the CL-model calibrated to the 0.25mm mesh are shown in Fig. 5.9a) along with the experimental results. It is seen that the simulated results are in good agreement up to peak force, after which the model is unable to capture the material softening and predicts slightly lower logarithmic strains. The T6 temper results are somewhat better as the T6 temper experiences less softening before fracture. The results using the 0.15mm - mesh with the CL-model calibrated to both the 0.25mm mesh and the 0.15mm mesh is shown in Fig. 5.9b). The CL-model calibrated to the 0.25mm mesh predicts a slightly earlier fracture when the mesh is refined. However, the deviation is considerably less than that observed in the GTN-model, suggesting greater mesh sensitivity in the latter.

Material cards for the GTN-model and CL-model for $h_e = 0.25$ are presented in the appendix

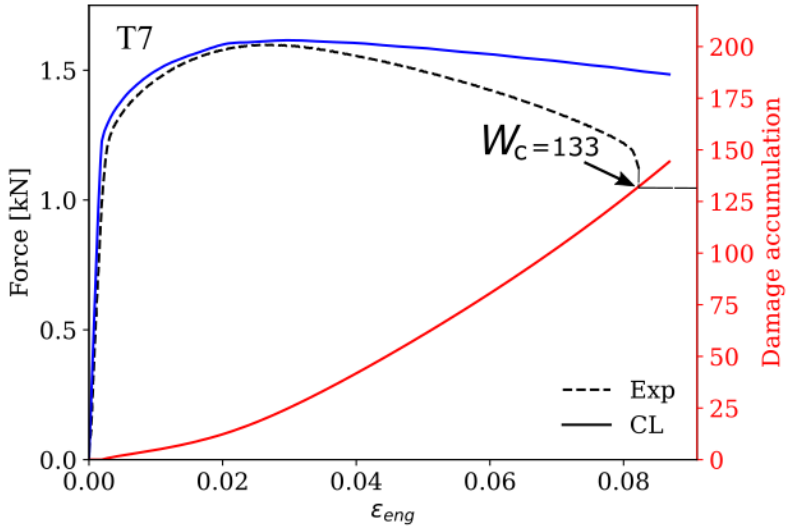

Figure 5.8: Acquisition of the damage parameter, W_c for the T7 temper, from the accumulated damage up to the experimentally observed fracture strain from the T7

Table 7: CL, damage parameter calibration

Temper	$W_c\left(\frac{Nmm}{mm^3}\right), h_e = 0.25\text{mm}$	$W_c\left(\frac{N\,mm}{mm^3}\right), h_e = 0.15\text{mm}$
T4	127	131
T6	78	80
T7	133	140

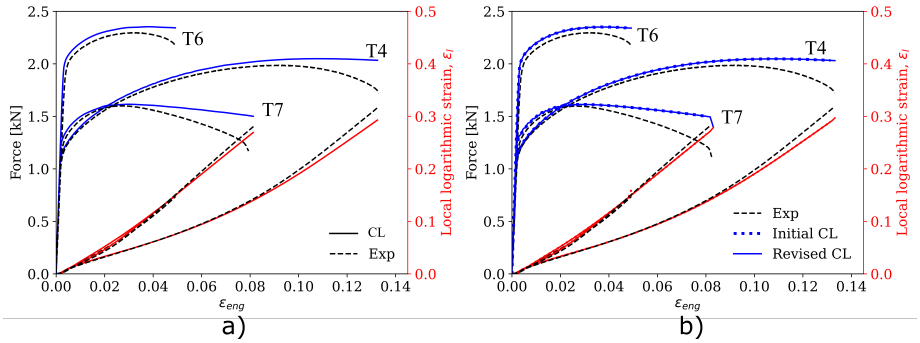

Figure 5.9: Experimental NT3 force-displacement and logarithmic strain-displacement curves and corresponding numerical results using the a) the CL-0.25mm calibration applied to the 0.25mm model b) the CL-0.25mm(initial) and CL-0.15mm (revised) -calibration applied to the 0.15mm model.

6 Numerical results and discussion

This section presents the numerical results obtained from uniaxial tension tests, single edge notched tension (SENT) and double edge notched tension (DENT) simulations using two characteristic element dimensions, $h_e = 0.25$ and $h_e = 0.15$. The ability to capture experimental force-displacement data, crack initiation and crack propagation for GTN and CL-models are examined and compared. Stress triaxiality and lode from elements along the crack path are also presented. There was little difference in computational effort between the two fracture models, as central processing unit (CPU) time for GTN was only around $1.1\times$ the CPU time for CL.

6.1 Material tests

The numerical results from the tensile test simulations using the uniaxial tension (UT200), notched NT3 and NT10 specimens are shown in Fig. 6.1, Fig. 6.2, and Fig. 6.3, respectively. The experimental results are presented as dashes, while the solid and dotted lines represent the simulated results using the GTN and CL-model. Since the GTN-model was calibrated to the experimental-NT3 data, the numerical results show an excellent agreement with the NT3-tests.

The least accurate results were obtained for the UT200-simulations, where both GTN and CL consistently underestimate the fracture strain. The considerable deviation regarding the fracture strain of the GTN-model was investigated by incorporating a minor strain rate sensitivity such that the equivalent stress was defined by Eq.(4.2). The UT200 finite element model was also adjusted by replacing time-scaling with mass scaling to accommodate the installed strain rate sensitivity, see sec. 2.7. The T7 engineering stress-strain curves and equivalent plastic strains as a function of the engineering strains are presented in Fig. 6.1b for different values of c. The onset of fracture in the specimen occurs shortly after necking. The material softening in the Gurson material accelerates stress-localization, seen by the steep rise in the equivalent plastic strain-strain curve. Adding a small strain rate sensitivity significantly delays the occurrence of necking, and an accurate fracture strain is acquired for a strain rate sensitivity with $c = 0.003$. The dramatic impact to the engineering fracture strain emanating from the minor strain rate sensitivity, despite loading being quasi-static, suggests that the discrepancy in the uniaxial tensile test could be attributed to the lack of strain rate sensitivity and the delicate balance between stress redistribution and localization in the gauge area rather than a limitation of the GTN model.

Results obtained for the NT10 simulation, Fig. 6.3, are in good agreement with experimental data for both GTN and CL-models. And only minuscule difference with regards to the fracture strain is seen between the two characteristic element dimensions $h_e = 0.25mm$ and $h_e = 0.15mm$. GTN-model captures the force-strain curves correctly until peak force, after which the model overestimates the material softening; resulting in a slightly reduced fracture strain for the T4 and T6 temper. While for the T7 temper, the fracture strain is slightly overestimated. The CL-model results are correct up to peak force, where after the CL-model is unable to capture the decline in forces. The model can also not capture the correct fracture strains cross stress triaxiality, resulting in a reduced fracture strain. The CL-model, however, more accurately predicts the local logarithmic strains than the GTN-model. Whereas the GTN-model overestimates the logarithmic strains following the peak force, the logarithmic strains are only slightly underestimated by the CL-model.

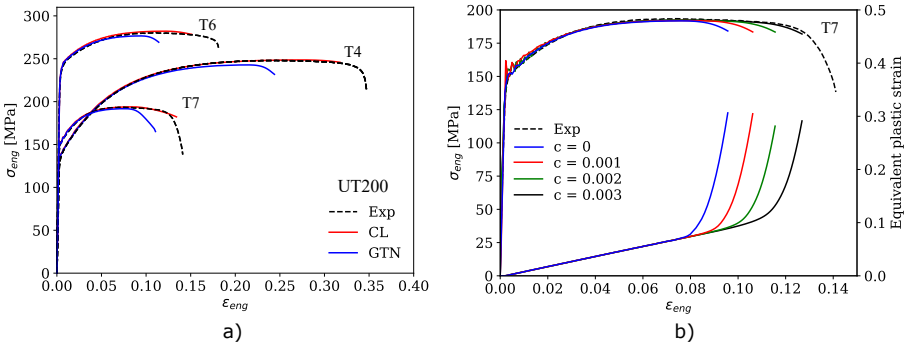

Figure 6.1: a) Experimental and numerical stress-strain curves for the UT200- test for all tempers. b) Strain rate sensitivity study for the T7 temper.

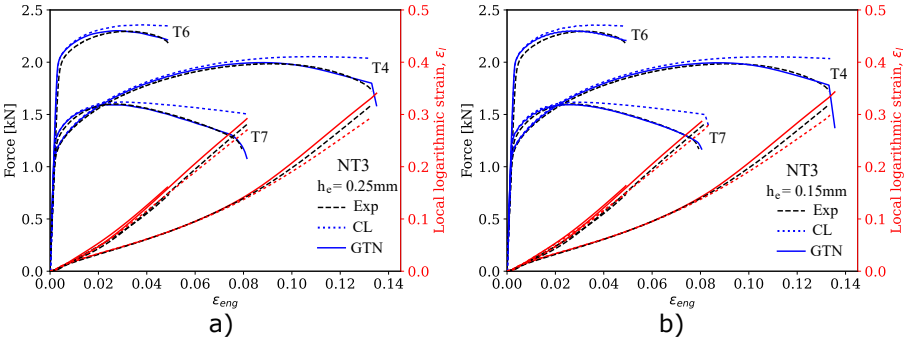

Figure 6.2: NT3 Experimental and numerical force-strain curves plotted with the logarithmic strains as a function of the engineering strains for the a) 0.25mm mesh and b) 0.15mm mesh.

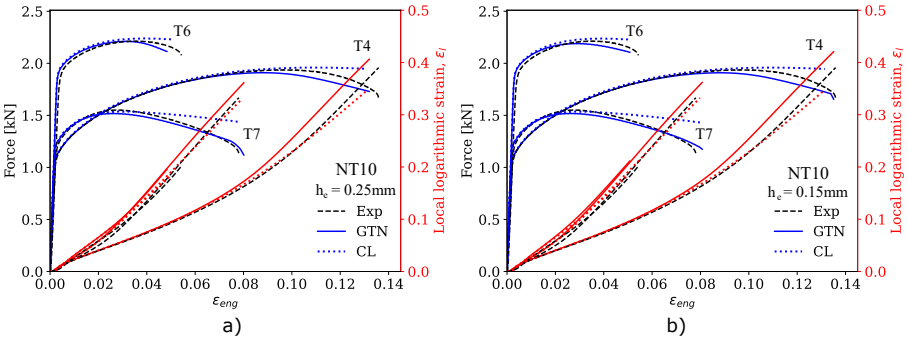

Figure 6.3: NT10 Experimental and numerical force-strain curves plotted with the logarithmic strains as a function of the engineering strains for the a) 0.25mm mesh and b) 0.15mm mesh.

Stress state histories from simulations of the smooth and notched tension tests are presented

in Fig. 6.4. The stress state histories are taken from the through-thickness center element for the NT10, NT3 and UT200 tests, which corresponds to the element subjected to the largest stresses. The stress state evolution for both material models are identical before material softening and stress localization's occurs due to void nucleation. Once the equivalent plastic strain approaches the nucleation limit, the GTN-model experiences a notable increase in stress triaxiality and lode parameter. At the same time, it remains almost uniform in the CL-model. The exception is the T7 temper, where the extensive necking due to its high ductility alters the stress state for the CL-model.

For the T7 temper, the effects of including the f_f parameter (used only for T7-temper) is seen. When the void volume fraction lies in the interval between the critical value, f_c, and failure value, f_f, the stress triaxiality is observed to increase dramatically. The lode parameter is also affected by the softening term of the GTN-model, as it shifts towards generalized shear. Since the standard Abaqus GTN-model does not include damage evolution due to deviatoric stresses, the shift in load angle does not impact simulated results. Between the two material models, it is seen that the GTN-model predicts significantly more ductile behavior with a predicted failure strain nearly twice that of the CL-model. This explains how the two models can obtain the same fracture strain for the notched specimens, even though the plastic deformation is more localized in the GTN-model.

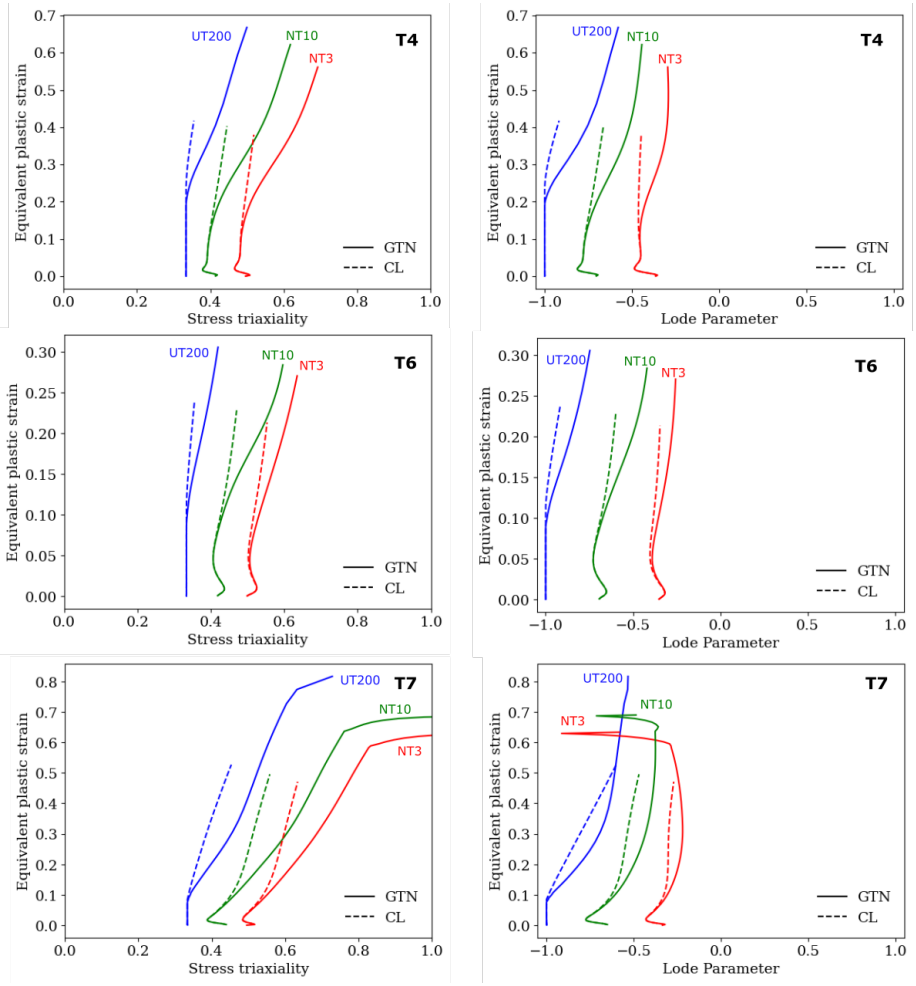

Figure 6.4: Evolution of the stress state (i.e., Lode parameter and stress triaxiality) as function of the equivalent plastic strain extracted from the critical element.

Figure 6.5 shows the deformed NT10 specimens with the equivalent plastic strain fields from the various simulations. The image of the 0.25mm models corresponds to the frame just before fracture of the first elements, while the 0.15mm models correspond to the frame where the first elements have fractured. The image represents the general trend seen for all tempers: the GTN-model predicts more localization and ductility, and consequently, the equivalent plastic strain in the most exposed elements is larger.

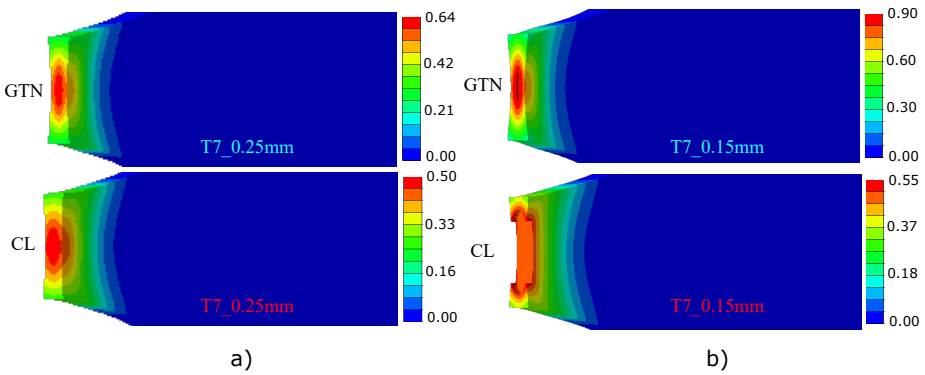

Figure 6.5: Strain fields from FE simulations of the T7 NT10-test a) just befor fracture in the 0.25 mm model, and b) just after fracture of the first elements in the 0.15 mm model.

6.2 SENT-test

Numerical results for the SENT simulations using the structured 0.25mm and 0.15mm models are shown in Fig. 6.6 and Fig. 6.7, respectively. The figures display the relation between the applied load, slit opening displacement (SOD), and the propagated surface crack displacement (SCD). Despite the UT200 test's questionable inaccuracies, excellent agreement between the numerical and experimental results is observed for the SENT-simulations.

Applying the GTN-model with $h_e = 0.25$mm, some deviations are seen following fracture initiation. T4 temper predicts the correct peak force, but subsequent force drop ensuing the peak-force is not accurately captured - SCD lagging behind and consequently follows a right-shifted path parallel to the experimental data. A similar trend is observed for the T6 temper, where the numerical results slightly overshoot the experimental peak force before also following a slightly right-shifted path as the forces drop. In contrast to the T6-temper, where the actual peak force is slightly overestimated, the T7 temper is seen to undershoot the peak force. The surface crack displacement with respect to the slit opening displacement shows that the model tends to initiate fracture slightly early for all tempers. However, the relative crack velocity is in good agreement for T6 and T4 temper but is somewhat elevated for the T7 temper.

Using the refined $h_e = 0.15$mm mesh gave improved numerical results for T6 and T7. The peak force was still slightly overestimated in the T6 temper and underestimated for T7. However, the predicted drop in forces for the T6 and T7 temper is in excellent agreement with the experimental results. The early crack initiation and slightly elevated surface crack displacements were also addressed using the 0.15mm model. Despite the refined model considerably improving the T6 and T7 temper results, the T4 results did not follow the same trend. The T4 results are seen to display a somewhat delayed fracture initiation and an inadequate relative crack velocity, and consequently overshoots the peak force and overestimates the forces during crack propagation.

The CL-model captures the experimental force-displacement data perfectly using $h_e = 0.25 = 0.25$mm, with only a slightly elevated peak force for the T6 temper. However, comparable to the 0.25mm - GTN-model, the tempers tend to initiate fracture somewhat early, and the crack propagates with a too high relative crack velocity, especially for the T4 temper. With the refined $h_e = 0.15$mm model, the overestimation of the peak force in the T6 temper is addressed, giving excellent agreement around peak force. As with the GTN-model the accuracy of the T4 results

decreases with the finer mesh, but rather than overestimating the forces, which was the case for the GTN-model, the CL-model underestimates the forces, and force-SOD curves follow a left-shifted path.

Figure 6.6a) and Fig. 6.7a) displays the fracture mode obtained for T7 simulations. The slanted fracture surface observed in the experiments was not predicted in any of the simulations as this would require omitting through-thickness symmetry (further simulation requirements for slant fracture is described in sec. 6.3.1). Instead, the crack propagated in a flat tunneling mode from initiation to complete failure for all simulations. The degree of tunneling was dependent on mesh size, temper, and material model, where the most prominent differences are displayed in the aforementioned figures. In general, the GTN-model experiences the most tunneling as the material softening leads to greater strain localization in the specimen's thickness plane compared to the CL-model.

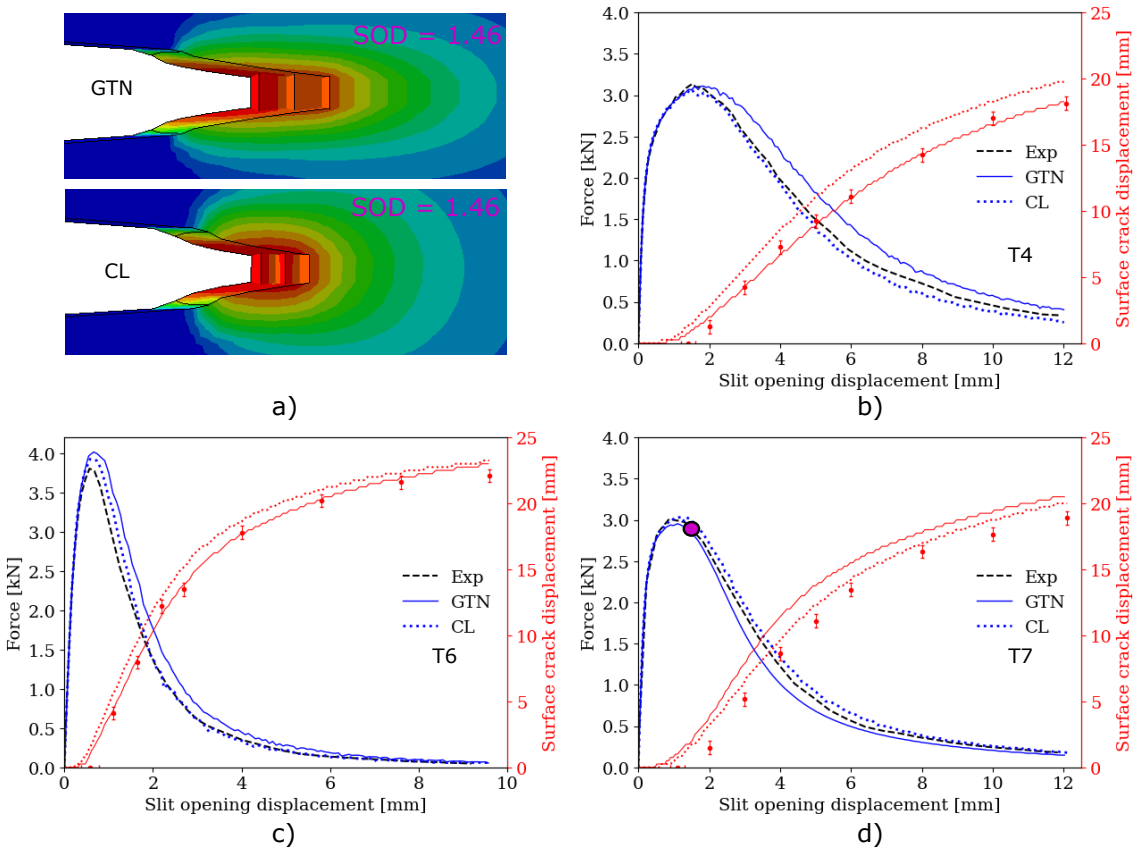

Figure 6.6: Simulated results of the SENT tests using a characteristic element length of 0.25 mm: (a) predicted crack propagation in the T7 temper, (b, c, d) Force - SOD curves along with SOD - Surface-Crack-Displacement curves of tempers T4, T6 and T7 respectively.

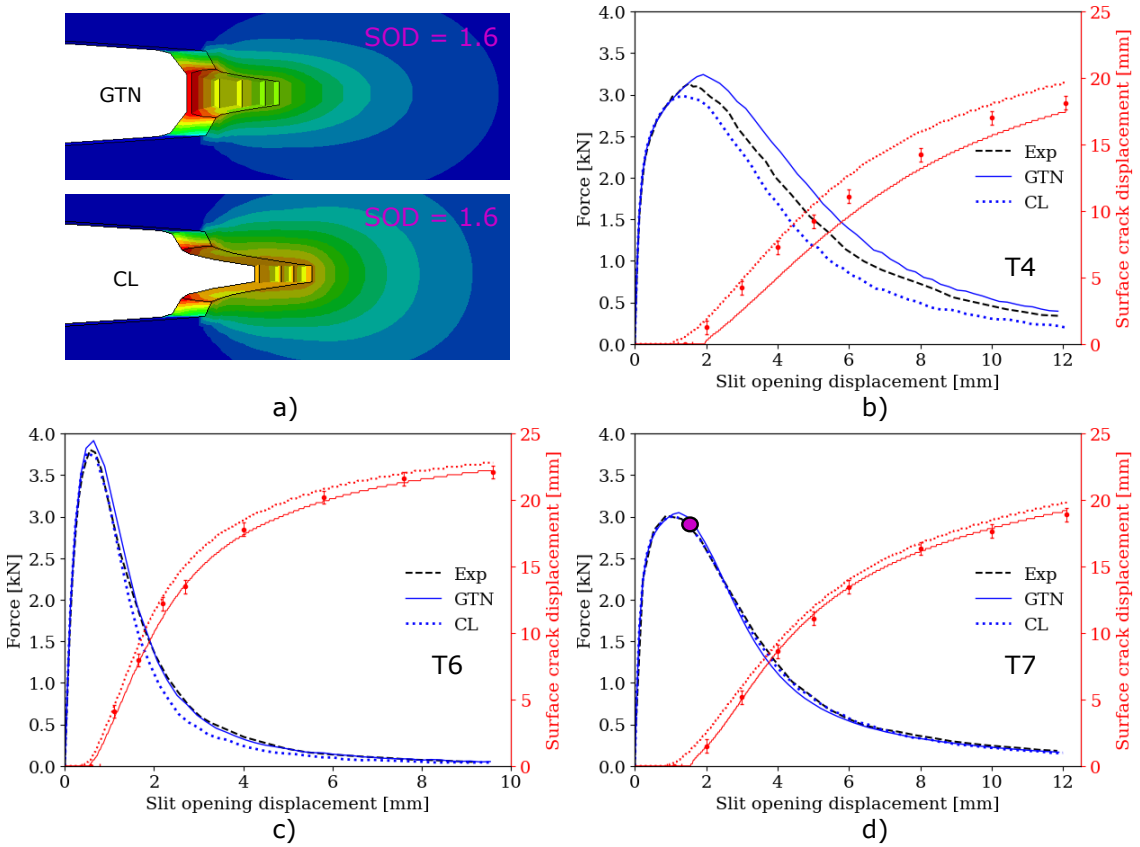

Figure 6.7: Simulated results of the SENT tests using a characteristic element length of 0.15 mm: (a) predicted crack propagation in the T7 temper, (b, c, d) Force - SOD curves along with SOD - Surface-Crack-Displacement curves of tempers T4, T6 and T7 respectively.

6.2.1 Stress state analysis

Stress triaxiality and lode from three elements at selected positions in the crack path at the through-thickness plane are extracted. Element 1, denoted: e1, corresponds to the element positioned at the slit-surface where fracture initiates, with element 2, e2, belonging to the second row of elements from the free surface, and element 3, e3, was positioned roughly half the distance to the center. The evolution of the stress-triaxiality and the lode parameter for the respective elements are plotted in Fig. 6.8. E1 is seen to experience a vastly different stress state than its counterparts, with a nearly constant stress triaxiality equal to 0.6 and a lode parameter equal to -0.6. On average, it is seen that e2 experiences the highest stress triaxiality, ranging from 0.8 and 1 for most of the loading, while the lode remains close to generalized tension at L = -1. This is consistent with theory regarding ductile crack growth; that the peak stress is reached at approximately two times the crack tip opening displacement rather than at the crack tip.[2]. Element 3, e3 represents the typical stress state evolution for the bulk of elements along the through-thickness plane that experiences failure. The stress triaxiality for e3 ranges from 0.6 to 0.8 during most of the loading, while the

Lode parameter varies between -0.25 and 0.25. The dramatic increase in the stress triaxiality and decrease in the Lode parameter seen for e2 and e3 occurs just before fracture when the crack has propagated to the element's location. Comparing the GTN-model and CL-model stress states, the stress state histories are rather similar but with fracture occurring at much lower plastic strains in the CL-model.

The average stress triaxiality and lode parameter each element experiences, located at the center-plane in the crack path, after reaching 20% of the damage threshold, $0.2 \times f_c$ for GTN and $0.2 \times W_c$, until failure are presented in A.8. The figure shows that majority of the elements experience an average stress triaxiality $= 0.8$ with a Lode parameter $= -0.2$, while the CL-model experiences a slightly reduced stress triaxiality $= 0.7$ and lode parameter $= 0$..

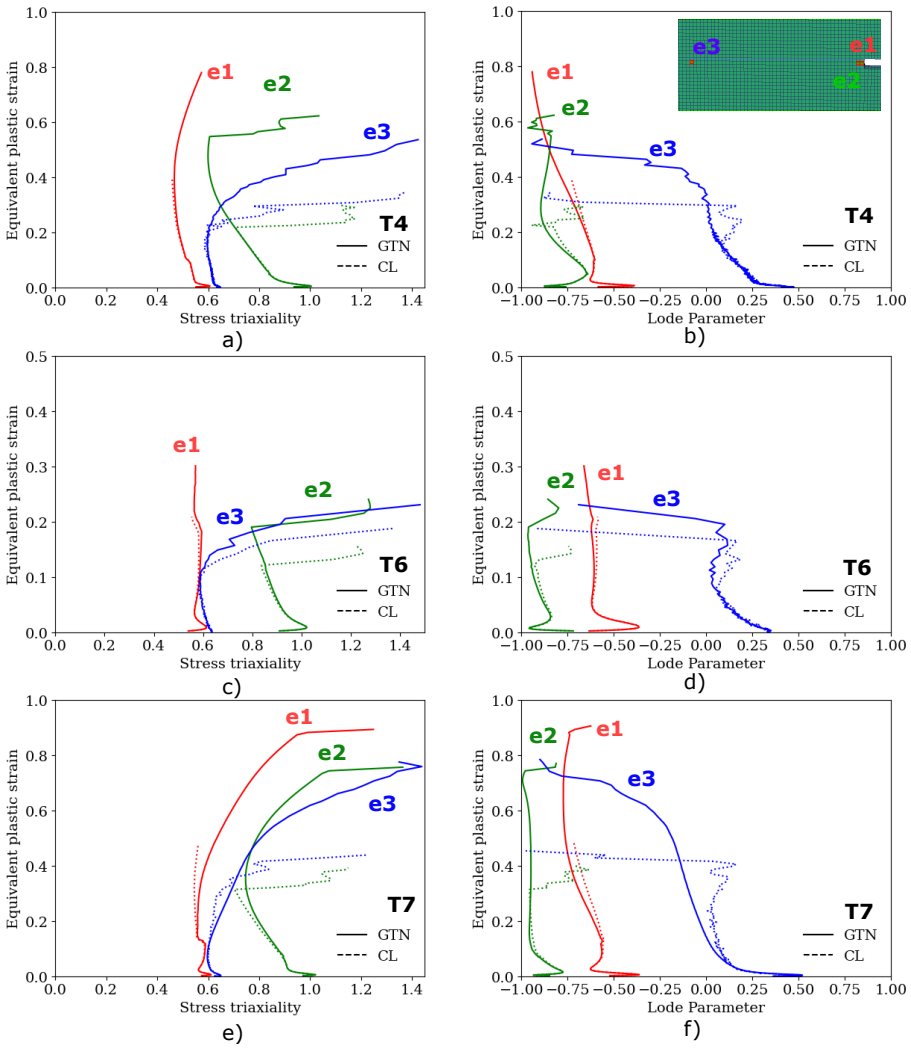

Figure 6.8: Evolution of the stress triaxiality and Lode parameter with equivalent plastic strain for elements at the center plane: e1 located at the slit opening surface, e2 located in the second row of elements behind element 1, and e3, located halfway to the specimen center.

6.2.2 Mesh structure sensitivity

The sensitivity to mesh structure for both the GTN- and CL-models was investigated by running simulations with both structured and irregular sweep mesh. The numerical results for both mesh structures combined with a 0.25 and 0.15 mm mesh size is plotted in Fig. A.9-A.10. From the GTN results, the mesh structure had a negligible effect on the force-SOD curves for the T6 and T7 models. A slight increase in resistance to crack propagation was observed for the T4 temper, especially in the regions where the mesh is generated in such a way that obstructs the preferred crack path, which by crack pinning or crack deflection increases the curvature of the crack front such

that force release rate rises. The CL-model was seen to be unaffected by the mesh structure. Figure 6.9 shows the equivalent plastic strain field map on the cracked SENT specimen for the GTN-model and CL-model for T4 temper using an irregular swept mesh with 0.15mm mesh size. It is seen that the crack propagation is considerably more developed in the CL-model than the GTN-model, and the plastic strains in the GTN-model are significantly higher. It can also be seen that the crack predicted by the GTN-model shows more curvature at the start of crack propagation compared to the CL-model.

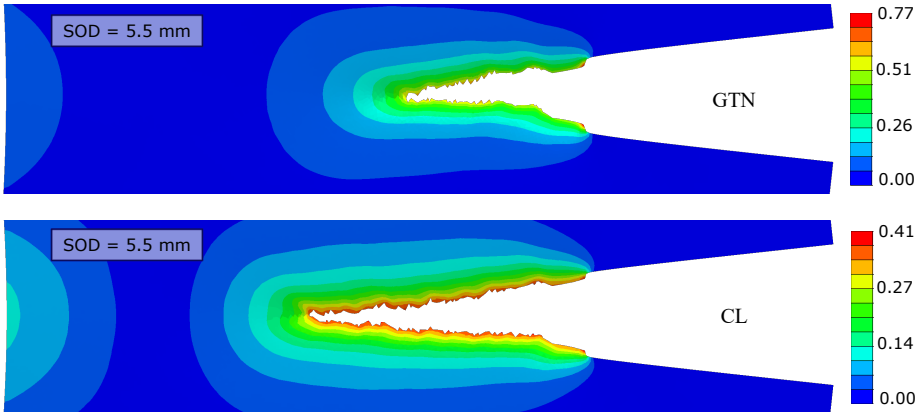

Figure 6.9: Equivalent plastic strain field map on the cracked SENT- specimen from the (top) GTN-T4 simulation and the (bottom) CL-T4 simulation.

6.3 DENT-test

Figure 6.10 shows the predicted force- slit-opening-displacement curves for the DENT-tests using the GTN-model and the CL-model. The circles on the curves mark the onset of fracture. The figure displays that both the GTN-model and CL-model can capture the experiment's general trends but slightly overestimate the peak force observed in the experiments. Crack initiation is also rather accurately predicted by the GTN-model, but consistently occurs at a lower slit opening displacement. The CL-model deviates more in terms of fracture onset, with fracture initiating at even lower slit-opening-displacement. In nearly all simulations, the fracture is initiated in the most exposed element located in the center of the slit on the free surface. However, GTN-model predicts fracture to initiate inside the plate for the T7 temper, at the second element from the free surface. Figure 3.11 shows that either fracture model did not capture the asymmetric crack path observed in the experiment. Instead, the crack propagated perpendicular to the loading direction until final separation.

After crack initiation and throughout most of the crack propagation, the GTN-model predicts a higher resistance to crack propagation than observed in the experiments, while near the point of final separation, the resistance to crack propagation is underestimated. The effect on mesh size has a negligible impact on predicted peak force but impacted crack propagation resistance. Similarly to the SENT simulations using the GTN-model, the T4 and T6 temper showed a decline in the plate's resistance to crack propagation using a finer mesh, while the T7 temper showed a slight increase. Comparing the GTN-model and CL-model curves, it is seen that for the T4 and T6 temper, the CL-model predicts a lower resistance to crack propagation compared to the GTN-model. It also

shows a lower peak force for the T4-temper. So the curve offset to the experimental data is slightly improved at fracture initiation and for the early stages of crack propagation. Like the GTN-model, the CL model's crack propagation resistance during the latter stage of the test is underestimated. The curve offset, therefore, greater near the point of final separation than for the GTN-model. The opposite trend is seen for the T7 temper, where the CL-model predicts a high resistance to crack propagation and deviating more from the experimental data.

The elevated crack initiation and propagation resistance in the numerical simulations could also result from anisotropic material behavior in the experiment, which would not be accurately described by the von Mises yield criterion. While the degree of anisotropic behavior can be seen as negligible for the experimental tests not involving neck localization, it was moderately present for the UT200 specimen. As visualized in Fig. 6.12, DENT-specimens experience a diffuse plastic zone with an embedded fracture process zone known as the necking zone. This necking zone is very much affected by any plastic anisotropy. [49].

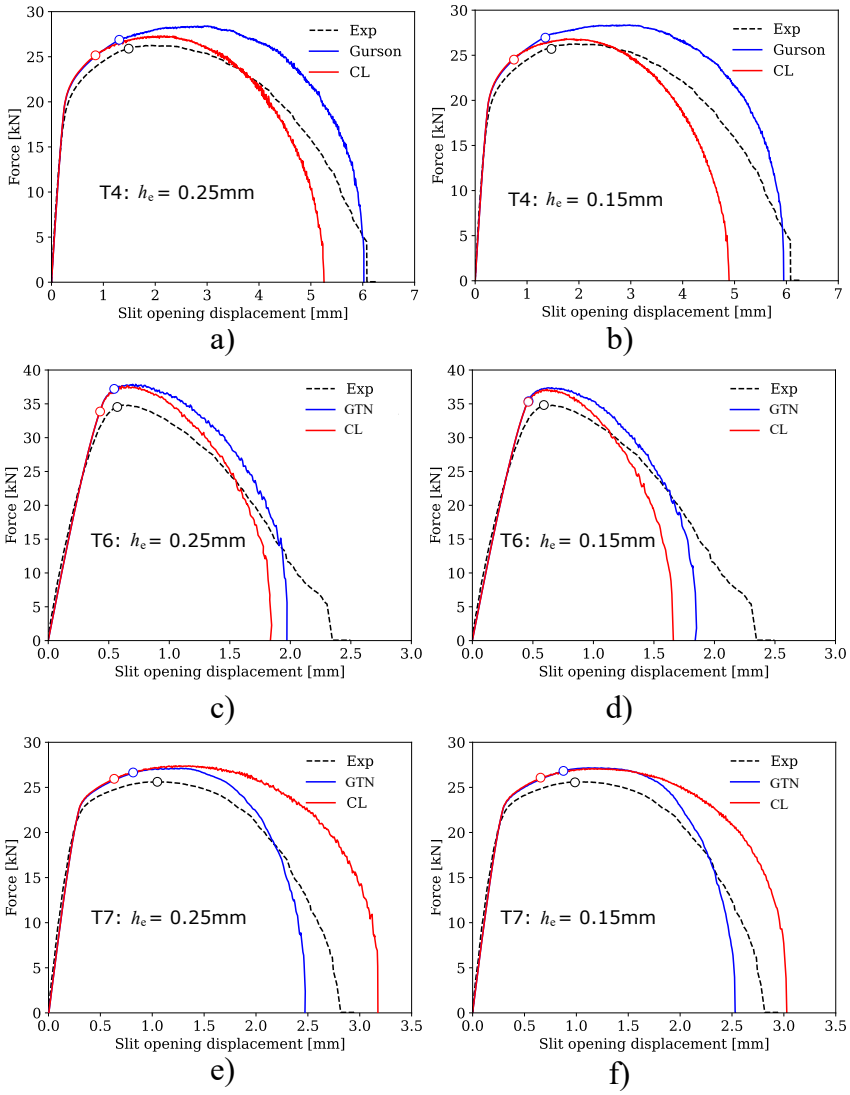

Figure 6.10: Simulated results of the DENT tests using a characteristic element length of 0.15 mm and 0.25 mm(a)predicted crack propagation in the T7 temper, (b, c, d) Force - SOD curves along with SOD - Surface-Crack-Displacement curves of tempers T4, T6 and T7 respectively

The stress state of the most exposed element at different points on the crack path is shown in Fig. 6.11. The red curves correspond to the stress state evolution of the most exposed element on the free surface of the slit opening. The green curves are representative of the stress state of the first ten elements in the vicinity to the slit opening, and the blue curves are representative of the stress state evolution of the remaining elements on the crack path. The most exposed element at the slit opening had a stress triaxiality that remained close to 0.5, and a lode parameter that remained approximately -0.75 for all tempers. According to Eq. (**??**), the damage evolves faster for

the CL-model when the Lode parameter is closer to -1. Compared to the NT3 specimens used in the calibration process, where L = -0.4, the lower Lode parameter in the DENT specimens might result in an earlier fracture. The earlier fracture for CL-model is especially notable for the T4 and T7 temper. Aside from the first element, it is seen that the elements ahead of the propagating crack are subjected to a similar stress state during most of the deformation, with stress triaxiality remaining between 0.6 and 0.7 and the Lode parameter close to zero, which roughly corresponds to plane strain conditions. The higher stress triaxiality experienced by the elements within the slit compared to those on the free surface can explain why the GTN-model predicts fracture to occur inside the specimen rather than on the free surface despite the higher equivalent plastic strains on the free surface.

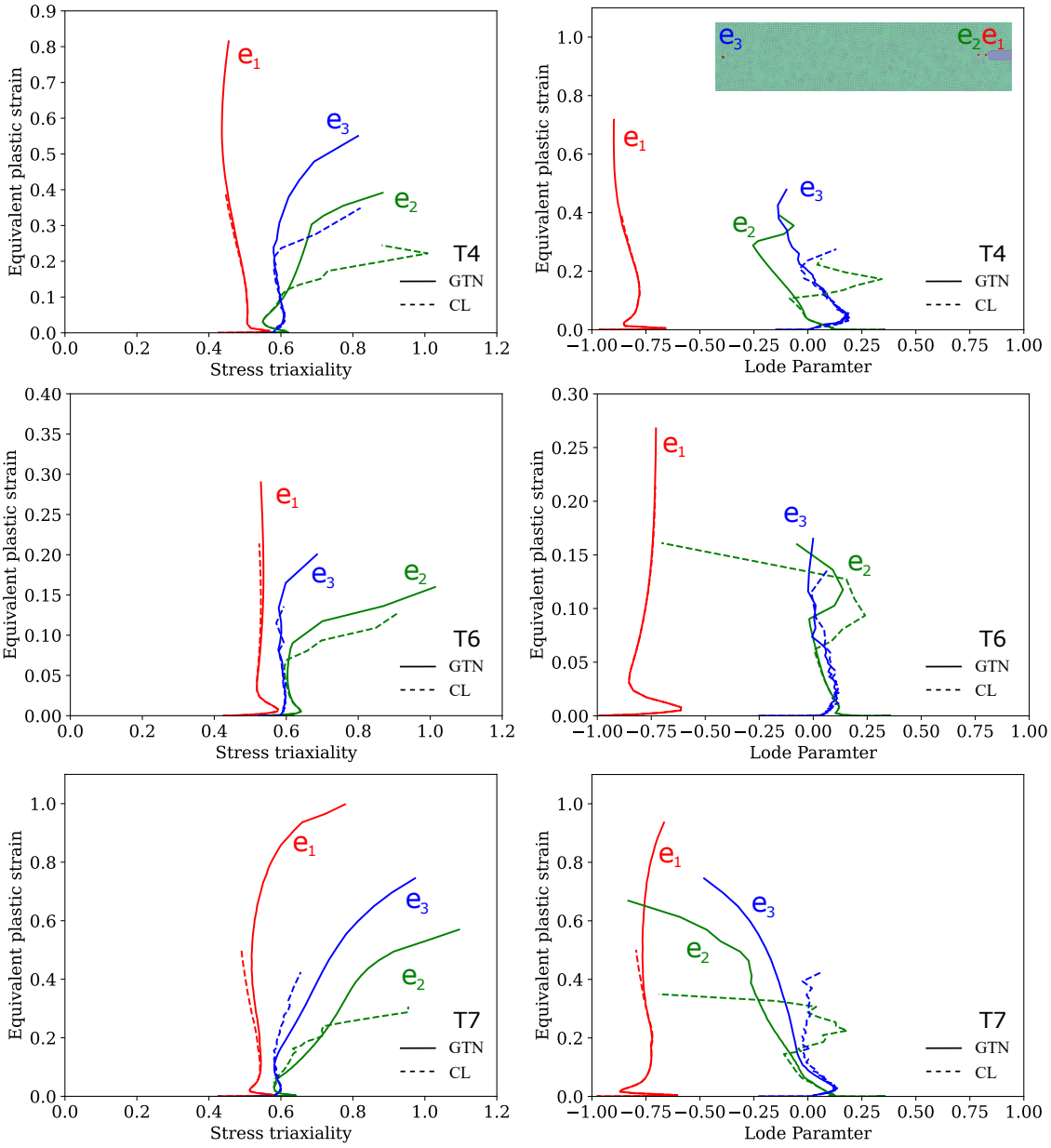

Figure 6.11: Evolution of the stress triaxiality and Lode parameter with equivalent plastic strain for elements at the center plane: e1 located at the slit opening surface, e2 representing the elements located behind element e1, and e3, representing the rest of the elements at the crack path.

Figure 6.12 shows the strain field in the vertical direction, ε_{yy} from the experiment and simulations. The field maps are taken when the crack had propagated approximately a third of the distance

to the specimen's center: SOD = 4.0, SOD =1.4, and SOD = 2.0 for the T4, T6, and T7 temper, respectively. The magnitude of the strains is consistently higher in the FE simulations than in the DIC simulations owing to the denser mesh used in the former. However, the qualitative trends are similar between the two sets of simulations for both tests. A narrow zone with localized strains in front of the propagating crack is correctly predicted in both cases. The GTN-model predicts more localization than the CL-model, and thus the maximum plastic strains in the most exposed element are consistently higher. The T7 temper sees the greatest deviation in results, with the GTN-model predicting ε_{yy} above 0.7 compared to the CL-model predictions: ε_{yy} 0.3 and the DIC results: ε_{yy} = 0.2.

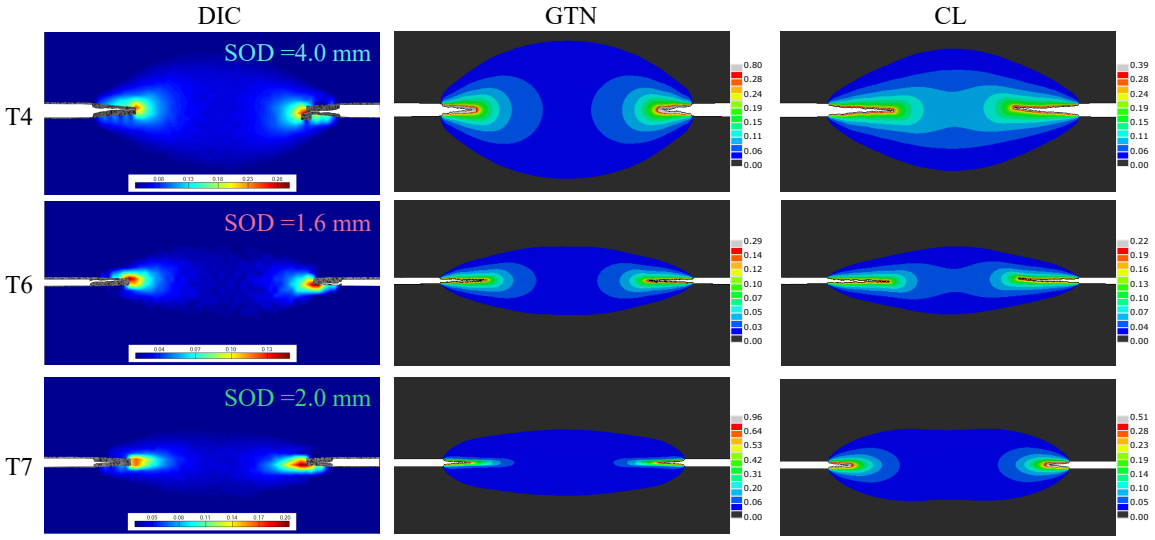

Figure 6.12: Experimental and numerical strain fields at selected slit opening displacements.

6.3.1 Revised model

Revisions to the numerical model were performed to capture the asymmetric crack propagation path found in the experimental data for the T6 and T4 temper. The following were investigated: 1) Modelling the full specimen without through-thickness symmetry such that symmetry effects could be identified. 2) Modelling the mesh in a way that steered the crack at one end upwards and the other end downwards by aligning the first few elements after the slit in a curbed manner, as seen in Fig. A.3 in the appendix. 3) Adding a horizontal load to the loading pin corresponding to the linear increasing horizontal displacement found in the experimental data.

Crack paths using the GTN-model for T6 temper is presented in Fig. 6.14. We see that removing thickness symmetry (Fig. 6.14b) had little impact on the crack path while guiding the mesh (Fig. 6.14c) had some, but still not sufficient to replicate in the experimental crack. Combining the guided mesh and removal of the thickness symmetry plane (Fig. 6.14d) further improved agreement with the experimental crack as the crack deviates slightly more from the original crack plane resulting in a nearly identical crack path to that in the experiment (seen in Fig. 6.14a). The resulting force-displacement relation was also improved at the end of the simulation when the asymmetric

deflected crack shifted direction right before linking together Fig. 6.13.

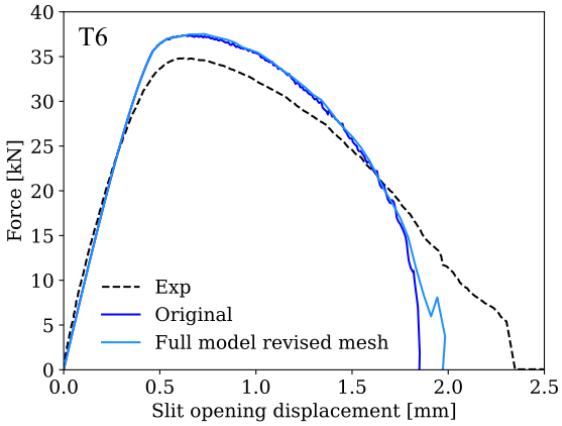

Figure 6.13: Force-displacement comparison between the original and revised model where mesh guidance is included and through thickness symmetry is omitted for the T6 temper

Including the through-thickness symmetry with revised mesh and horizontal displacement (Fig. 6.14e) gave the same results as the configuration without horizontal displacement. It did, however, recreate the horizontal displacement fields from the experiment up to peak force. Figure 6.15 presents the simulated results. The average horizontal displacement field map is replicated in the simulation, and the average horizontal displacement plotted against the average vertical displacements is in good agreement up to peak force. The CL-model was also run using the full specimen-model and revised mesh. Figure A.13 and Fig. A.14 in the appendix display the crack paths obtained using GTN and CL-model for the T4 and T6 temper. Both material models produce good representations of the experimental crack path, but CL-model overestimates the original crack plane's deviation slightly.

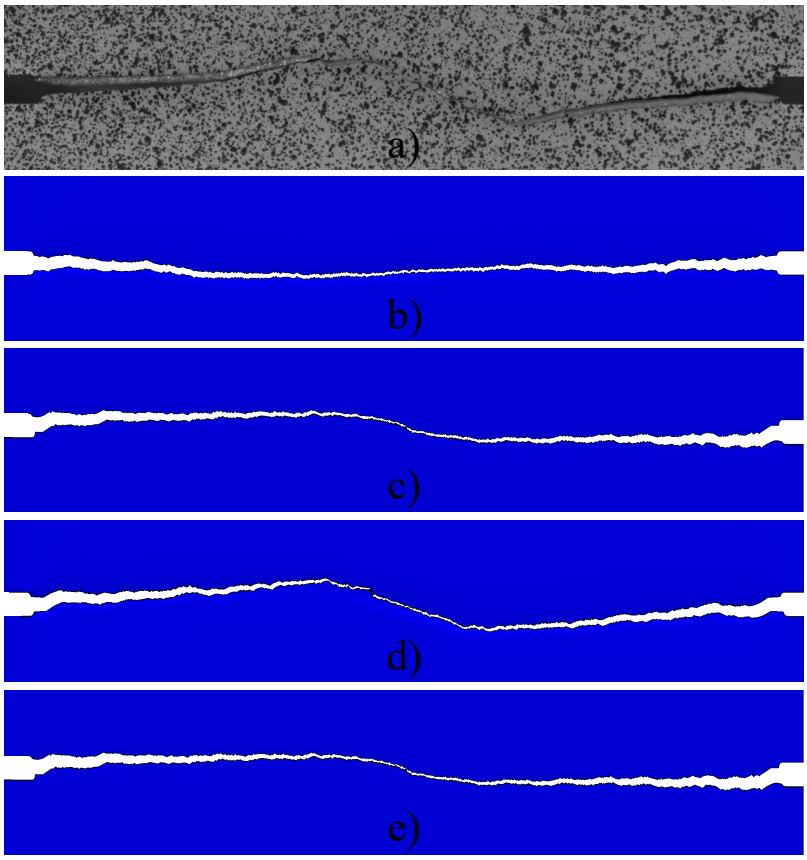

Figure 6.14: Crack path on the T6 DENT specimen from a) Experiment, and b) simulations of the full specimen (through-thickness symmetry omitted), c) simulations with a the revised mesh, d) simulations with both full model and revised mesh, and e) simulations with revised mesh and a horizontal velocity.

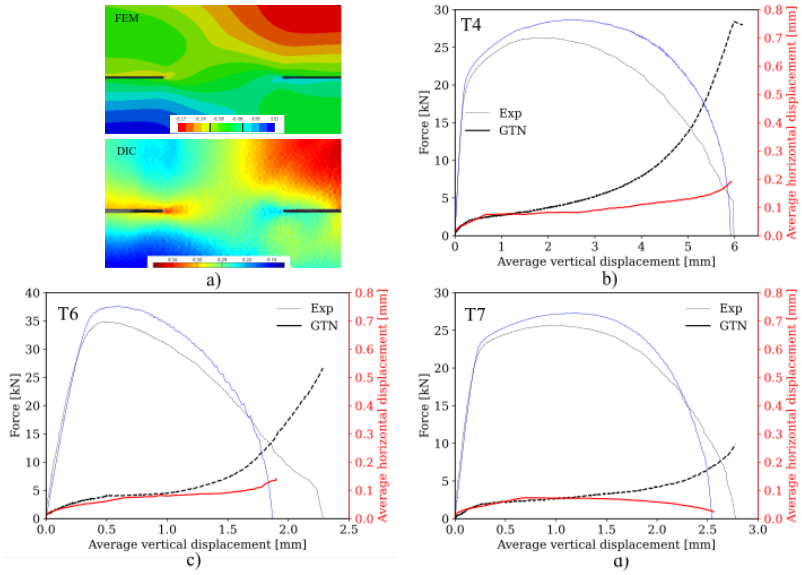

Figure 6.15: Numerical results with the revised model, including a horizontal displacement. a) display the horizontal displacement field comparison. (b, c, d) are force-displacement curves and horizontal-vertical displacement curves for (T4, T6, T7)

Neither of the material models was able to replicate slanted fracture when removing through-thickness symmetry. Several studies have investigated the slant fracture phenomenon, Liang Xue in [50] and Morgeneyer and Besson in[**?**]investigated the requirements to obtain slant fracture. Their studies showed that the slanted fracture phenomenon required both Lode dependence and weakening effects from the deviatoric stresses and the use of a refined mesh. The CL criterion is Lode dependent, but it exhibits no form of material weakening, which the study also suggests is a requirement. The same goes for the GTN-model used for this study, where neither the fracture strain nor material weakening is dependent on deviatoric stresses. For further studies, it would be interesting to investigate if an extended GTN-model containing shear contribution would replicate the slanted fracture observed for T6 and the alternating slant fracture for T4 temper.

7 Case study 1: Modified Arcan tear tests

In [16] Granum et al. conducted experiments on modified arcan specimens with dimensions shown in Fig. 7.1. The samples were clamped by four loading brackets using 12 M6-bolts. The test setup shown in Fig. 7.1 allows the plate to be loaded at various orientations. Test series were conducted with loading direction β, set to 45° and 90°. The test set-ups are labeled "Arcan-β" to specify the loading direction. A virtual extensometer of initial length 10.5 mm spanning across the notch along the longitudinal axis of the specimen in eCorr was used to extract displacements by use of 2D-DIC. The tests were conducted with a cross-head velocity of 1 mm/min. The hydraulic test machine recorded force and displacement at 10 Hz. For addition information about the experimental set-up the reader is referred to [16].

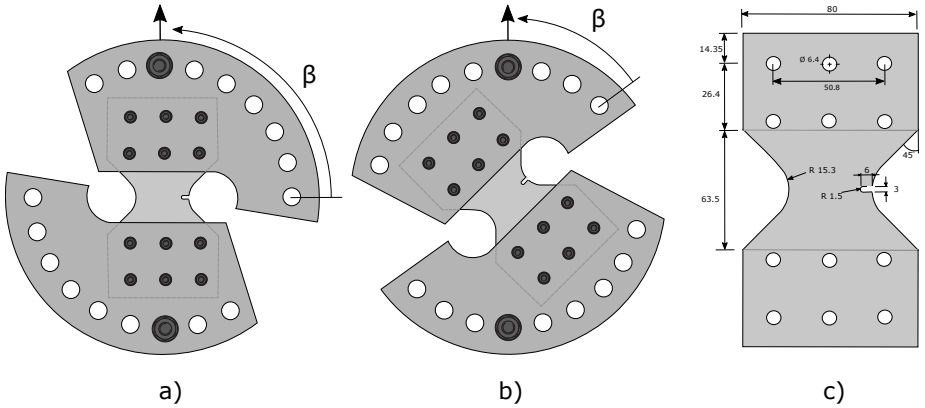

Figure 7.1: Test setup of a modified Arcan specimen with a) $= 90°$ and b) $= 45°$, and c) drawing of specimen geometry with measurements in mm.

7.1 Experimental results

The reader is referred to [16] for the experimental force-displacement curves and images of the fractured specimens. The trends observed in modified arcan tests matched those seen in the other experimental tests, where the T6 gives the highest peak force, followed by the T4, then T7 temper, while the T4 temper gives the largest displacements followed by the T7 and then T6 temper. The Arcan90 tests showed consistently higher peak forces between the two loading directions, while the displacements were more extensive in the Arcan45 test except at peak force. In the Arcan90 tests, the T6 temper was seen to fracture almost immediately after crack propagation was initiated, represented by the steep drop in forces following the peak force. Each temper followed a similar crack path: perpendicular to the loading direction. The T4 and T6 displayed the slant-fracture mode, where the alternating slant fracture phenomenon was observed for temper T4, and the T7 temper displayed the tunneling fracture mode. For the Arcan45 tests, mixed-mode loading resulted in a curved crack path for the T4 and T6 temper, while the T7 temper curved initially but continued propagation perpendicular to the loading direction. The fracture modes were comparable to those of the Arcan90 tests. For the T6 and T4 temper, the crack was arrested approximately 10mm and 5mm from the edge, respectively. After the arrest, the forces dropped below a lower threshold, stopping the test. The observed fracture surface for the T7 temper was rough with evident shear

lips, whereas the fracture surface for the T6 and T4 was smooth.

7.2 Numerical modelling

The modified Arcan tests were assembled according to Fig. 7.1, with symmetry planes omitted. The specimen was modelled with characteristic element length, $h_e = 0.15$mm, giving ten elements across the thickness. An MPC beam constraint was used to connect the upper and lower part of the specimen to reference points located at the loading and support pins, thus omitting the specimen's clamped region by presuming it behaves like a rigid body. The load reference point had a single translational degree of freedom and assigned a 500mm/s velocity in the load direction. Both reference points were allowed to rotate in-plane to recognize rotations induced by the pinned link. The displacements were taken as the distance between two nodes on either side of the notch (see Fig. 7.1).

7.3 Numerical results

Figure 7.2 shows the force-displacement curves for the arcan45 tests along with the experimental and simulated crack paths. The numerical models are seen to capture the general trends of the experiment with good accuracy. The predicted force-displacement curves using the GTN-model are seen to follow a similar trend to the SENT-simulations, where excellent agreement is obtained for the T6 and T7. At the same time, the force level is overestimated for the T4 temper. The CL predictions are also comparable to the SENT-results as the model slightly underestimates the force level for all tempers. Fracture initiation was accurately captured by both models, with fracture initiating at the peak force for all tempers. The curved crack path observed in the T4 temper was predicted by both models but slightly to the left of the experimentally observed crack path. For the T6 temper, the correct crack path is predicted using the CL-model whereas the GTN-model predicts crack propagation along a straight line. This could be an artifact of the structured mesh in the crack region which obstructs the crack from leaving its plane. The straight crack path for the T7 temper was accurately predicted by the GTN-model, while the CL-model predicts that it initiates in a straight crack path but deflects halfway through the specimen.

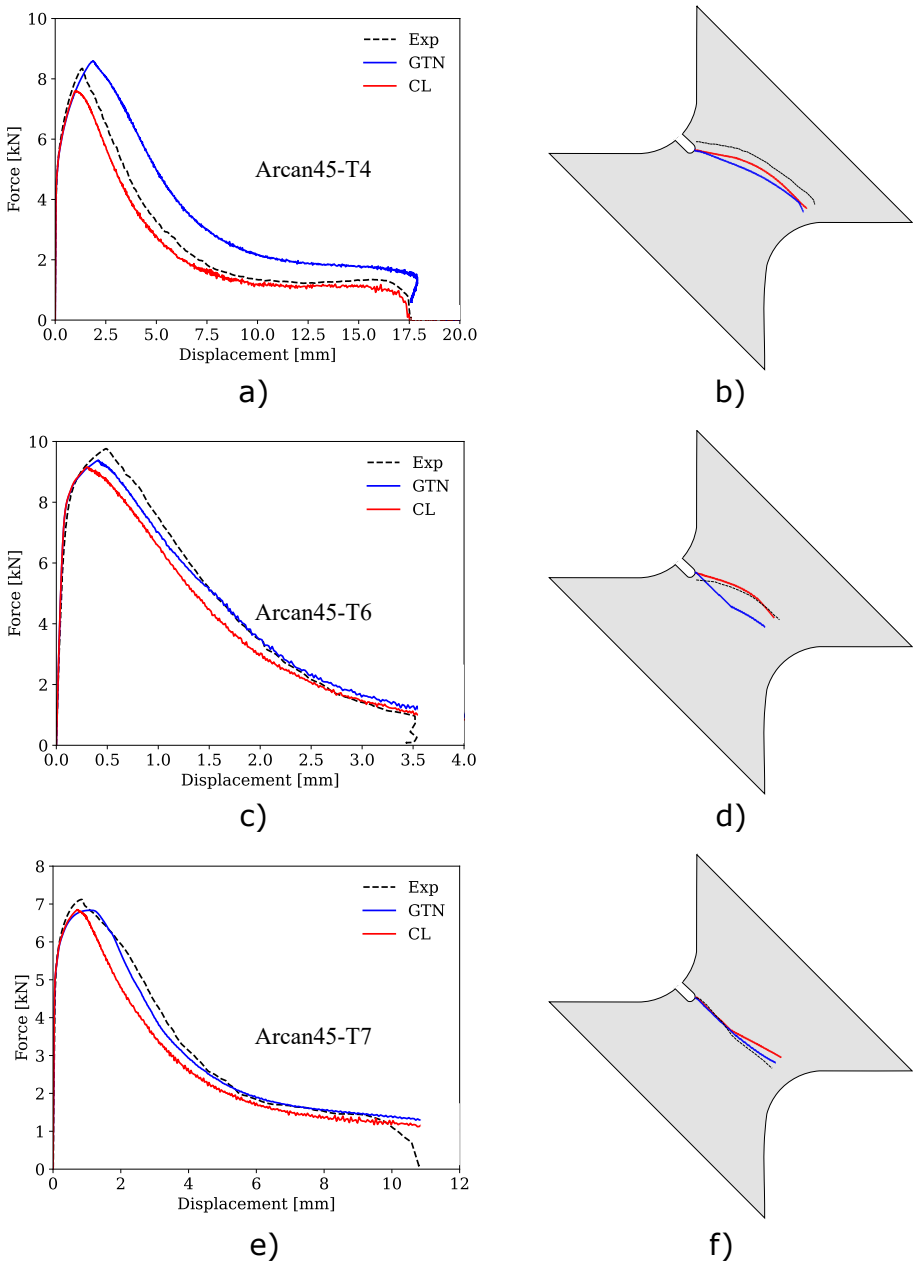

Figure 7.2: Experimental and numerical force-displacement curves for the Arcan45 tests in a), c) and e) and corresponding crack paths on the undeformed configuration in b), d) and f).

The experimental and numerical force-displacement curves for the Arcan90 tests are shown in Fig. 7.3. The force-displacement curves are shown to be in good agreement. The GTN-model predicts the correct peak force for the T4 temper while slightly underestimating the peak force in the T6 and T7 temper. For the CL-model, the forces are consistently underestimated in the T4 and T6 temper whereas excellent agreement is obtained for the T7 temper. Neither model was able to capture the abrupt failure in the Arcan90-T6 specimen.

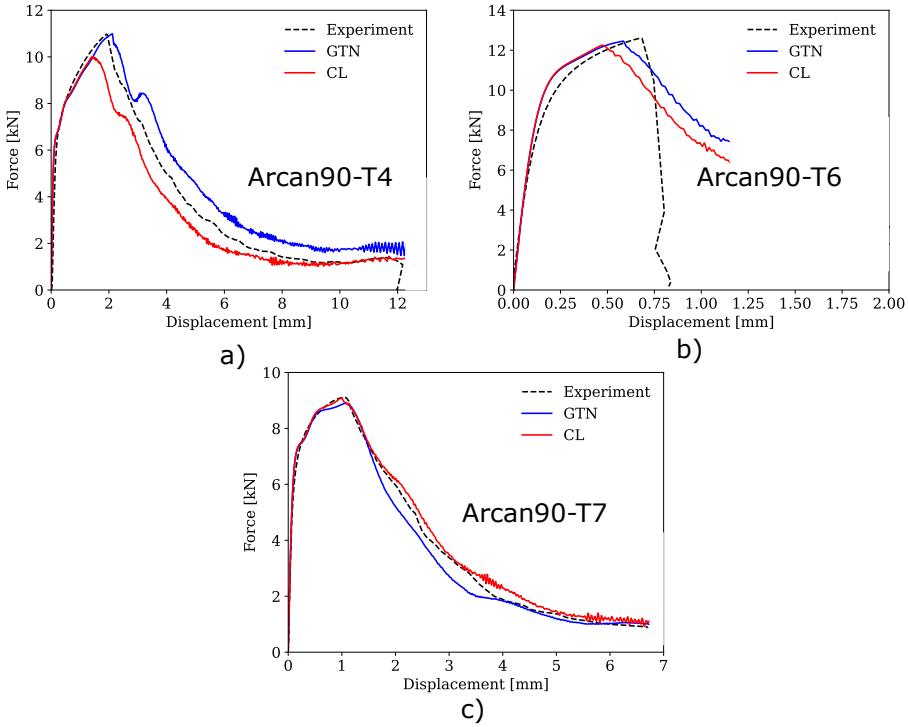

Figure 7.3: Experimental and numerical force-displacement curves for the Arcan90 tests, for temper a) T4, b) T6, and c) T7

8 Case study 2: Drop weight impact tests

To assess the calibrated fracture models ability to predict crack propagation in AA6016 plates subjected to dynamic loading conditions, drop weight impact tests were simulated and compared to existing experimental test data.

8.1 Experimental setup

Drop weight tests were conducted in [1] on square target AA6016 aluminium plates with dimensions 312.5 mm × 312.5 mm × 1.5 mm and a star-shaped slit at the center oriented 45° to the rolling direction, Fig. 8.1). The tests were conducted with an Instron CEAST 9350 dropped-objects-rig; a 14kg striker with hemispherical tip and an initial velocity of 4m/s was used in the test. The plates were clamped between two circular frames with an inner diameter of 200 mm, using 12 equidistant M12 bolts resulting in essentially fixed boundary conditions. Experimental setup is illustrated in Fig. A.16. Forces were measured by a strain-gauge sensor attached to the striker, and the striker's displacement calculated from the logged forces through Eq.(B.13-B.15) in the appendix. Two phantom v1610 high-speed cameras positioned beneath the aluminum plate, recording the test at 15,000 frames per second, were also implemented in the test configuration. The reader is referred to [1] for a more details on the experimental setup.

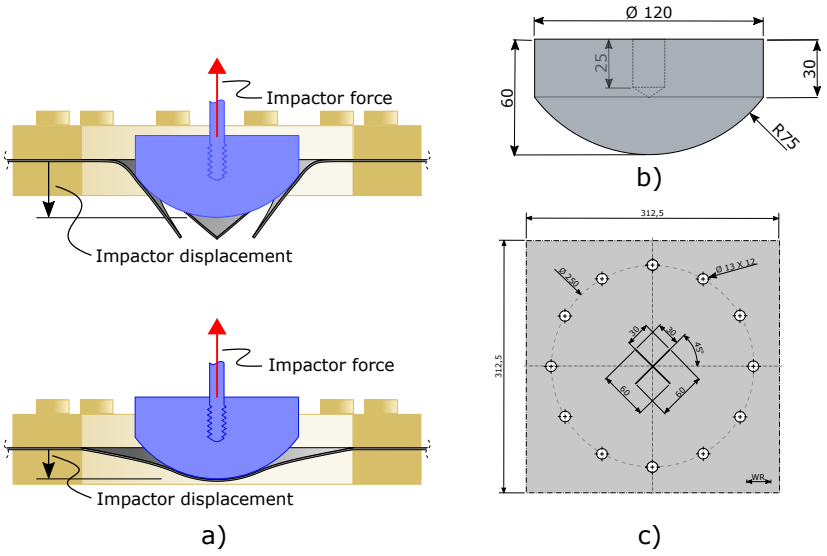

Figure 8.1: a) Illustrative drawing of the dropped weight impact test, created by Vetle Espeseth. Geometry of b) impactor with hemispherical tup and c) square target plate with 45° slit, with measurements in mm.

8.1.1 Numerical modelling

The assembly used for the drop weight test can be seen in Fig.8.2. The plate was modeled using two symmetry planes, and the outer boundary of the plate was fixed against displacements to mimic the effect of the clamping plates. A local segment in the crack zone was meshed with $h_e = 0.15mm$ with a single element in the slit opening, while the global mesh was set to 1.5 mm. The impactor

was modeled as a 3D analytical rigid shell and assigned a reference point marked RP positioned at the apex of the impactor, through which inertial properties and boundary conditions were set. It was constrained to only allow velocity in the direction perpendicular to the plate. Interaction between the plate and impactor was modeled using general contact with a friction coefficient (μ) set to 0.1. Force-displacement data from the simulations were obtained by extracting the acceleration and lateral displacements from the reference point.

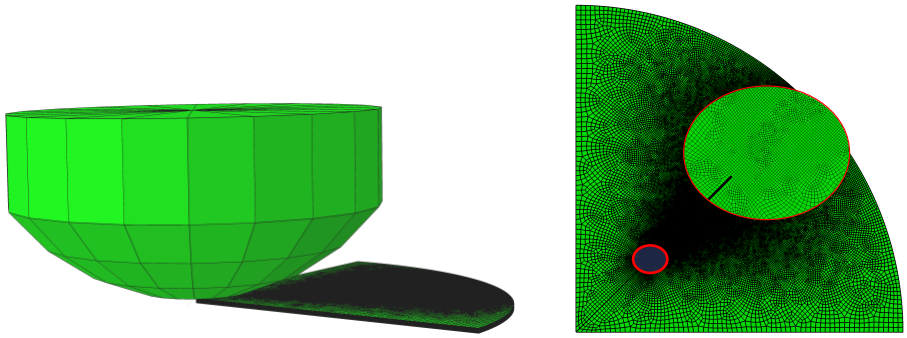

Figure 8.2: A) Numerical model of the hemispherical impactor and plate and b) Meshed plate, with irregular swept mesh in the predicted crack region.

8.1.2 Numerical and experimental results

Figure 8.3 shows the force-displacement curves for the the drop tests along with an in-plane view of the deformed T6 plate. Both models are seen to capture the general trends of the experiment. For the T6 and T7 temper, both material models predict a similar behavior, i.e., the forces saturate slightly before the experimental forces, and consequently the peak force is underestimated. For the T4 temper the GTN-model predicts a higher resistance, while CL predicts a lower resistance. The stress state resembles what was found in the SENT simulation with a stress triaxiality of 0.6 and lode around 0 in front of the propagating crack. The deviation from experimental data can be attributed to a wrong friction coefficient. Results obtained in [1] with respect to the effects of μ are shown in Fig. 8.4. The figure presents results obtained from the same experimental test (with a different velocity) and displays how increasing μ from 0.1 to 0.5 increase the resistance for T7 and T4 temper. For T6, μ ranges from 0.1 to 0.3 and suggests the same effects. This suggests that accurate results for all tempers could be obtained by increasing μ for CL, but only improve the results for T6 and T7 for GTN. This is consistent to the results obtained for both Arcan45 and SENT simulations, where the T4 calibrated GTN parameters predicts a delayed fracture.

The friction coefficient used for this study was set ($\mu = 0.1$) which is far less than what usually found between the steel-aluminium interface. For example, [51] suggests that the friction coefficient for steel- aluminium interfaces start at an initial value of 0.2, increase to almost 0.8 in the elastic region, and then decrease to the value of 0.6 in the plastic region.

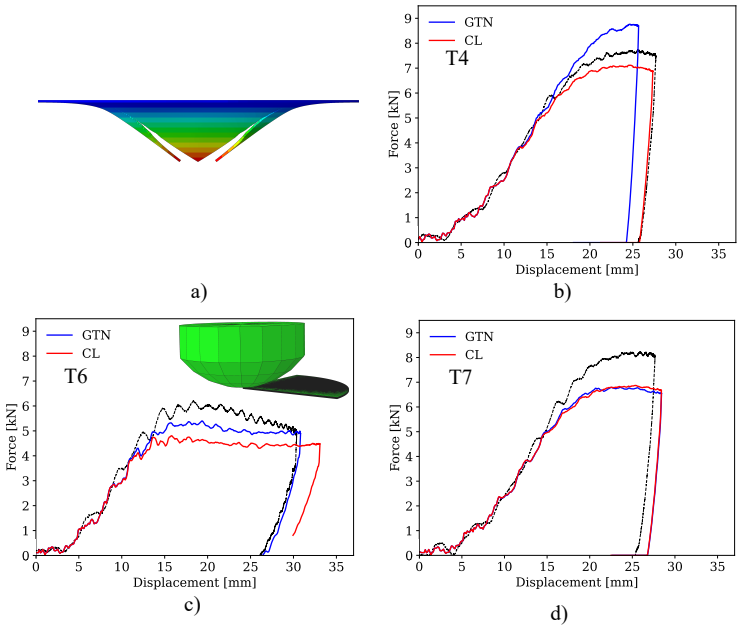

Figure 8.3: a)Deformed plate from the T6 drop test simulation and experimental and numerical force-displacement curves for temper b)T4, c)T6 and d)T7.

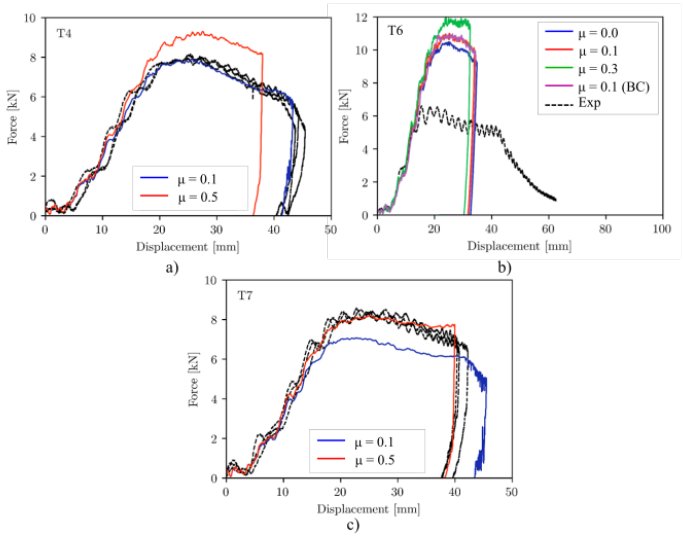

Figure 8.4: Experimental and numerical force-displacement curves for the Drop-test for different friction coefficients using temper a)T4, c)T6 and e)T7. [1]

9 Summary

This study has presented a calibration procedure of the Gurson-Tvergaard-Needleman (GTN) fracture model and the Cockroft-Latham (CL)) fracture model, and applied it for three tempers of the aluminium alloy AA6016. Two experiments were used to calibrate the models, smooth tension (UT200) tests for the hardening parameters, and Notch tension (NT3) tests for the damage and fracture parameters. The fracture parameters were calibrated to two characteristic element dimensions $h_e = 0.25mm$ and $h_e = 0.15mm$. Both fracture models were then validated against notch tension(NT10) tests, single edge notch tension (SENT) tests, double edge notch tension (DENT) tests, modified Arcan test loaded at a 45- and a 90-degree angle, and to a drop-weight impact test on plate targets with center oriented slits. The goal was to assess the predictive capabilities of the calibrated GTN-model, where the easily calibrated CL-fracture model was used for comparison. The difference in CPU time between the two models was minimal; with the GTN model using roughly $1.1\times$ the time for CL. Finite element simulations using the von Mises plasticity model combined with both the GTN-model and CL-model were, in most cases, capable of accurately predicting the initiation of fracture and the force-displacement relation found in the experimental data. The results did not necessarily improve when refining the mesh from a characteristic length of 0.25mm to 0.15mm, suggesting that $h_e = 0.25$ is sufficient to replicate the force-displacement relation for crack propagation in thin plates. However, for the model to replicate the slant-fracture surface seen in the T4 and T6 temper, a much denser mesh is likely required along with a shear dependent damage term. The T4 temper was the only temper where substantial deviations occurred for the two fracture models. The GTN model usually performed worse than CL by predicting an elevated resistance to crack initiation and propagation. This may suggest that the calibration method applied in this study is less suited for materials experience extensive work hardening. The GTN-model also had problems replicating the fracture strain for UT200 specimens as the added material softening resulted in an earlier and accelerated necking process. However, the GTN model performed slightly better than CL in predicting the fracture strain for NT10. Giving a mixed result on which fracture model can predict correct fracture strain for a range of stress triaxiality. The study also presents the effects of adding pressure dependence on stress triaxiality, lode parameter, equivalent plastic failure strain, and crack propagation mode by comparing the two fracture models. The tendency found throughout is that the stress localization due to material softening results in a higher stress triaxiality, and the lode parameter shifts towards generalized shear. A major difference in ductility is seen between the fracture models. It is evident that the calibrated GTN-parameters predict more necking before fracture than experimental tests suggests, while the CL model underestimates strains at necking. In all simulations the crack propagated in a tunneling mode (even when through thickness symmetry was omitted), though but the tunneling mode was more prominent when adding pressure sensitivity. A sensitivity study was performed for the DENT specimen simulations to capture the unexpected asymmetric crack path and horizontal displacement in the experimental tests. The results suggest that T4 and T6 temper are extremely sensitive to the mesh design, and are inclined to deviate from the original crack plane. By omitting through-thickness symmetry and simply guiding the mesh slightly asymmetrically at the vicinity of the slit, the correct crack path was replicated for both tempers with the GTN model. CL-model was seen to be even more sensitive, as the resulting crack path became too asymmetrical. The horizontal displacement field was replicated by adding some horizontal displacement to the loading pin.

10 Conclusion

The potential of the GTN-model in predicting the ductile fracture process is well documented. Herein, GTN-model parameters and the CL-fracture parameter were identified for three tempers of AA60616 aluminium. The aim was to assess the GTN-models accuracy, efficiency and robustness in simulating crack propagation in thin aluminium alloy plates, where the CL-fracture criterion was used for model comparison. The material models were validated under both quasi-static and dynamic loading conditions. In the following sections, concluding remarks and proposals for future work are presented.

- Calibrating the GTN-model to multiple specimens proved challenging, whereas good agreement was obtained for the NT10 test, the numerical results of the UT200 test were unsatisfactory.
- The failure parameters in the GTN model were considerably more mesh sensitive than the CL-fracture parameter.
- The accuracy of the models was shown to vary between the tempers, where the T4 temper predictions deviated the most from experimental data. The GTN model was shown to consistently overestimate the forces in the T4 temper, while the CL mostly underestimated forces.
- Good correlation was detected between the quasi-static and dynamic experiments which corroborates with the notion that quasi-static experiments can give satisfying validation for this type of experiment on AA6016.
- Both models gave good results in terms of fracture initiation, with slightly better results for the GTN model.
- The CL criterion proved better at predicting the correct crack path under the mixed mode loading conditions of the Arcan45 test.
- The results using the two mesh sizes in the critical region did not deviate substantially, nor was the finer mesh able to capture the slant-fracture mode from the experiments.
- Despite the greater complexity of a coupled damage criterion, the computational efficiency of the GTN model in Abaqus is approximately the same as for the CL model.

10.1 Proposal for future fork

In this study the isotropic yield criterion was adopted in the material model. However, some degree of anisotropy was found in both the uniaxial tensile tests and the SENT-tests and can therefore be a source of deviation between the numerical and experimental results, especially for DENT simulation. It would thus be interesting to investigate and compare the performance of an extended GTN-model where an anisotropic stress measure is implemented. Alternately the Hershey yield criterion, which resembles an anisotropic yield criterion, with yield surface in between the Tresca and von Mises yield surface could be utilized. The simple GTN model used in this study is also impaired when it comes to predicting fracture or localization under shear dominated loading states. The same limitation extends to the ability to capture the slanted fracture observed for T6 and alternating slanted fracture for T4. It would thus be interesting to see if extending the model to include softening from shear

will improve the crack propagation predictions and whether it could capture the slanted fracture mode.

The high resolution images captured of the SENT-test made it possible to take measurements of the surface crack displacements with tolerable accuracy. For the DENT-test however, the lower resolution images in combination with the black and white speckle pattern on the specimen surface, made detecting the surface crack front more cumbersome, and measurements with adequate accuracy could not be made. Further investigation of crack propagation in the DENT-tests could thus benefit from higher resolution images. It would also be interesting to attain measurements of the crack displacement at mid-plane such that the GTN-models performance in predicting the degree of tunneling could be assessed. Furthermore, the cause for the disproportionate loading conditions in the DENT-tests was not discovered, and thus there is some uncertainty to which extent comparison of the idealistic simulated data to experimental data can be used to assess the performance of the GTN-model. It would therefore be interesting to conduct a new set of tests and attempt to better survey the boundary conditions such that more ideal conditions are met or that any disproportion can be identified.

References

[1] Vetle Espeseth. Untitled manuscript. unpublished.

[2] T. L. Anderson. *Fracture Mechanics Fundamentals and Applications*. Third EDITION. Taylor & Francis Group,LLC, 2005.

[3] O. S. Hopperstad and T Børvik. Lecture notes, material mechanics, part 1, norwegian university of science and technology.

[4] Juergen Hirsch. Recent development in aluminium for automotive applications. *Transactions of Nonferrous Metals Society of China*, 24:1995–2002, 07 2014.

[5] J. Gurland and J. Plateau. The mechanism of ductile rupture of metals containing inclusions. *Trans. ASM*, 56:442–454, 01 1963.

[6] F. A. McClintock. A Criterion for Ductile Fracture by the Growth of Holes. *Journal of Applied Mechanics*, 35(2):363–371, 06 1968.

[7] D. M. Tracey J. R. Rice. On the ductile enlargement of voids in triaxial stress fileds. *J. Mech. Phys. Solid*, 17:201–217, 1969.

[8] A. L. Gurson. Continuum Theory of Ductile Rupture by Void Nucleation and Growth: Part I—Yield Criteria and Flow Rules for Porous Ductile Media. *Journal of Engineering Materials and Technology*, 99(1):2–15, 01 1977.

[9] V. Tvergaard. Influence of voids on shear band instabilities under plane strain conditions . *International Journal of Fracture*, 17(4):389–407, 1981.

[10] V. Tvergaard and A. Needleman. Analysis of the Cup-Cone Fracture in a Round Tensile Bar. *Acta metall*, 32(1):157–169, 1984.

[11] Ravi Kiran and K. Khandelwal. Gurson model parameters for ductile fracture simulation in astm a992 steels. *Fatigue & Fracture of Engineering Materials & Structures*, 37, 02 2014.

[12] Sondre Bergo, David Morin, Tore Børvik, and Odd Hopperstad. Micromechanics-based identification of a ductile fracture model for three structural steels. *Engineering Fracture Mechanics*, 224:106803, 12 2019.

[13] Lars Edvard Dæhli, Jonas Faleskog, Tore Børvik, and Odd Hopperstad. Unit cell simulations and porous plasticity modelling for strongly anisotropic fcc metals. *European Journal of Mechanics - A/Solids*, 65, 05 2017.

[14] K. Nahshon and J.W. Hutchinson. Modification of the gurson model for shear failure. *European Journal of Mechanics - A/Solids*, 27:1–17, 02 2008.

[15] Matthieu Dunand and Dirk Mohr. On the predictive capabilities of the shear modified gurson and the modified mohr-coulomb fracture models over a wide range of stress triaxialities and lode angles. *Journal of The Mechanics and Physics of Solids - J MECH PHYS SOLIDS*, 59:1374–1394, 07 2011.

[16] Henrik Granum, David Morin, Tore Børvik, and Odd Hopperstad. Calibration of the modified mohr-coulomb fracture model by use of localization analyses for three tempers of an aa6016 aluminium alloy. *International Journal of Mechanical Sciences*, 192:106122, 10 2020.

[17] Zhenyu Xue, M.G. Pontin, F.W. Zok, and J.W. Hutchinson. Calibration procedures for a computational model of ductile fracture. *Engineering Fracture Mechanics*, 77:492–509, 02 2010.

[18] Lars Edvard Dæhli, David Morin, Tore Børvik, and Odd Hopperstad. Influence of yield surface curvature on the macroscopic yielding and ductile failure of isotropic porous plastic materials. *Journal of the Mechanics and Physics of Solids*, 107:253 – 283, 07 2017.

[19] Roger Lumley. *Fundamentals of Aluminium Metallurgy: Production, Processing and Applications*. Woodhead Publishing in materials. Elsevier Science & Technology, Cambridge, 2010.

[20] J. Gilbert Kaufman. *Introduction to Aluminum Alloys and Tempers*. Third EDITION. ASM International, 2000.

[21] J.E. Hatch, A. Association, and A.S. Metals. *Aluminum: Properties and Physical Metallurgy*. Aluminum / J.E. Hatch Hrsg. American Society for Metals. American Society for Metals, 1984.

[22] Zhenzhen Fan, Xiuchuan Lei, Lu Wang, Xiaofang Yang, and Robert Sanders. Influence of quenching rate and aging on bendability of aa6016 sheet. *Materials Science and Engineering: A*, 730, 05 2018.

[23] ASM Handbook Committee. *Heat Treating of Aluminum Alloys*. Volume 4. ASM International, 1991.

[24] Joseph Bluhm and Robert Morrissey. Fracture in a tensile specimen. *Proc. 1st Int. Conf. Fracture*, 3:66, 07 1966.

[25] E. W. Weisstein. Kronecker delta. from mathworld–a wolfram web resource.

[26] O. S. Hopperstad and T Børvik. Impact mechanics – part 1: Modelling of plasticity and failure with explicit finite element methods, structural impact laboratory.

[27] J. Lubliner. *Placticity Theory*. Pearson Education, Inc, 1990.

[28] O. S. Gruben, G. Hopperstad and T Børvik. Evaluation of uncoupled ductile fracture criteria for the dual-phase steel docol 600dl. *International Journal of Mechanical Sciences*, 62(1):1374–1394, 2012.

[29] M. G. Cockroft and D. J. Latham. Ductility and the workability of metals. *Journal of the Institute of Metals*, 96:33–39, 1968.

[30] Henrik Granum, Vegard Aune, Tore Børvik, and Odd Hopperstad. Effect of heat-treatment on the structural response of blast-loaded aluminium plates with pre-cut slits. *International Journal of Impact Engineering*, 05 2019.

[31] Jens Kristian Holmen, Jan Solberg, Odd Hopperstad, and Tore Børvik. Ballistic impact of layered and case-hardened steel plates. *International Journal of Impact Engineering*, 02 2017.

[32] Mikhail Khadyko, Stephane Dumoulin, Tore Børvik, and Odd Hopperstad. Simulation of large-strain behaviour of aluminium alloy under tensile loading using anisotropic plasticity models. *Computers & Structures*, 157, 09 2015.

[33] Marion Fourmeau, Tore Børvik, Ahmed Benallal, and Odd Hopperstad. Anisotropic failure modes of high-strength aluminium alloy under various stress states. *International Journal of Plasticity*, 48:34–53, 09 2013.

[34] E. Chu. Generalization of hill's 1979 anisotropic yield criteria. *Journal of Materials Processing Technology*, 50(1):207 – 215, 1995. 2nd International Conference on Numerical Simulation of 3-D Sheet Metal Forming Processes.

[35] Odd-Geir Lademo, Odd Hopperstad, and M. Langseth. An evaluation of yield criteria and flow rules for aluminium alloys. *International Journal of Plasticity*, 15:191–208, 03 1999.

[36] J. Bishop and R. Hill. A theory of the plastic distortion of a polycrystalline aggregate under combined stress. *Philosophical Magazine Series 6*, 42:414–427, 04 1951.

[37] V. Tvergaard. On localization in ductile materials containing spherical voids. *International Journal of Fracture*, 18(4):237–252, 1982.

[38] C.C. Chu and A. Needleman. Void Nucleation Effects in Biaxially Stretched Sheets . *Journal of Engineering Materials and Technology*, 102:249–256, 1980.

[39] 2014. Dassault Systems. Abaqus analysis user's guide-6.3.3 explicit dynamic analysis.

[40] K. M. Mathisen. 2014e. lecture notes for course tkt4197 - nonlinear finite element analysis. norwegian university of science and technology.

[41] Ted Belytschko, Wing Kam Liu, and Brian Moran. *Nonlinear Finite Elements for Continua and Structures*. John Wiley Sons, Ltd, 2000.

[42] E. Fagerholt. 2017, ecorr v4.0 documentation, norwegian university of science and technology. 2017.

[43] S.A. El-Naaman and K.L. Nielsen. Observations on mode i ductile tearing in sheet metals. *European Journal of Mechanics - A/Solids*, 42:54–62, 11 2013.

[44] M. A Sutton, D. S Dawicke, and Jr Newman, J. C. *Orientation effects on the measurement and analysis of critical CTOA in an aluminum alloy sheet.* 1994.

[45] R. Becker, Alan Needleman, O RICHMOND, and Viggo Tvergaard. Void growth and failure in notched bars. *Journal of The Mechanics and Physics of Solids - J MECH PHYS SOLIDS*, 36:317–351, 12 1988.

[46] Erik L. Grimsmo, Lars Edvard Dæhli, Odd Hopperstad, Arne Aalberg, Magnus Langseth, and Arild Clausen. Numerical study of fillet welds subjected to quasi-static and impact loading. *International Journal of Mechanical Sciences*, 131, 08 2017.

[47] Zhiliang Zhang, C Thaulow, and J Ødegård. Complete gurson model approach for ductile fracture. *Engineering Fracture Mechanics*, 67:155–168, 09 2000.

[48] 2013. Dassault Systèmes. Abaqus analysis user's guide - 23.2.9 porous metal plasticity.

[49] Thomas Pardoen, F. Hachez, B. Marchioni, P.H. Blyth, and A. Atkins. Mode i fracture of sheet metal. *Journal of the Mechanics and Physics of Solids*, 52:423–452, 02 2004.

[50] Hongcheng Huang and Liang Xue. Prediction of slant ductile fracture using damage plasticity theory. *International Journal of Pressure Vessels and Piping*, 86:319–328, 05 2009.

[51] Mehrdad Javadi and Mehdi Tajdari. Experimental investigation of the friction coefficient between aluminium and steel. *Materials Science- Poland*, 24, 01 2006.

A Figures

A.1 Figures to section 3 (Experimental setups)

Figure A.1: Picture taken of the experimental DENT-test set-up.

A.2 Figures to section 4 (Finite element modelling)

Different meshing configurations of the SENT-model

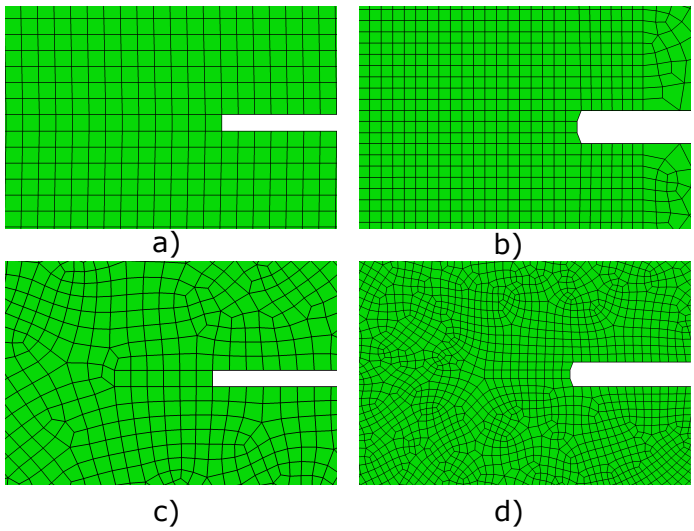

Figure A.2: The the critical region of the SENT-specimen modelled using a structured mesh of a) h_e=0.25 and b) h_e=0.15 and using an irregular swept mesh combined with c) h_e=0.25 and d) h_e=0.15

The original and revised mesh used in the DENT simulations

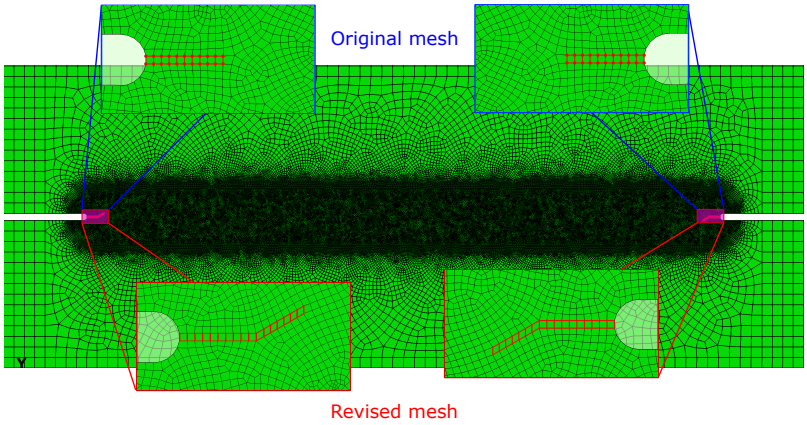

Figure A.3: The original mesh used for the bulk of numerical simulations of the DENT-test and the revised mesh used to replicate the experimental crack and assess mesh design sensitivity.

A.3 Figures to section 5 (Calibration of material models)

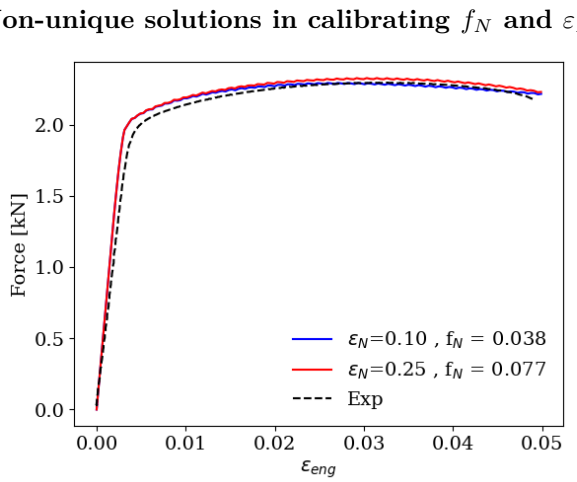

Figure A.4: Nearly identical force - strain curves for the NT3-T6 temper simulations using distinct combinations of ε_N and f_N of the T6 .

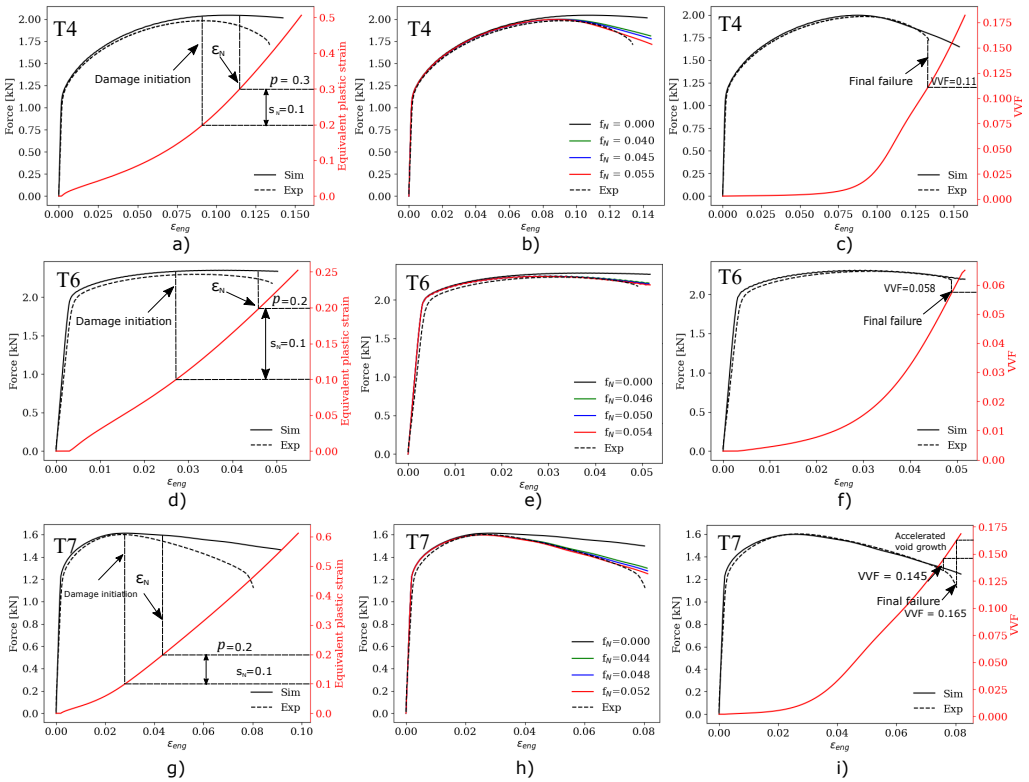

Figure A.5: Illustration of the applied calibration process for the GTN-paramters: a,d,g) Extraction of ε_N at the onset of deviation between experimental force-strain curves and the corresponding FE analysis results of the GTN-model with nucleation omitted. b,e,h) f_N optimization steps. c,f,i) Extraction of the fracture parameters, f_c from the simulated VVF corresponding to the experimental fracture strain.

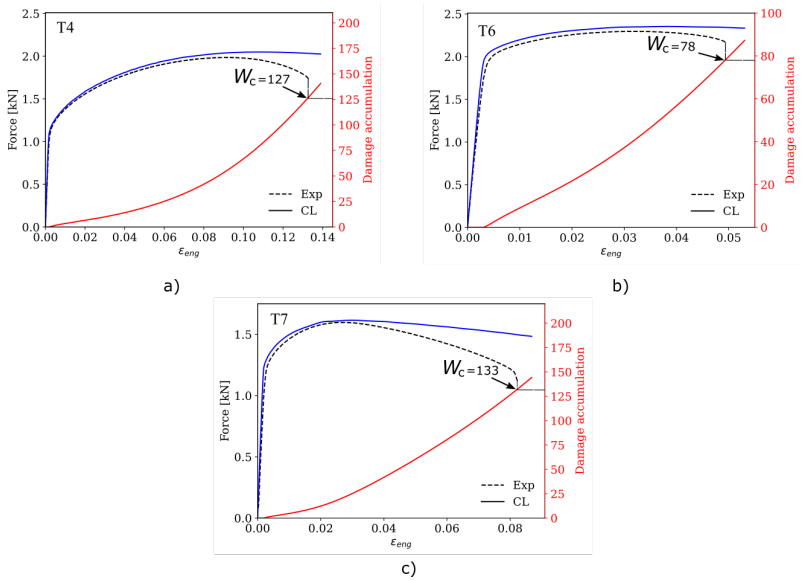

Figure A.6: Force-strain curves and logarithmic strains from experiments and simulations of the NT3 - tensile tests using characteristic element length h_e =0.15mm.

A.4 Figures to section 6 (Numerical results and Discussion)

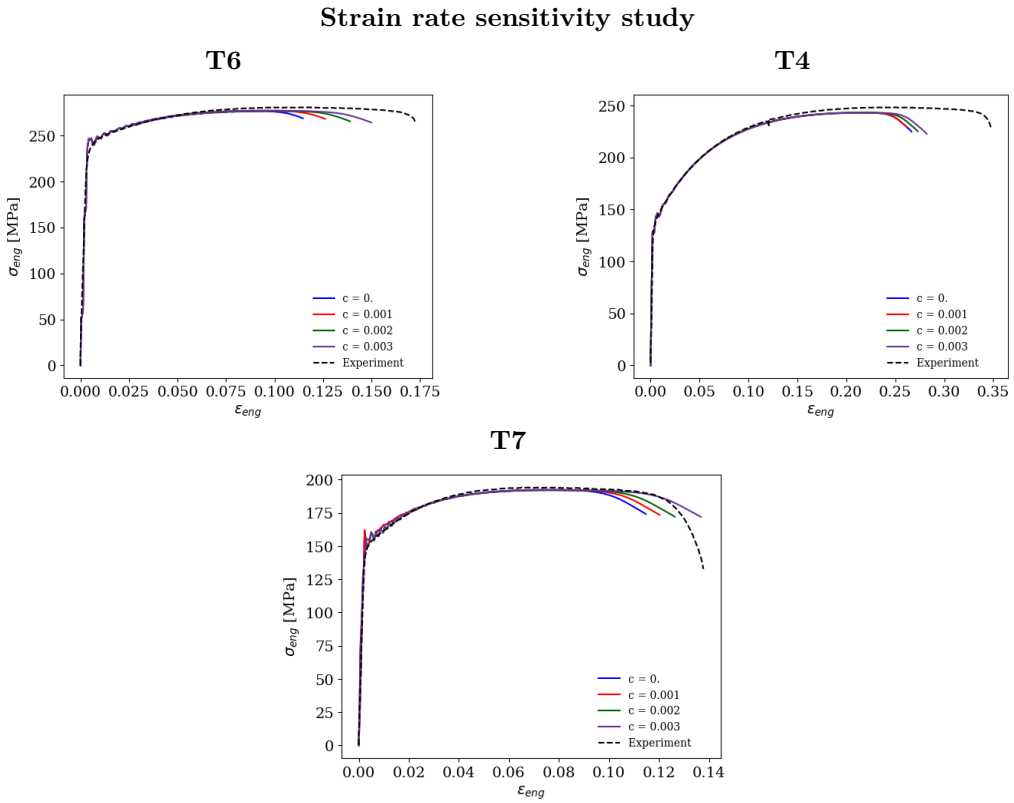

Figure A.7: Influence of strain-rate-dependence on the behavior of the smooth specimen.

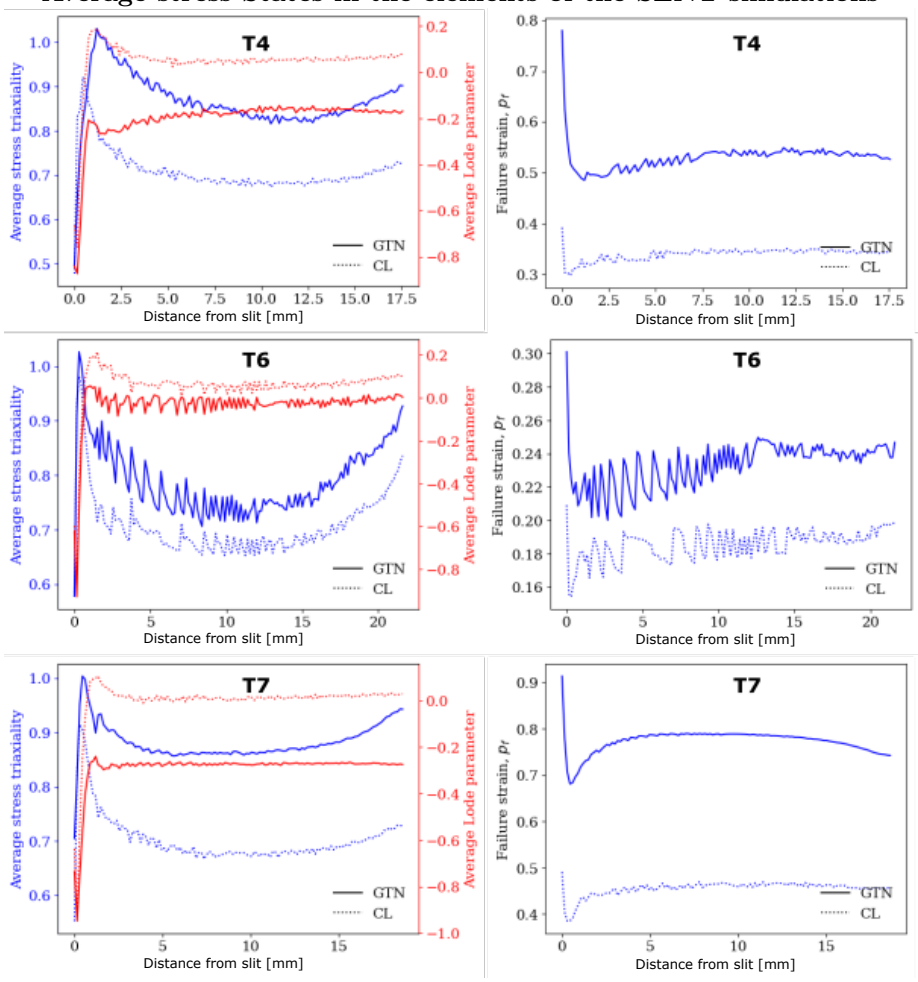

Figure A.8: (left column) Average stress triaxiality and lode parameter of elements in the predicted crack plane having accumulated 20 % of the total predicted damage as a function of the elements position from the slit . (right column) Average equivalent plastic strain of elements as a function of the elements position from the slit.

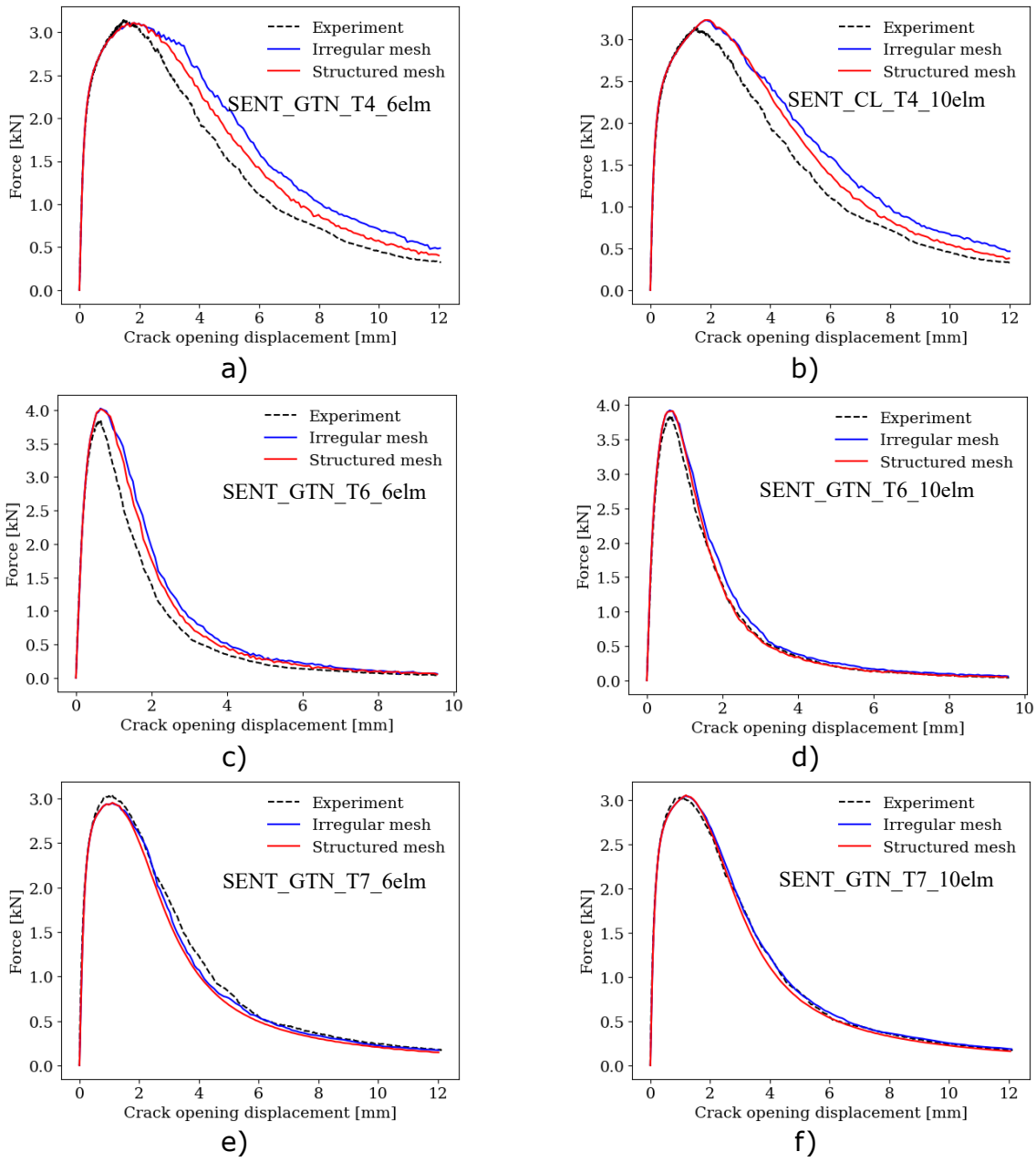

Figure A.9: Experimental and numerical force-strain curves from the SENT-test applying the GTN-model to combined with the structured and irregular mesh using a mesh size (a,c,e)0.25mm (b,d,f) 0.15mm.

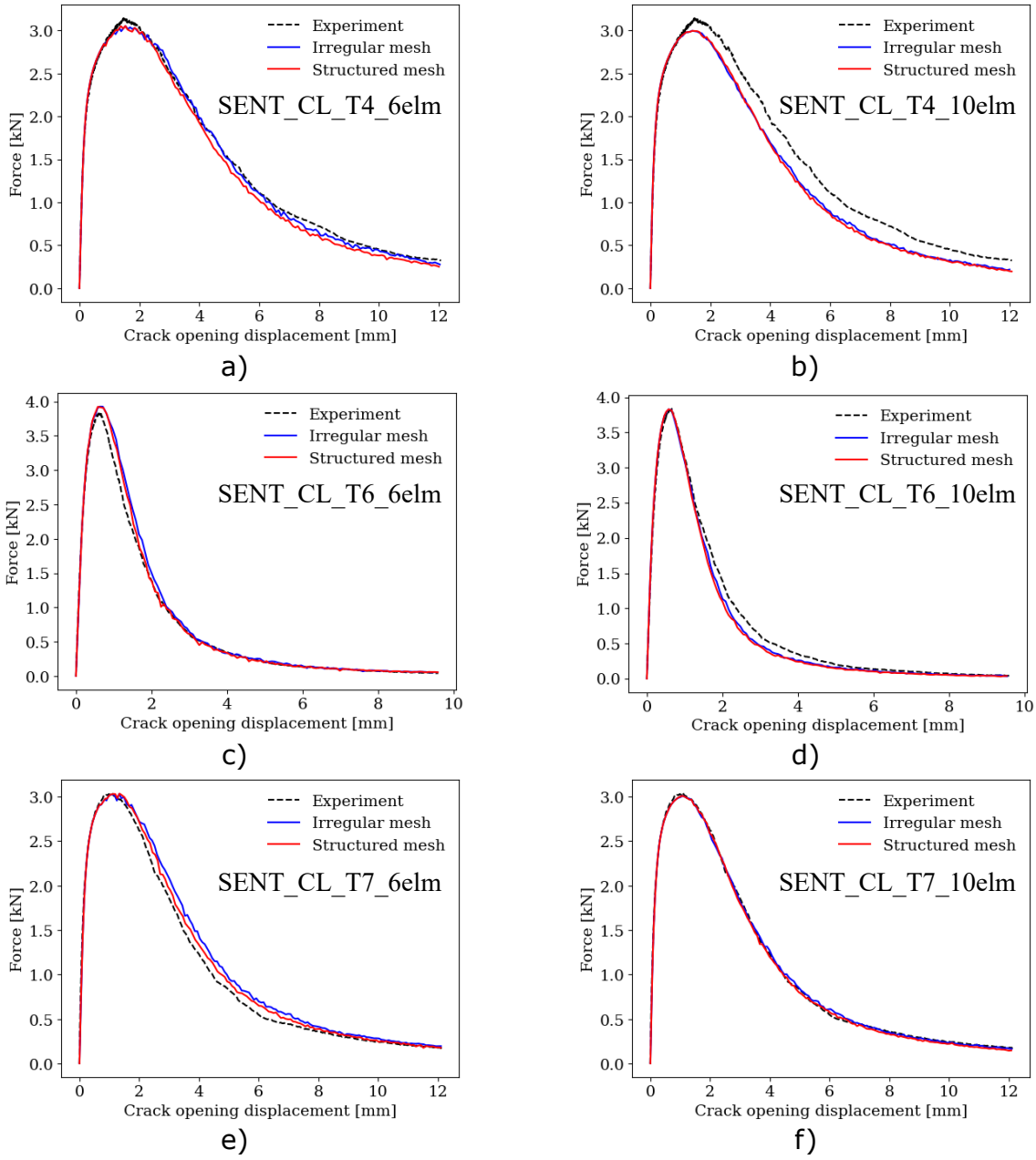

Figure A.10: Experimental and numerical force-strain curves from the SENT-test applying the CL-model to combined with the structured and irregular mesh using a mesh size (a,c,e)0.25mm (b,d,f) 0.15mm.

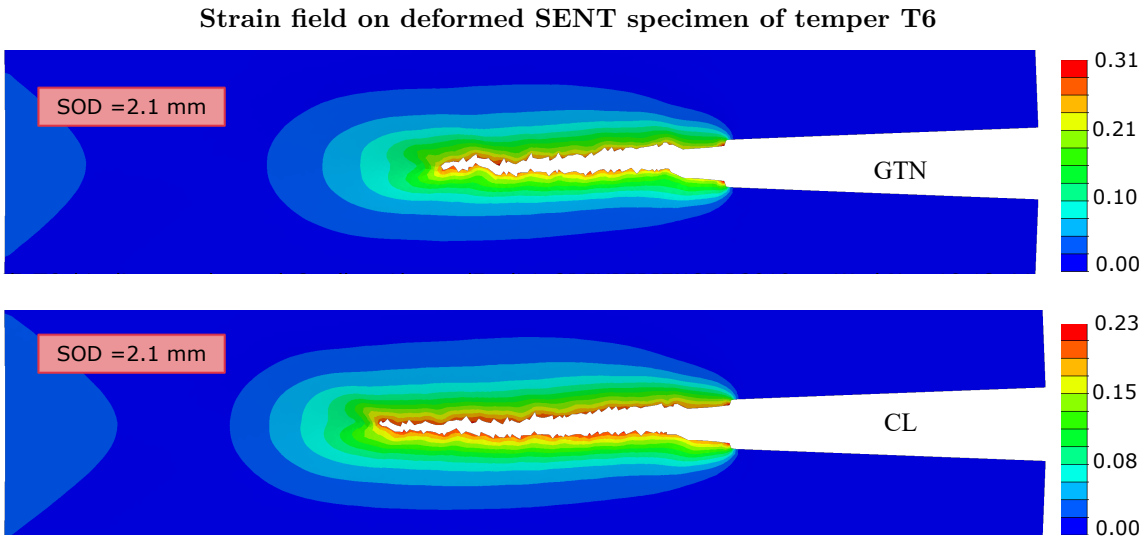

Figure A.11: Equivalent plastic strain fields on the cracked SENT- specimen from the (top) GTN-T6 simulation and the (bottom) CL-T6 simulation.

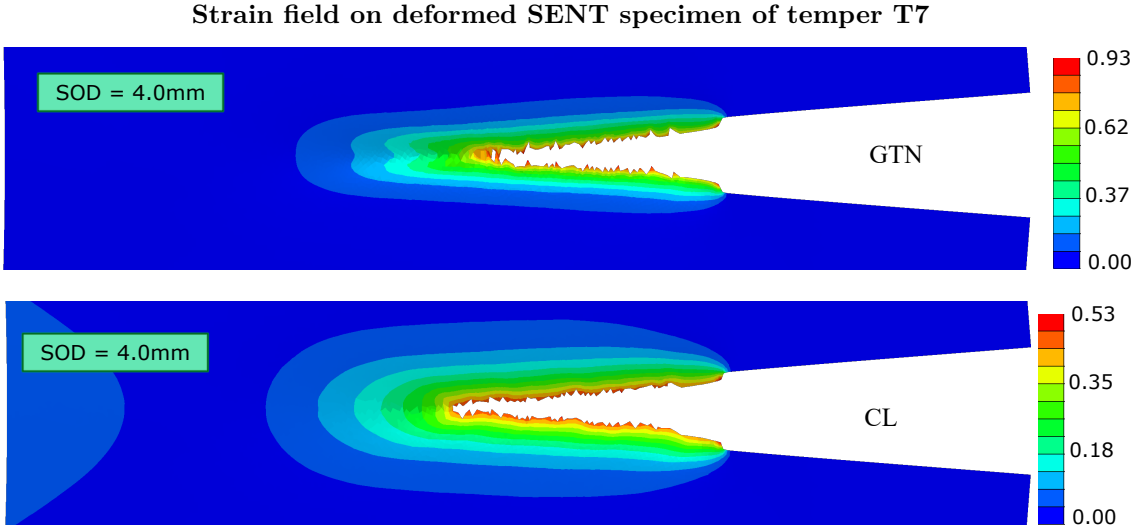

Figure A.12: Equivalent plastic strain field map on the cracked SENT- specimen from the (top) GTN-T7 simulation and the (bottom) CL-T7 simulation.

Experimental and simulated crack path in the T4 temper using the revised model

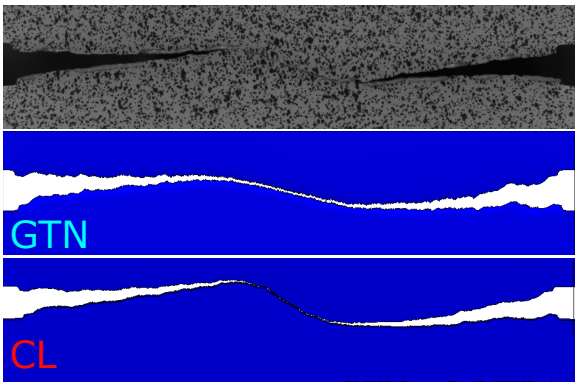

Figure A.13: Experimental and simulated crack path in the T4 temper using a revised mesh and discarding the thickness symmetry plane..

Experimental and simulated crack path in the T4 temper using the revised model

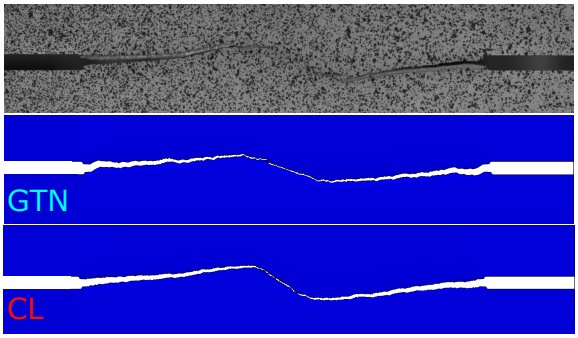

Figure A.14: Experimental and simulated crack path in the T6 temper using a revised mesh and discarding the thickness symmetry plane.

A.5 Figures to section 7 (Modified Arcan-tests)

Illustration of the Modified Arcan model

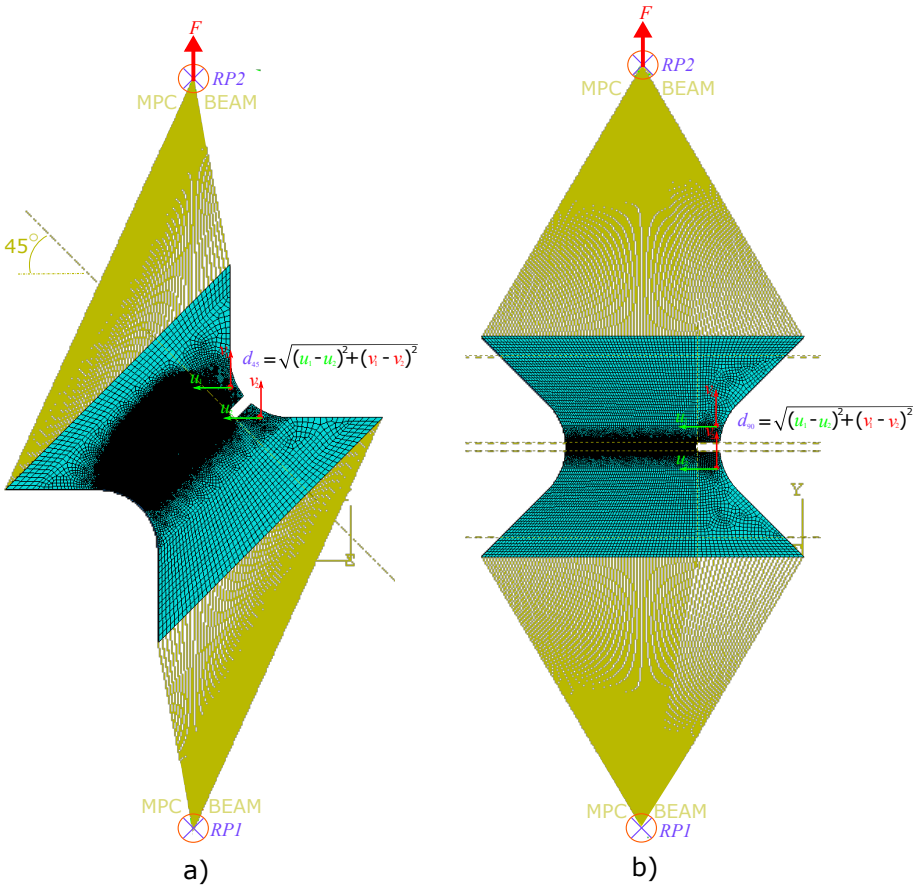

Figure A.15: Representation of the a) Arcan45 and b) Arcan90 model in Abaqus.

A.6 Figures to section 8 (Drop weight impact test)

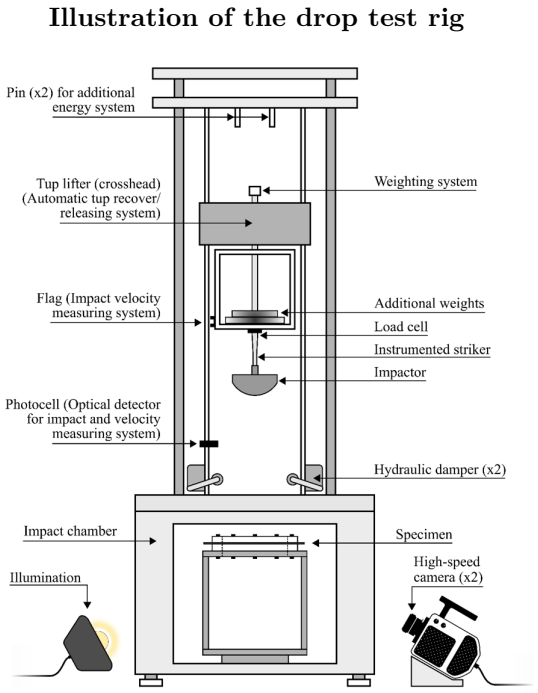

Figure A.16: Illustrative drawing of the drop weight experiment created by PhD. candidate Vetle Espeseth.

B Theory

B.1 The Central Difference Method

In Abaqus the governing equation of motion, expressed on matrix form as:

$$[M]\{\ddot{D}(t)\} + [C]\{\dot{D}(t)\} + [K]\{D(t)\} = \{R^{ext}(t)\} \tag{B.1}$$

is solved in time to obtain the structural response. Using the central difference method, the velocity and accelerations are obtained from Taylor series expansion of $\{D\}_{n+1}$ and $\{D\}_{n-1}$, neglecting terms of Δt above second order, thus,

$$\{\dot{D}\}_n = \frac{1}{2\Delta t}(\{D\}_{n+1} - \{D\}_{n-1}) \tag{B.2}$$

$$\{\ddot{D}\}_n = \frac{1}{\Delta t^2}(\{D\}_{n+1} - 2\{D\}_n + \{D\}_{n-1}) \tag{B.3}$$

Introduced into the equation of motion the following is obtained:

$$\left(\frac{[M]}{\Delta t^2} + \frac{[C]}{2\Delta t}\right)\{D\}_{n+1} = \{R^{ext}\} + \left(2\frac{[M]}{\Delta t^2} - [K]\right)\{D\}_n - \left(\frac{[M]}{\Delta t^2} - \frac{[C]}{2\Delta t}\right)D_{n-1} \tag{B.4}$$

where the bracket term on the left side is denoted the effective stiffness, K^{eff} and the right hand side the effective load, R^{eff}. Thus the displacement for the next increment is given by:

$$\{D\}_{n+1} = [K^{eff}]^{-1}\{R^{eff}\}_n \tag{B.5}$$

In a general dynamic response analysis it can be desirable to include stiffness-proportional damping $[C] = \beta[K]$ to damp high-frequency numerical noise. This makes the effective stiffness matrix $[K^{eff}] = \left(\frac{[M]}{\Delta t^2} + \frac{[C]}{2\Delta t}\right)$ non-diagonal and thus the computational cost per time increases significantly. To overcome this problem, it is possible to establish the equilibrium equations with velocity lagging by half time step[40](see Eq.(B.6)).

$$[M]\{\ddot{D}\}_n + [C]\{\dot{D}\}_{n-\frac{1}{2}} + [K]\{D\}_n = \{R^{ext}\}_n \tag{B.6}$$

This method is called the half-step central difference method and is established using the following equations for velocity and acceleration, respectively:

$$\{\dot{D}\}_{n+\frac{1}{2}} = \frac{1}{\Delta t}(\{D\}_{n+1} - \{D\}_n) \tag{B.7}$$

$$\{\dot{D}\}_{n-\frac{1}{2}} = \frac{1}{\Delta t}(\{D\}_n - \{D\}_{n-1}) \tag{B.8}$$

$$\{\ddot{D}\}_n = \frac{1}{\Delta t^2}\left(\{\dot{D}\}_{n+\frac{1}{2}} - \{\dot{D}\}_{n-\frac{1}{2}}\right) = \frac{1}{\Delta t^2}(\{D\}_{n+1} - 2\{D\}_n + \{D\}_{n-1}) \tag{B.9}$$

Inserted into the equation of motion we get:

$$\left(\frac{[M]}{\Delta t^2}\right)\{D\}_{n+1} = \{R^{ext}\} - [K]\{D\}_n + \frac{[M]}{\Delta t^2}\left(\{D\}_n + \Delta t\{\dot{D}\}_{n-\frac{1}{2}}\right) - [C]\{\dot{D}\}_n - \frac{1}{2} \tag{B.10}$$

Ahead of the first iteration $\{\dot{D}\}_{n-\frac{1}{2}}$ must be obtained by a backward difference approximation.

$$\{\ddot{D}\}_0 = \frac{1}{\frac{\Delta t}{2}}\left(\{\dot{D}\}_0 - \{\dot{D}\}_{-\frac{1}{2}}\right) \tag{B.11}$$

$$\{\dot{D}\}_{-\frac{1}{2}} = \frac{2}{\Delta t}\{\ddot{D}\}_0 - \{\dot{D}\}_0 \tag{B.12}$$

where $\{\ddot{D}\}_0$ is found by evaluation Eq. (B.1) at t_0.

B.2 Drop test displacement calculation

Newtonian mechanics is applied to the striker and carriage using:

$$mg - F = m\frac{dv}{dt} \tag{B.13}$$

where F is the force applied to the striker, measured by a sensor, m is the mass and, g is the gravitational constant. Integrating Eq. (B.13) the velocity at any time, t, is obtained.

$$v = v_0 + gt - \frac{1}{m}\int_0^t F\,dt \tag{B.14}$$

Equation (B.14) is further integrated to obtain the displacement

$$x = v_0 t + \frac{gt^2}{2} - \frac{1}{m}\int_0^t (\int_0^t F\,dt)\,dt \tag{B.15}$$

C Material Cards

C.1 T6

```
*Material, name=GTN_for_T6
*Density
 2.7e-09,
*Depvar, delete=4
      4,
1, p,"equivalent plastic strain"
2, pdot, "equivalent plastic strain rate"
3, W, "Cockroft-Latham failure model"
4, FAIL, "failure indicator"
*Elastic
70000., 0.3
*Plastic, hardening=USER, properties=12
**SIGMA0, TETHA1,    Q1, TETHA2,     Q2, TETHA3,     Q3,       C
   226.9, 11430., 15.23,  1272.,  51.17,   235.,  5229.,    0.0
**epsot0,    m,  Tr,  Tm
     0.0,  0.0, 0.0, 0.0
*Porous Metal Plasticity, relative density=0.997
** q1,   q2,    q3
  1.5,   1.,  2.25
*Porous Failure Criteria
**  VVFCF,    VVFCR
     0.058,   0.058
*Void Nucleation
** en,   sn,     fn
  0.2,  0.1,  0.054

** ----------------------------------------------------------------
```

```
*Material, name=Cockroft_Latham_for_T6
*Density
 2.7e-09,
*Depvar, delete=4
      4,
1, p,"equivalent plastic strain"
2, pdot, "equivalent plastic strain rate"
3, W, "Cockroft-Latham failure model"
4, FAIL, "failure indicator"
*Elastic
70000., 0.3
*Plastic, hardening=USER, properties=12
**SIGMA0, TETHA1,    Q1, TETHA2,     Q2, TETHA3,     Q3,       C
   226.9, 11430., 15.23,  1272.,  51.17,   235.,  5229.,    0.0
**epsot0,    m,  Tr,  Tm
     0.0,  0.0, 0.0, 0.0
*User Defined Field, properties = 2
**   Wc,   Tc
   78.0,  0.0

** ----------------------------------------------------------------
```

C.2 T7

```
*Material, name=GTN_for_T7
*Density
 2.7e-09,
*Depvar, delete=4
      4,
1, p,"equivalent plastic strain"
2, pdot, "equivalent plastic strain rate"
3, W, "Cockroft-Latham failure model"
4, FAIL, "failure indicator"
*Elastic
70000., 0.3
*Plastic, hardening=USER, properties=12
**SIGMA0, TETHA1,    Q1, TETHA2,     Q2, TETHA3,     Q3,      C
   145.3, 13620., 2.464,  2385.,  52.95,  138.6,  6626.,     0.
**epsot0,    m,  Tr,  Tm
     0.0,  0.0, 0.0, 0.0
*Porous Metal Plasticity, relative density=0.998
** q1,   q2,    q3
  1.5,   1.,  2.25
*Porous Failure Criteria
**  VVFCF,    VVFCR
     0.2,     0.145
*Void Nucleation
** en,   sn,     fn
  0.2,  0.1,  0.052

** ----------------------------------------------------------------
```

```
*Material, name=Cockroft_Latham_for_T7
*Density
 2.7e-09,
*Depvar, delete=4
      4,
1, p,"equivalent plastic strain"
2, pdot, "equivalent plastic strain rate"
3, W, "Cockroft-Latham failure model"
4, FAIL, "failure indicator"
*Elastic
70000., 0.3
*Plastic, hardening=USER, properties=12
**SIGMA0, TETHA1,    Q1, TETHA2,     Q2, TETHA3,     Q3,    C
   145.3, 13620., 2.464,  2385.,  52.95,  138.6,  6626.,  0.0
**epsot0,    m,  Tr,  Tm
     0.0,  0.0, 0.0, 0.0
*User Defined Field, properties = 2
**   Wc,   Tc
  133,  0.0

** ----------------------------------------------------------------
```

C.3 T4

```
*Material, name=GTN_for_T4
*Density
 2.7e-09,
*Depvar, delete=4
      4,
1, p,"equivalent plastic strain"
2, pdot, "equivalent plastic strain rate"
3, W, "Cockroft-Latham failure model"
4, FAIL, "failure indicator"
*Elastic
70000., 0.3
*Plastic, hardening=USER, properties=12
**SIGMA0, TETHA1,    Q1,   TETHA2,    Q2, TETHA3,       Q3,      C
   123.3, 1.241e+4, 10.64,  1941., 118.3,  279.4, 2.455e+4,    0.0
**epsot0,    m,  Tr,  Tm
     0.0,  0.0, 0.0, 0.0
*Porous Metal Plasticity, relative density=0.997
** q1,   q2,    q3
  1.5,   1.,  2.25
*Porous Failure Criteria
**  VVFCF,    VVFCR
     0.11,     0.11
*Void Nucleation
** en,   sn,     fn
  0.3,  0.1,  0.055

** ----------------------------------------------------------------
```

```
*Material, name=Cockroft_Latham_for_T4
*Density
 2.7e-09,
*Depvar, delete=4
      4,
1, p,"equivalent plastic strain"
2, pdot, "equivalent plastic strain rate"
3, W, "Cockroft-Latham failure model"
4, FAIL, "failure indicator"
*Elastic
70000., 0.3
*Plastic, hardening=USER, properties=12
**SIGMA0,   TETHA1,    Q1, TETHA2,    Q2, TETHA3,       Q3,    C
   123.3, 1.241e+4, 10.64,  1941., 118.3,  279.4, 2.455e+4,    0.0
**epsot0,    m,  Tr,  Tm
     0.0,  0.0, 0.0, 0.0
*User Defined Field, properties = 2
**   Wc,   Tc
    127,  0.0

** ----------------------------------------------------------------
```

Aslak Magdalon Blytt & Sander Sundt

Crack propagation in aluminium alloy plates

NTNU
Norwegian University of
Science and Technology